Title
Improved PVDF Terpolymers for Solid State Cooling and Beyond

Author
Zhang, Ziyang

Publication Date
2019

Peer reviewed|Thesis/dissertation

UNIVERSITY OF CALIFORNIA

Los Angeles

Improved PVDF Terpolymers for Solid State Cooling and Beyond

A dissertation submitted in partial satisfaction of the

requirements for the degree Doctor of Philosophy

in Materials Science and Engineering

by

Ziyang Zhang

2019

ABSTRACT OF THE DISSERTATION

Improved PVDF Terpolymers for Solid State Cooling and Beyond

by

Ziyang Zhang

Doctor of Philosophy in Materials Science and Engineering

University of California, Los Angeles, 2019

Professor Qibing Pei, Chair

Cooling is a basic need for human beings. Vapor compression cooling is the technology behind almost all of the applications. However, limited by its mechanism, the vapor compression refrigeration is not suitable for modern technologies such as mobile devices and personal cooling. Besides, it relies on refrigerants like Freon and hydrofluorinecarbons, which pose serious environmental problems. Therefore, it is urgent and over-due to develop new cooling technologies that are efficient and environmentally friendly.

As a solid-state cooling technology, electrocaloric cooling offers several advantages over traditional cooling systems, but few devices offer high specific cooling power and a high coefficient of performance (COP). To develop electrocaloric cooling technology towards commercialization, we attacked the project through both material and device directions.

We developed a solution process fabrication method for large area EC film fabrication. Various material characterizations were conducted to study and optimize the performance of the EC film. The as-fabricated EC film has an active area of 10 cm^2 and a cycling test was conducted to prove its reliability under repeating high voltage. Another material's effort is to chemically modify the EC polymer for features like better mechanical strength, reliability, and high dielectric constant. Poly(vinylidene fluoride-trifluoroethylene-chlorofluoroethylene) was used as the starting material. It is a dehydrochlorination reaction catalyzed by triethylamine. The organic base attacks the hydrogen close to the Cl atoms, and the reaction introduces unsaturated double bond in the polymer chain. The unsaturated sites can be used as active sites for functional group introduction to modify the polymer further. In particular, we used this double-bonding containing polymer as the precursor to prepare crosslinked thin films and demonstrated improved capacitive energy storage.

We presented a cooling device with high intrinsic thermodynamic efficiency using a flexible electrocaloric (EC) polymer film and an electrostatic actuation mechanism to transfer heat between a heat source and a heat sink. Reversible electrostatic forces reduce parasitic power consumption and allow efficient heat transfer through excellent thermal contact with the heat source or sink. The EC device produced a specific cooling power of 2.8 W/g and a relative COP of 13. Our cooling device is more efficient and compact than existing solid-state cooling technologies, showing a path towards using the technology for a variety of practical applications.

The dissertation of Ziyang Zhang is approved.

Yong Chen

Laurent Pilon

Qibing Pei, Committee Chair

University of California, Los Angeles

2019

Dedicated to my beloved wife

Muhong

Table of Contents

List of Figures

Acknowledgements

First and foremost, I would like to express my sincere gratitude to my advisor, Professor Qibing Pei, for his guidance and generous support over the past five years. The completion of this dissertation would not be possible without his insight and mentorship.

I would also like to thank Professor Yong Che, Professor Ali Mosleh, and Professor Laurent Pilon for serving on my committee, providing guidance and suggestions that are vital for the completion of this dissertation.

I am grateful to all current and past members of the Soft Materials Laboratory Research Group whom I have had the pleasure to work with during this and other related projects. I am indebted to Dr. Rujun Ma, Dr. Yi Chen, Dr. Jorge Oliva, Dr. Wei Hu, Dr. Zhi Ren, Dr. Chao Liu, Dr. Huier Gao, Dr. Kwing Tong, Dr. Charlotte Chou, Dr. Yuan Meng, Dr, Ye Shi, Dr. Yu Xie, Mr. Zhixin Xie, Mr. Zhou Li, Mr. Hexing Yin, Mr. Kareem Youssef, Ms. Zihang Peng, Ms. Jianghan Wu, Mr. Hanxiang Wu, Mr. Haolun Wang, Mr. Adie Alwen and Ms. Fangyi Guan for their discussion and help during my PhD journey.

I would also like to extend my appreciation to my collaborators at UCLA's Electrical Engineering department. Many thanks to Prof. Aydin Babakhani, Dr. Hongming Lyu, and Mr. Xiangyu Liu. Thank you for helping me with the wireless charging project.

A special thanks go to my friends Dr. Cai Chen, Dr. Junlong Kou, Dr. Yue Zhao, and Dr. Xinke Yu for the insightful discussions both in and out the academic field. You all helped me to keep things in perspective and maintain a healthy stress level.

Finally, I want to thank my wife Ms. Muhong Zhou and my parents and parents-in-law, Ms. Hongwei Han, Mr. Cheng Zhang, Ms. Guiyun Ma, and Mr. Zhongxin Zhou for their support and unconditional love.

Vita

2014	Bachelor Degree, Kuangyaming Honors School, Nanjing University
2018	Associate Intern, IDG Capital, Beijing, China
2018	Research Intern, Hardware Research Lab, PARC, Palo Alto, CA
2014 – 2019	Research Assistant, Soft Materials Research Lab, UCLA

1 Introduction

1.1 Background on Electrocaloric Cooling

1.1.1 Background

Refrigerators and air conditioners based on the Vapor Compression Cycle (VCC) are omnipresent in modern society. Gases like Freon gases, chlorofluorocarbons (CFCs) and hydrochlorofluorocarbons (HCFC) are widely used in vapor compression systems. These gases once leak to the atmosphere will deplete ozone, which protects the earth against ultraviolet (UV) radiation. Moreover, with more than one hundred years' research, it has been rather hard to push the efficiency of the vapor compression system to a higher level. Thus, research and development of novel cooling materials are critical to many industries that need highly efficient and environmentally friendly cooling systems.

Nowadays there are four types of cooling technologies that have been studied, namely vapor compression system, thermoelectric cooler, Magnetocaloric cooler, and Electrocaloric cooler. For conventional vapor compression cycle technology, everything is optimized, and there is no growth can be made in this market. Also, the size of vapor compression cycle systems is a barrier to its application in the microelectronic industry. The thermoelectric effect has been studied for decades and has been applied widely in some extreme environments like space exploration. However, because of its physical mechanism, high efficiency of thermoelectric cooler or power generator cannot be delivered. Magnetic cooling is based on Magnetocaloric effect. Though the effect has been used for decades in the laboratory to reach extremely low temperatures. Its application as a commercial cooling system just emerged. In 2015 Consumer Electronics Show (CES), Haier and BASF brought

up the first refrigerator utilizing Magnetocaloric effect. As claimed, Magnetocaloric cooler can be as efficient as 70% of Carnot efficiency, however large magnetic fields are necessary for Magnetocaloric cooling system, which makes dimension decreasing of Magnetocaloric system impossible.

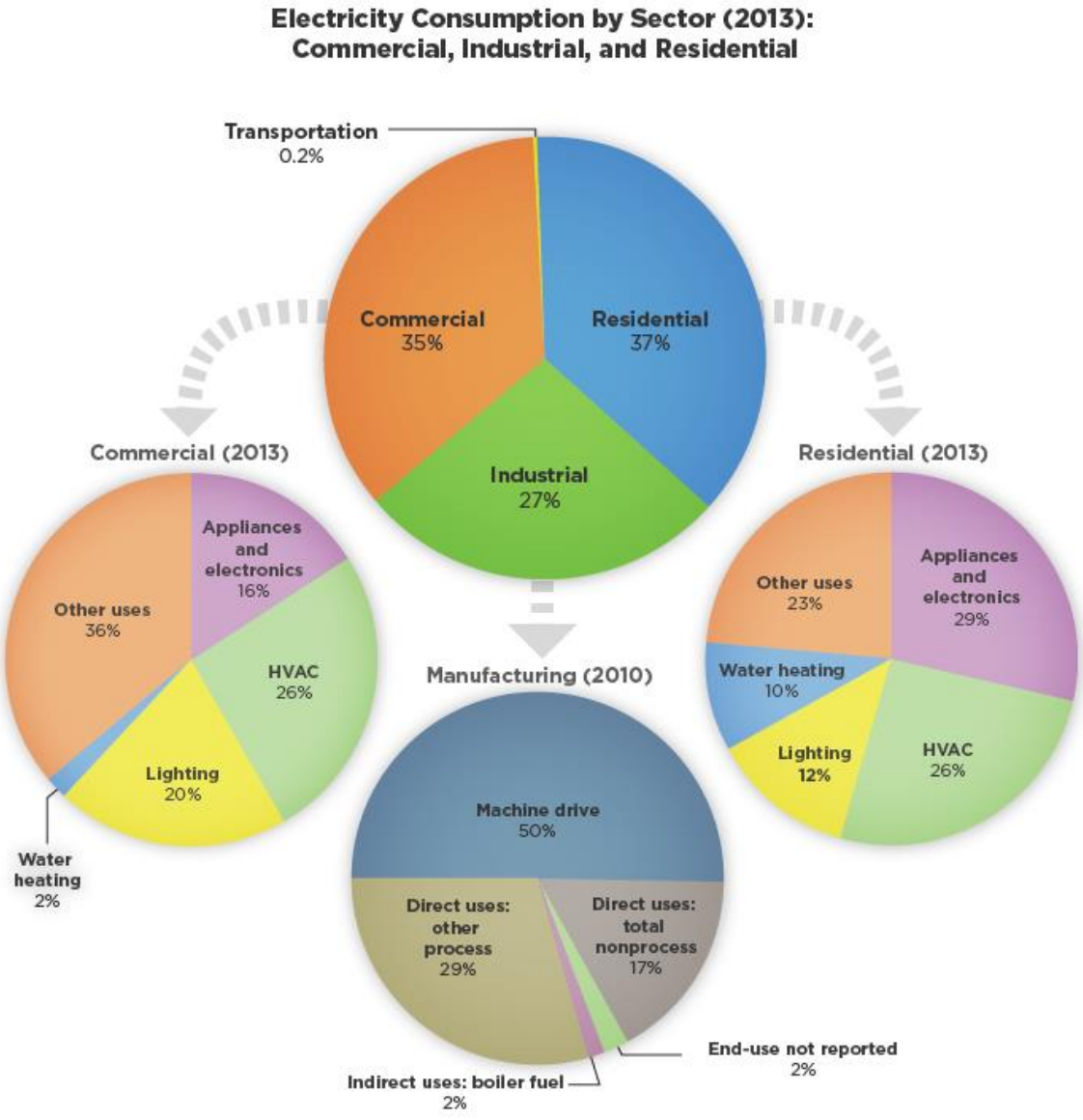

Figure 1-1. Electricity consumption by sectors.(1)

Coefficient of Performance (COP) is widely used to evaluate the performance of heat pumps. COP is defined as the ratio between the heat that is absorbed in the cold end,

Q_C and total input work *W*. Carnot COP is the maximum COP that a heat pump can reach, can be calculated by $T_H/(T_H - T_C)$, where T_C and T_H is the temperature of cold end and hot end respectively. For a Carnot cycle pumping heat from 300K to 320 K, the theoretical COP can be as high as 15, which indicates that the heat pump can be very efficient. However, nowadays, the vapor compression refrigerators (VCR) typically have a COP of 2-4. According to Figure 1-1, electricity use for space cooling and refrigeration consists of more than 30% of annual residential power usage in the US. Even only 10% COP improvement would save 110 terawatt-hours energy that is almost the annual electricity consumption in Mexico(*1*).

An average American home uses 11,700 kWh each year, which means 7 t CO_2 emission and costs around $ 1,400. Improving energy efficiency and reducing electricity usage can make a significant impact on our society both economically and environmentally(*1*). Meanwhile, heat management systems, including highly compact and efficient cooling devices, are highly demanded in various emerging fields. The localized thermal management system creates a comfortable localized micro-environment without cooling the whole space. Besides, with the continuously increasing computing power and the integrated density of chips, cooling of powerful chips has been a critical method to keep the chips work at their prime and increase their durability. The heating of handset devices is still a headache for consumer electronic product designers.

1.1.2 Alternative refrigeration methods

Electrocaloric effect (ECE) is one of a class of caloric effects that generate adiabatic temperature and/or isothermal entropy change in response to external stimuli. Electric field,

magnetic field, stress/strain, and hydrostatic pressure can all act as the external stimuli. Respectively, they are named as the electrocaloric effect (ECE), the magnetocaloric effect (MCE), the elastocaloric effect (eCE) and the barocaloric effect (BCE). Caloric effects are not new but recently attracting a lot for attraction in both academia and the industrial world. Elastocaloric effect was first reported by J. P. Joule in 1859. The first experimental observation of MCE was in 1881 by Warburg, and in the 1930s ECE was discovered in Rochelle salt(*2*). It was until the discoveries of giant MCE and giant ECE that scientists realized the high potentials of caloric materials(*3*, *4*).

Since the report of the Giant MCE, various designs to utilize MCE have been reported. After 2000, an active magnetic regenerator (AMR) has been widely studied, and a lot of them are prototyped(*5*, *6*). Theoretical analyses indicate that MCE can yield a higher efficiency even than the best air-cooled vapor compression systems nowadays. However, Magnetocaloric materials generally contain rare-earth elements, including Gadolinium (Gd), Lanthanum (La) and Rhodium (Rh), which makes the cost of MCE devices extremely expensive. Besides, MCE requires a high magnetic field (usually higher than 1.5 Tesla). It is challenging, if not impossible, to shrink the size of the devices for practical applications.

Moreover, such a large magnetic field may cause malfunction of electronic devices that keep MCE cooling devices from the application of heat management for chips. Compared with MCE and ECE, eCE and BCE are driven by mechanical stimuli, and the frequency is limited, which yields a lower cooling power. When applying the mechanical field, structure phase transition of eCE and BCE materials is induced and leads to caloric effect. Recently giant BCE at low pressure in ferroelectric ammonium sulfate was reported

and indicates the potential of BCE cooling and indicated the potential of BCE cooling(*7*, *8*).

Table 1-1. Comparison of different refrigeration methods.

Technology	Cooling Power Density	COP	Scalability	Current state
VCR	Medium	Medium	Low	Commercial(developed)
Thermoelectric	High	Low	High	Commercial
eCE&BCE	Low	High	Low	Prototype
Magnetocaloric	Medium	High	Low	Prototype
Electrocaloric	High	High	High	prototype

1.1.3 Electrocaloric effect

Electrocaloric effect (ECE) is defined as the temperature change of dielectric materials when an electric field is applied or removed. It has potential applications in air conditioning, efficient refrigeration, and heat management of microelectronics. Figure 1-2 illustrates the molecular mechanism of ECE in dielectric materials(*9*).

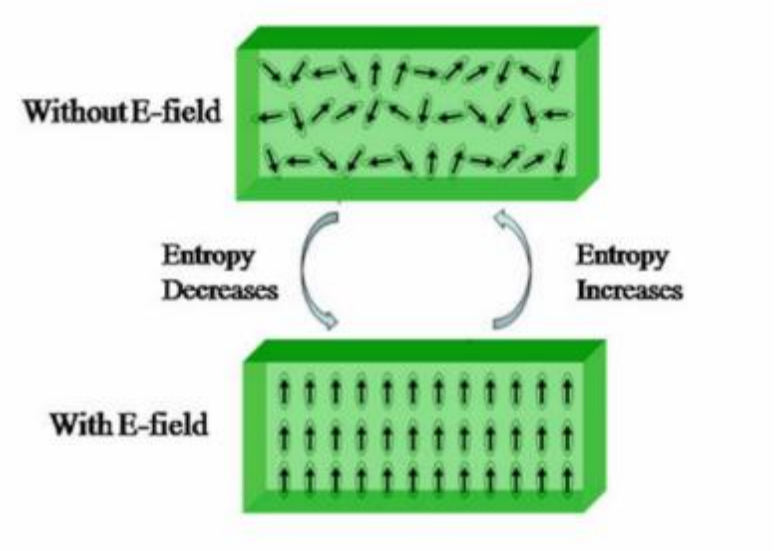

*Figure 1-2. schematic illustration of the molecular mechanism of ECE in dielectric materials. When E = 0, the dipoles orient randomly, having higher dipolar entropy. When E >0, the dipoles orient along the electric field direction, lowering the dipole entropy.(*9*)*

The basic principle of the electrocaloric effect is the entropy change associated with the change of polarization ordering in a dielectric material, induced by an external electric field (as the schematic illustration of figure 1-2). When changing from a non-polar phase to a polar phase or vice versa, there will be an accompanying entropy change. Application of an electric field to the material causes partial alignment of dipoles and consequently a reduction of entropy of the dipolar system. In an isothermal condition, the dipolar material ejects heat Q=TΔS to the surrounding, where T is the temperature and ΔS is the isothermal entropy change. Alternatively, in an adiabatic process, to keep the total entropy of the materials constant, the temperature of the dielectric is increased by ΔT, the adiabatic temperature change which is related to $Q=c\Delta T$ where c is specific heat capacity of the dielectric. In a reverse process, as the applied electric field is reduced to zero and the dipoles return to the less ordered state (or disordered state), an increase in the entropy of dipolar system occurs, and under an isothermal condition, the dielectric will absorb heat Q from the surrounding.

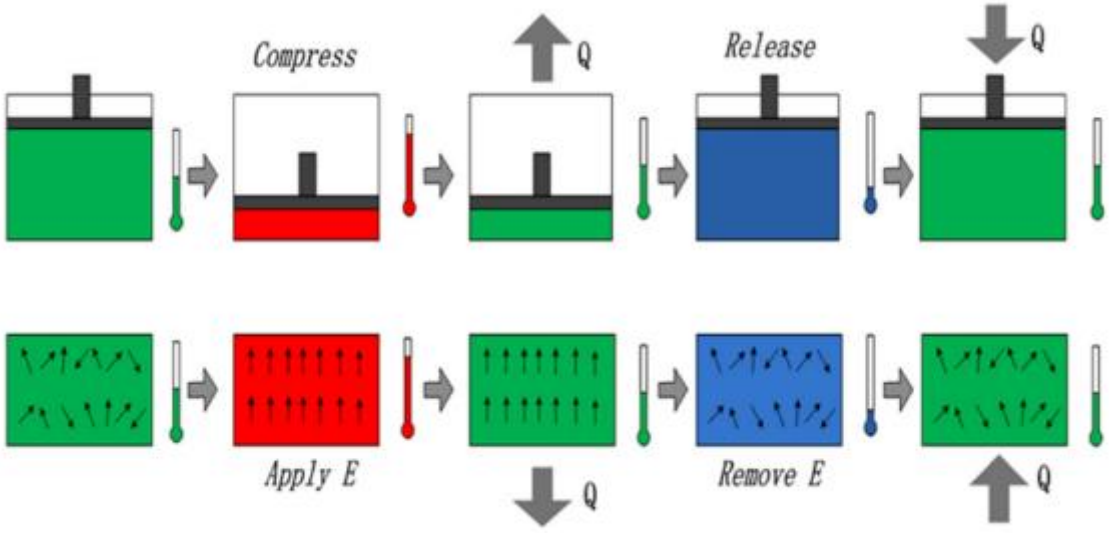

*Figure 1-3. Comparison of the electrocaloric cooling cycle (bottom) with that of the traditional vapor(*10*)*

1.2 Recent Progress on Electrocaloric Materials

For Electrocaloric cooling, the electrocaloric material is a crucial part and the starting point for the EC cooling system design. The adiabatic temperature change and the heat of ECE decide the performance of EC devices as heat is pumped through the EC materials. Electrocaloric effect (ECE) has been known in Rochelle salt since the 1930s(*11*). But not till the discovery of the giant electrocaloric effect that shines lights to practical applications(*3*, *4*, *12*).

The Heckmann diagram illustrating the thermodynamic reversibility interactions that may occur among the thermal, mechanical, and electrical properties of a crystal(*13–15*). The general forces are in the outer circles denoted by *E*, *T*, and θ. Moreover, the general displacements are expressed by the points of the inner triangle with *D, S* and σ. The lines between the points refer to the corresponding effects with the names marked. In the Heckmann diagram, the electrocaloric effect corresponding to the link between entropy and electrical field. The pyroelectric effect, which describes the electrical polarization change with temperature, is another property between thermal and electrical parameters.

To achieve a sizeable electrocaloric effect, a significant entropy change rising from the polarization of materials is necessary. Besides, the dielectric material should respond effectively to the external field. Ferroelectric materials, which consist of many dipole domains, are candidates to have the electrocaloric effect. At temperature just above Curie temperature, where ferroelectric (polarization ordered) – Paraelectric (polarization disordered) phase transition (FE-PE), where the most significant electric field-induced polarization change in a material can be achieved. Various materials have been studied for their ECE, from ceramics to polymers.

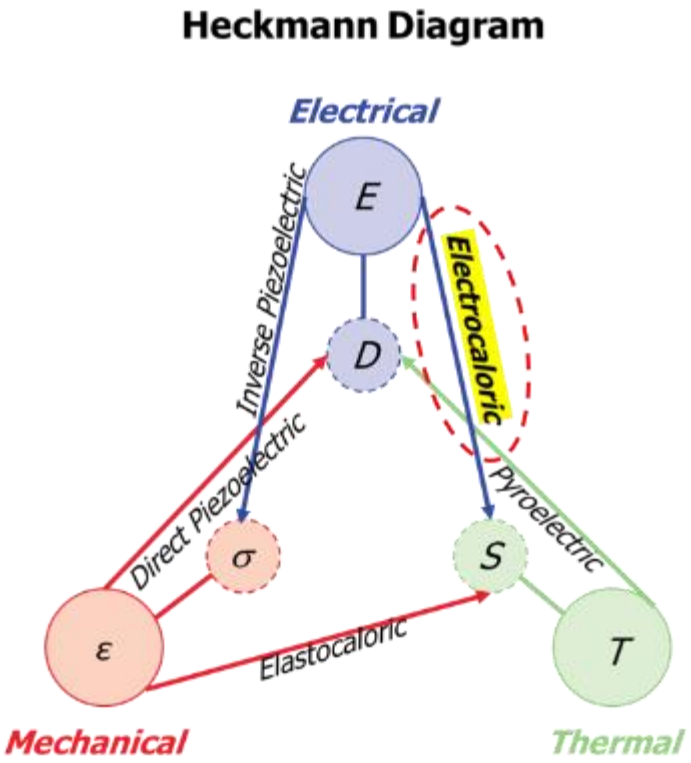

Figure 1-4. Heckmann diagram

1.2.1 EC ceramics film

The Giant ECE was first reported in ferroelectric ceramic films. In 2006, Mischenko et al. demonstrated a giant electrocaloric effect of 0.48 K per volt in a 350-nanometer thick $PbZr_{0.95}Ti_{0.05}O_3$ (PZT) film around 222 ^oC. An adiabatic temperature change of 12 K was reported under an electric field of 48 *MV/m*. The PZT nanofilm was fabricated through the sol-gel method. Due to the thickness of the sample, it was impractical to measure the EC temperature change directly through thermocouple or Infrared camera. A modified polarization measurement method was used to study the ECE in this research. A Maxwell relation $(\frac{\partial \mathrm{P}}{\partial \mathrm{T}})_E = (\frac{\partial \mathrm{S}}{\partial \mathrm{E}})_T$ was used to derive the EC temperature change. The discovery of

giant ECE in perovskite ceramics gained a lot of attention from scientists eager to develop alternative environment-friendly cooling technologies.

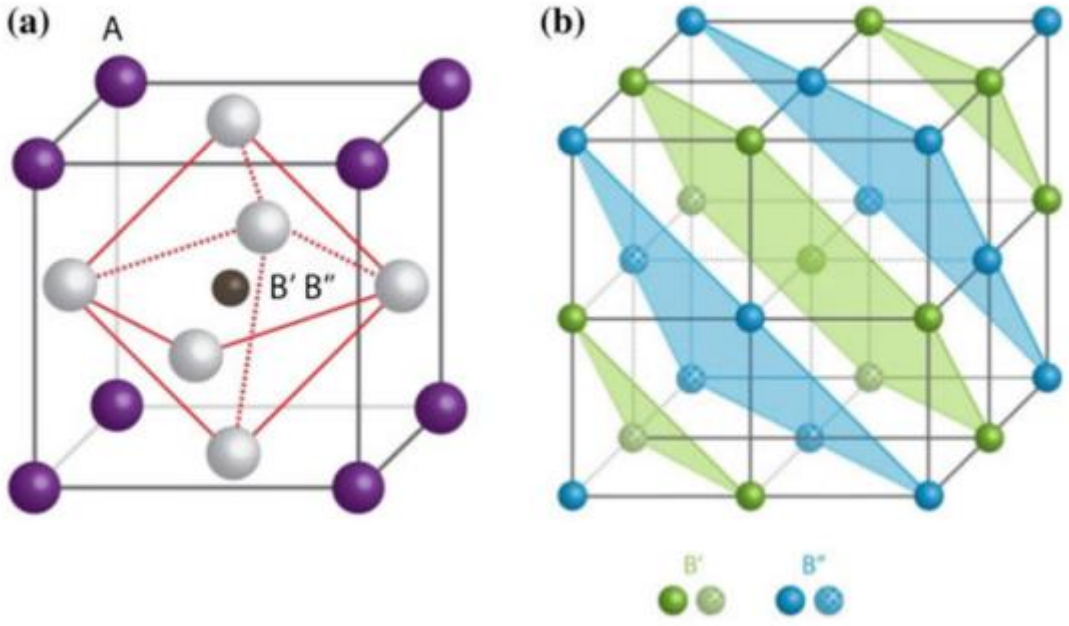

*Figure 1-5.(a) Schematic diagram of A(B',B'')O_3 perovskite structure. (b) Double perovskite crystalline structures(*9*)*

However, the high working temperature limited applications of electrocaloric ceramics. An effort has been made to decreasing EC ceramic working temperature to room temperature by introducing the substitutional atoms. The substitutional atoms allow the tuning of ferroelectric (FE) – paraelectric (PE) phase transfer temperature (Curie temperature)(*16–18*). ECE is largest at a temperature a little above Curie temperature. Also, in normal ferroelectrics, the FE-PE transition temperature range is quite sharp, which leads to the narrow working temperature(*19*). Ferroelectric relaxors, like PMN (Pb(MgNb)TiO_3), exhibits a diffused FE-PE transition around -13 ^oC. A temperature change of 2.5 K was reported around room temperature. Lead-free ceramics such as BST ($Ba_{0.73}Sr_{0.27}TiO_3$),

NBiTi($Na_{0.5}Bi_{0.5}TiO_3$) and $Ba_{0.3}Na_{0.7}Ti_{0.3}Nb_{0.7}O_3$ were also investigated for their environmental friendliness(*20*, *21*).

1.2.2 EC multilayer capacitors

The report of the giant ECE in ceramic films stimulated the research on EC materials. However, most of the EC ceramic films are thinner than one micron. Limited by the low thermal mass, the films cannot pump a significant amount of heat. Moreover, the films are usually fabricated on substrates and impose a significant challenge on EC device integration.

A multilayer capacitor (MLC) is a type of capacitor constructed of two or more alternating layers of ceramics and a metal layer acting as the electrodes. It is the most produced and used capacitors in the electronic equipment, and there are around one trillion pieces shipped per year. EC MLCs have been reported by modifying the existing dielectric MLC fabrication process(*22*). Several properties make EC MLCs attractive to engineers when fabricating EC devices,

1. EC MLCs are fabricated by stacking multiple ceramics films together; therefore, no substrate is needed to support the EC materials, and therefore, little dead volume is introduced.
2. The thickness of each EC layer is thin (<50 microns), therefore the heat can be quickly transferred to the metal electrodes and dissipated away through the thermally conductive metal electrodes. The rapid heat dissipation enables a higher operating frequency.
3. Because of the developed supply chain and packaging process of the MLCs, it is feasible to fabricate EC MLCs with large electrode areas. Besides, since the

electrodes are embedded in the MLCs and not exposed to air. Therefore, failure frequency due to arcing can be significantly minimized.

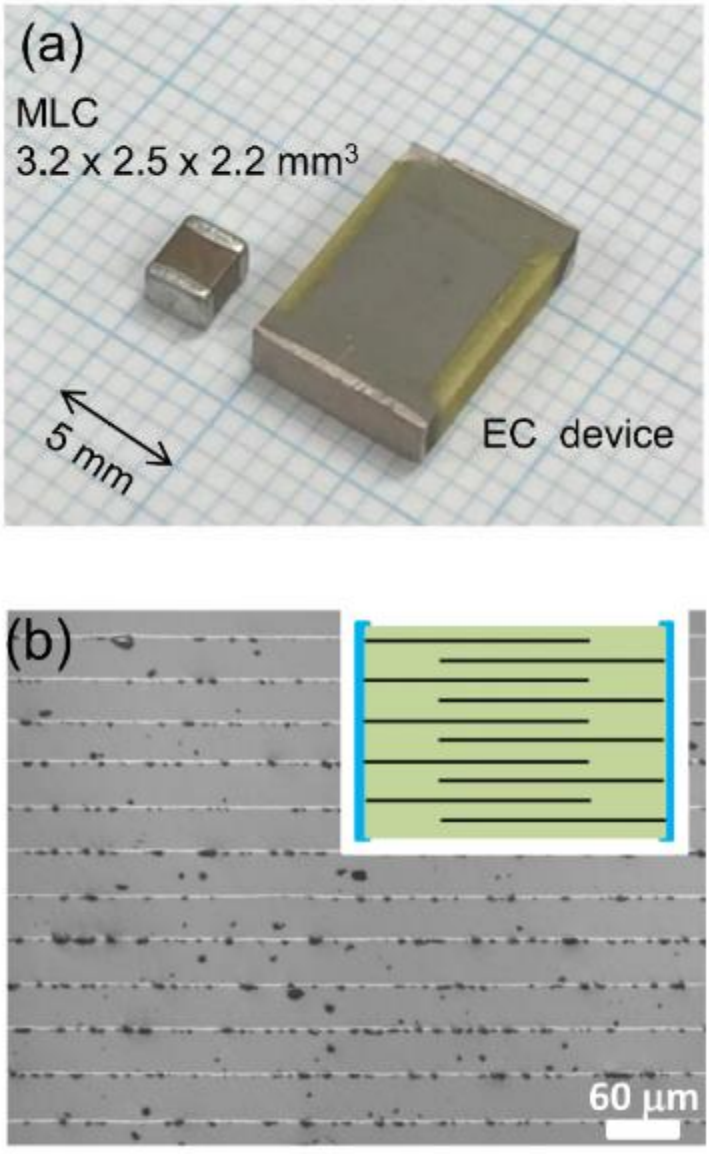

Figure 1-6. (a) Photograph of an EC MLC. (b) Cross-sectional optical microscopy image of the EC MLC(22)

1.2.3 EC polymers

Poly(vinylidene-difluoride) (PVDF) based polymers were first studied for their excellent electromechanical property and has been widely used for sensors and actuators(*23–26*). Five different crystalline phases have been reported of PVDF(*27, 28*). As shown in figure 1-7, the beta phase PVDF, in which, polymer chains are all-trans (TTTT) conformation, where all the fluorine atoms are on one side of the chain(*29*). Because of the significant difference between the electronegativities of F and H atoms, dipoles perpendicular to the chain directions is formed. Moreover, the beta phase shows the ferroelectric property. In contrast, the alpha phase of PVDF consisting of random arrangement of fluorine atoms. The phase transformation from the beta phase to the alpha phase indicates a change from an ordered state to a disordered state, which leads an increase in entropy.

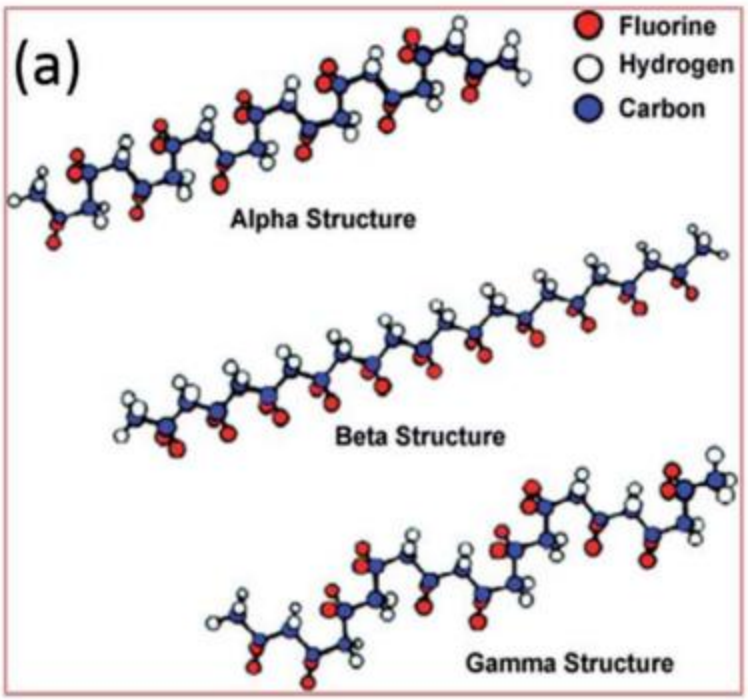

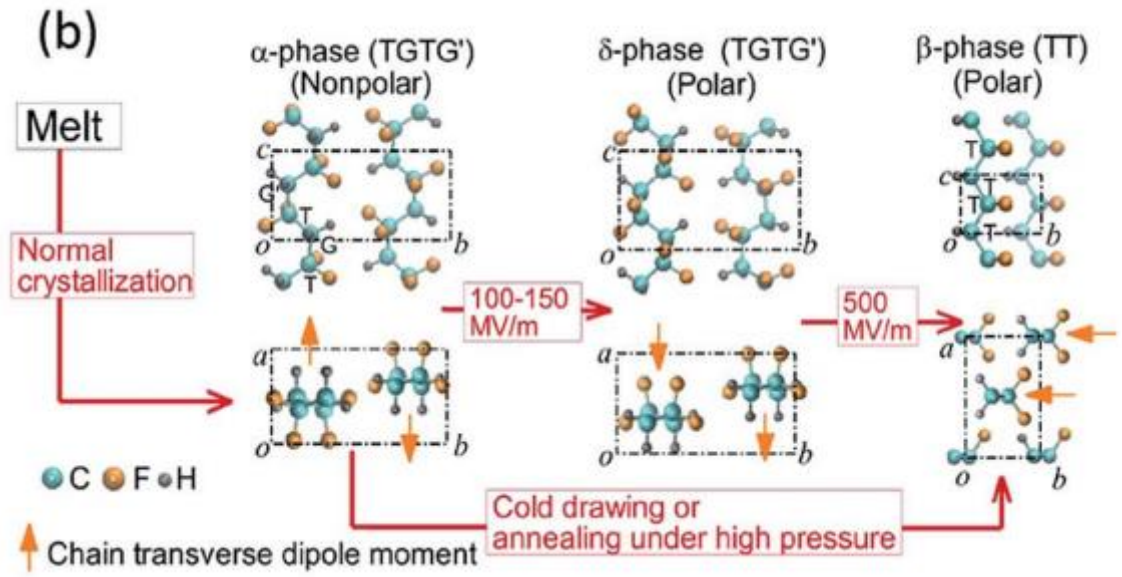

*Figure 1-7. Diagrams of (a) the three primary polymorphic crystalline phases of PVDF. (b) Electric field-induced phase transitions of PVDF(*29*)*

However, pure PVDF does not experience an FE-PE transition, even when the temperature rises to the melting point. By introducing trifluoroethylene (TrFE) unit into the PVDF chain, the curie temperature of the polymer can be tuned. Figure 1-8 shows the phase diagram of PVDF/P(VDF-TrFE) copolymer(*30*). When TrFE monomers consist of more than 20% of total repeating units, the Curie temperature is lower than the melting point, and we can achieve the FE-PE phase transition around for that P(VDF-TrFE) copolymer. As TrFE units increase, curie temperature keeps decreasing and reaches around 60 ^{o}C when TrFE is around 50%.

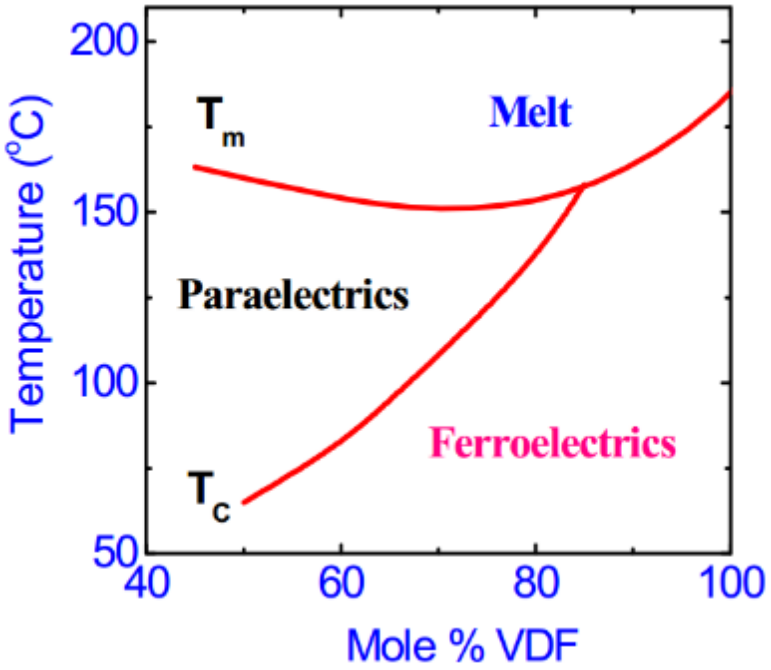

*Figure 1-8. P(VDF-TrFE) phase diagram(*30*)*

Around the curie temperature, the thermodynamic barrier between the ferroelectric phase and the paraelectric phase can be overcome by the presence of an external electric field. Paraelectric to ferroelectric phase transformation corresponds to a disorder to order phase transition. Therefore, we can control the phase transition of EC materials by applying the electric field. The latent heat of this FE-PE transition can be utilized. For P(VDF-TrFE) 68/32 mol % copolymer, a phase transition heat of 2.1×10^4 J/kg is yielded.

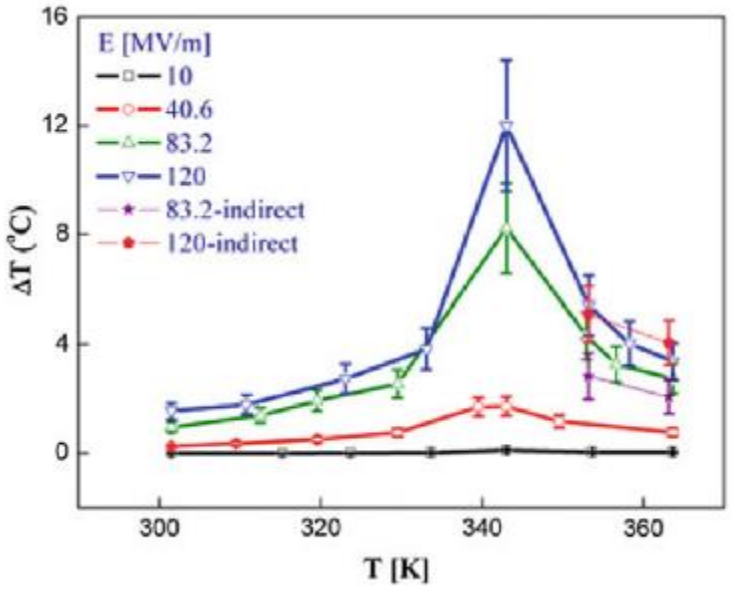

*Figure 1-9. Directly measured Temperature change as a function of temperature under several electric fields for unstretched P(VDF-TrFE) 55/45 mol % copolymers and comparison with that indirectly measured(*31*).*

In 2011, Lu et al. reported an EC temperature change of 12 K based on P(VDF-TrFE) copolymer around 345 K(*31*). However, as shown in figure 1-9 when operating temperature moves away from Curie temperature, the EC adiabatic temperature change decreases sharply. For P(VDF-TrFE) copolymers, the Curie phase transition temperature is usually higher than 50 ^{o}C, which makes it is impractical to use P(VDF-TrFE) copolymer for the room temperature cooling devices. Also, a high loss causing by hysteresis of P(VDF-TrFE) copolymer limits the efficiency of EC devices based on it.

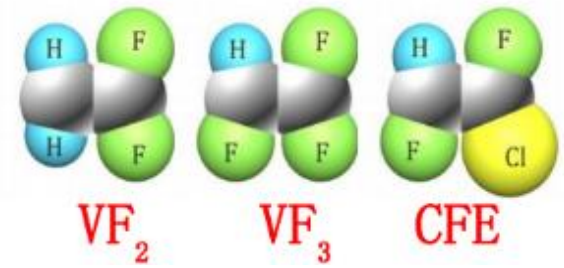

Figure 1-10. VF2, VF3 and CFE units

By defect modification, such as high energy irradiation or copolymerizing with a third bulky monomer, P(VDF-TrFE) ferroelectric polymer can be converted to a relaxor ferroelectric and therefore reducing the transition temperature and avoiding the hysteresis. As shown in figure 1-10, VF2 unit and VF3 unit are in similar size. Chlorofluoroethylene (CFE) unit, which contains a bulkier chlorine atom, is much larger than the former two. VF2 and VF3 are highly polar and provides crystalline structures that are essential in the ferroelectric phase. CFE units, in the other way, break the crystal structure. The normal ferroelectric polymer can be converted into relaxor ferroelectrics, and nano-polar microdomains exist. Neese et al. reported a giant ECE of P(VDF-TrFE-CFE) around room temperature(*4*).

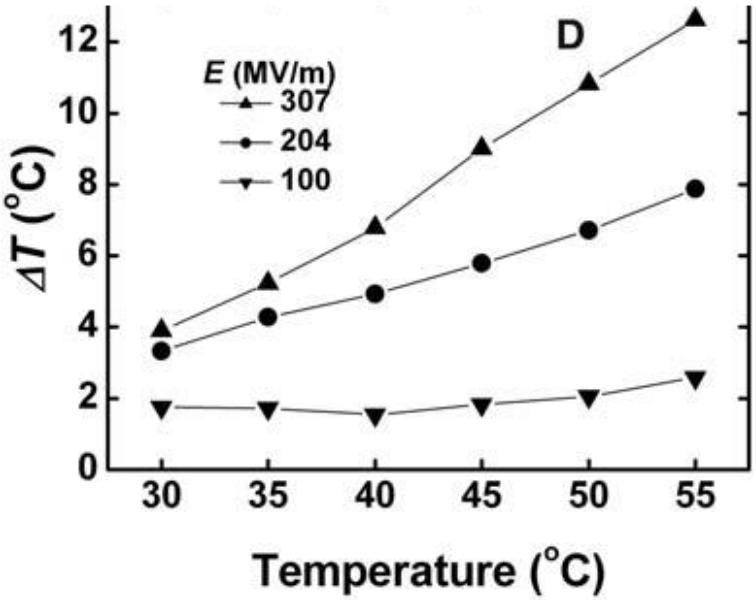

*Figure 1-11. EC temperature change of the P(VDF-TrFE-CFE) terpolymer(*4*)*

1.2.4 Electrocaloric nanocomposites

Electrocaloric nanocomposites which combine the advantages of both electrocaloric polymer and ceramics show some promising results in some recent reports. Zhang et al. fabricated an electrocaloric active nanocomposite with 10 vol % of Barium Strontium Titanate (BST) in P(VDF-TrFE-CFE) polymer matrix. The nanocomposite shows an enhanced temperature change of 20 K under 100 MV/m(*32*).

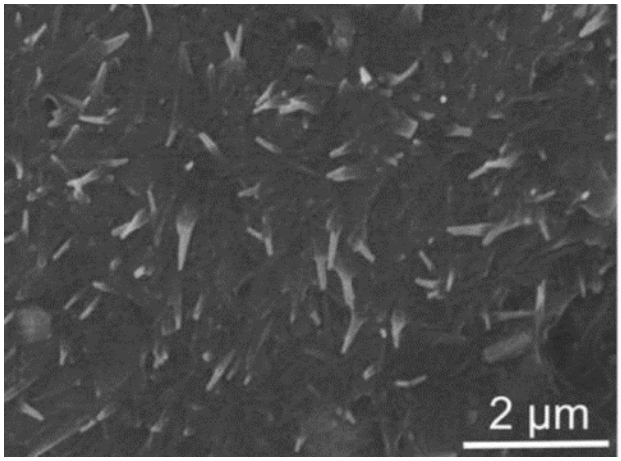

Figure 1-12. SEM of P(VDF-TrFE-CFE) and BST nanocomposite.

These reports demonstrate the potential to produce EC materials with temperature change larger than 10K under room temperature. The improvement of EC response is because of the interfacial coupling effect between the polymer and ceramic nanofillers(*19*, *33*). However, there is no EC device reported utilizing the nanocomposites even the temperature change is auspicious. It is still challenging to fabricate large area EC nanocomposite for EC devices.

1.3 Recent Progress on Electrocaloric Devices

1.3.1 Introduction to heat switches

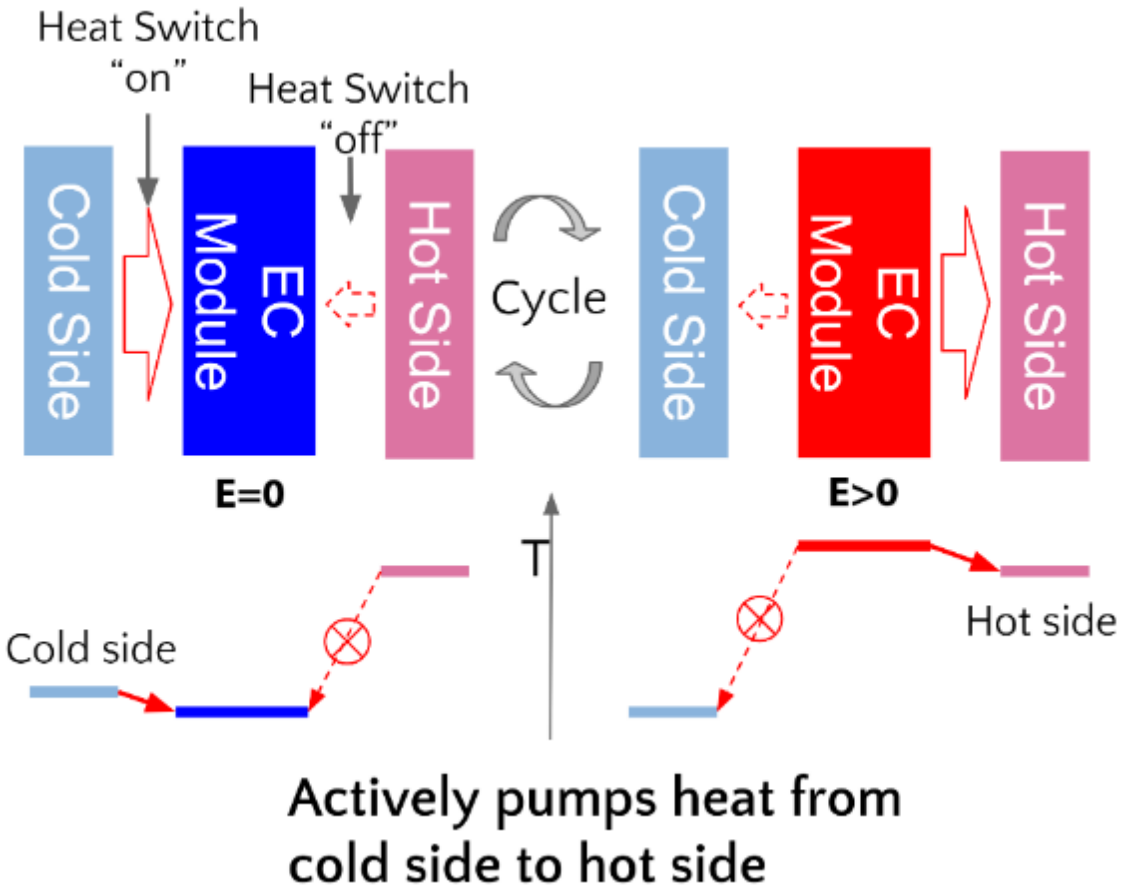

Figure 1-13. Illustration of an EC cooling system with heat switches

Unlike the rapid development of EC materials, the development of EC devices is still in its infancy and far away from making a massive impact on society. The heat switch is a necessary component to lay the foundation of the EC cooling devices. Unlike for thermoelectric materials, EC materials do not create directional constant heat flux. Instead, EC materials create a time-varying temperature driven by an external electric field. In a functional EC refrigeration system, the thermal connections between the EC layer and the hot and cold reservoirs need to be "on" and "off" synchronized with EC driving voltage.

As shown in Figure 1-13, when the EC layer's temperature at its minimum as a result of removing EC voltage, the heat contact between the cold side and EC layer is on, and heat can be transferred from the cold side to the EC layer. At the same time, the heat switch between the hot side and the EC layer is off. Therefore the heat flux is minimized. Likewise, when the EC layer's temperature at its maximum as a result of applying EC voltage, the heat contact between the hot side and EC layer is on, and heat can be transferred from the EC layer to the hot side. At the same time, the heat switch between the cold side and EC layer is off; therefore, heat flux to the cold side is minimized. The system cycles between these two states, and the net heat flux is from the cold side to the hot side against the temperature gradient.

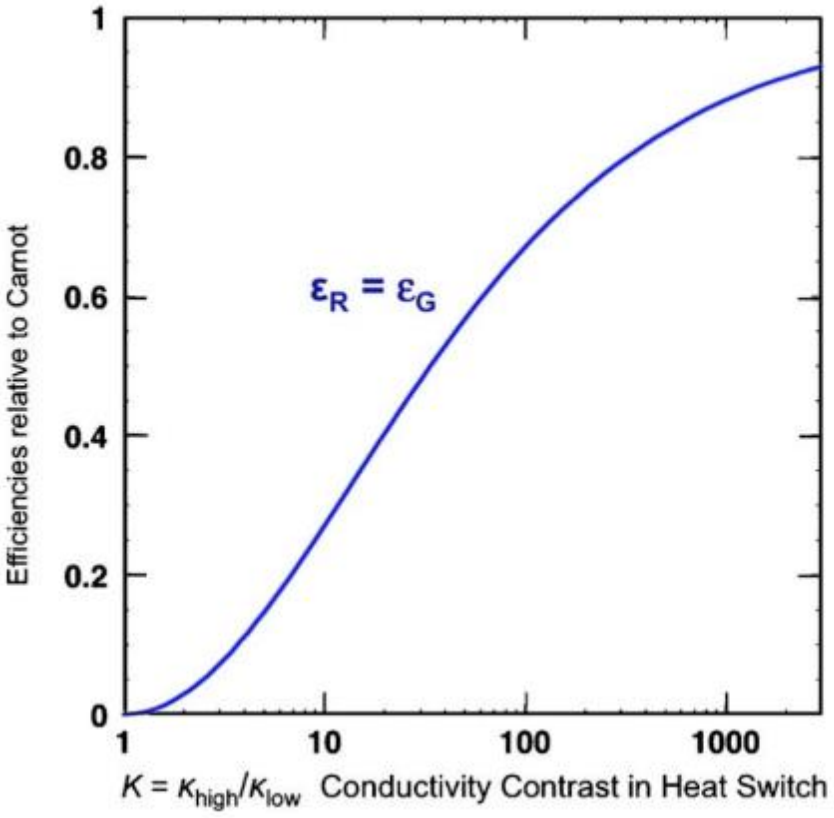

Figure 1-14. The efficiency relative to the Carnot values for both EC refrigerators

1.3.2 Liquid crystal heat switches

The on-to-off ratio of the heat switch is critical for the performance of the EC devices. Epstein et al. reported a theoretical modeling result of the relationship between heat switch on-to-off ratio and the device efficiency(*34*). When the ratio is higher than 100, the EC devices will have an efficiency superior to the vapor compression refrigeration system. There are several approaches that have been proposed. Liquid crystal molecules with anisotropic thermal conductivities offer the possibility of thin layer heat switches with fast response.

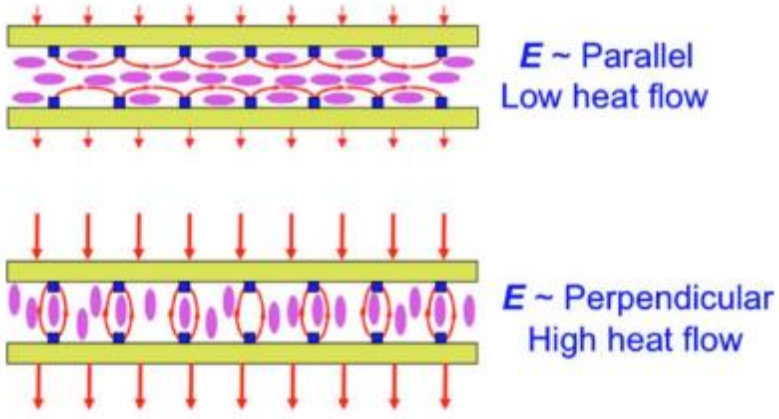

*Figure 1-15. Illustration of liquid crystal heat switch(*34*).*

1.3.3 MEMS based heat switches

However, it is challenging to identify a liquid crystal that can produce high on-to-off contract suitable for EC devices. Microelectromechanical systems (MEMS) are extensively studied and widely adopted in consumer electronics for their low power consumption and high robustness. Wang et al. reported a heat switch based on micro-machined silicon parts (Figure 1-17)(*35*). Comparing liquid crystal heat switch, the silicon heat switch has a much higher thermal contrast ratio, and the stiffness of silicon ensures the durability of the heat

switch. Jia et al. engineered switchable liquid-based thermal interfaces to enhance the thermal contrast(*36*). Glycerol was selected as the interface liquid for its relatively high contact angle on Teflon and low vapor pressure.

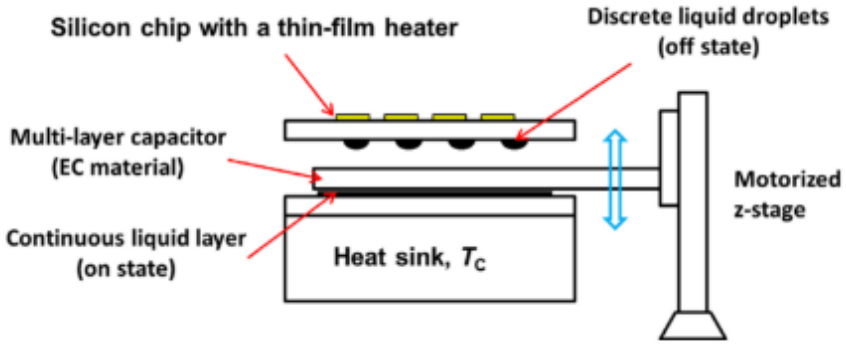

*Figure 1-16. A liquid droplet mediated heat switch(*36*).*

The prototypes mentioned above demonstrated the functionality of the various heat switches. However, the parasitic energy consumption to cycle the heat switch was non-trivial, and it is urgent to develop an EC device with energy-efficient and reliable heat switches which retain a high on-to-off ratio.

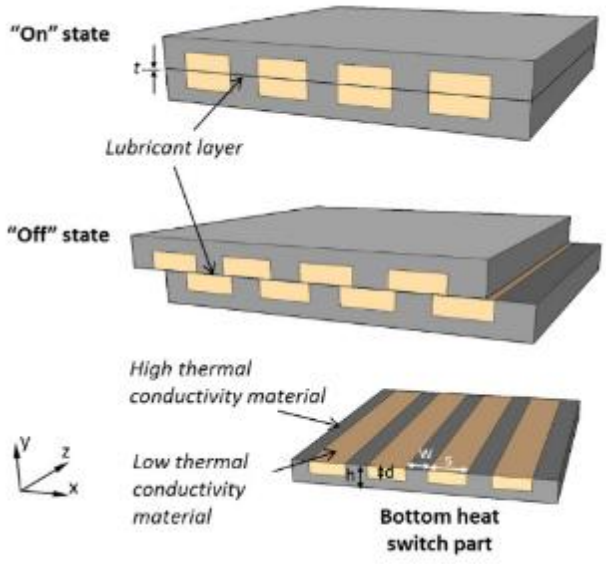

*Figure 1-17. Microchipped silicon heat switch(*35*)*

1.4 Wireless power transfer

1.4.1 Background

Wearable devices have been the focus of consumer electronic industry since the launches of a series of revolutionary products (such as Google Glass, Apple Watch, and AirPod). Over the past decades, the rapid development of electronics, materials, and telecommunication technologies enable the miniaturization of wearable electronics. Empowered by the ever-evolving micro-chips and low power sensor technologies, wearable devices become omnipresent in our daily life. Figure 1-18 presents some typical wearable devices.

Figure 1-18. Wearable devices(37)

Wearable electronics have evolved gradually in the form of accessories, integrated clothing, body attachment, and body inserts. As a computing platform, it emerges more and more important after television, personal computer, and mobile devices. The wide adaption of wearable electronics represents a great business opportunity. CCS Insight predicted that by 2019, the wearables market would be worth $25 billion, as shown in Figure 1-19.

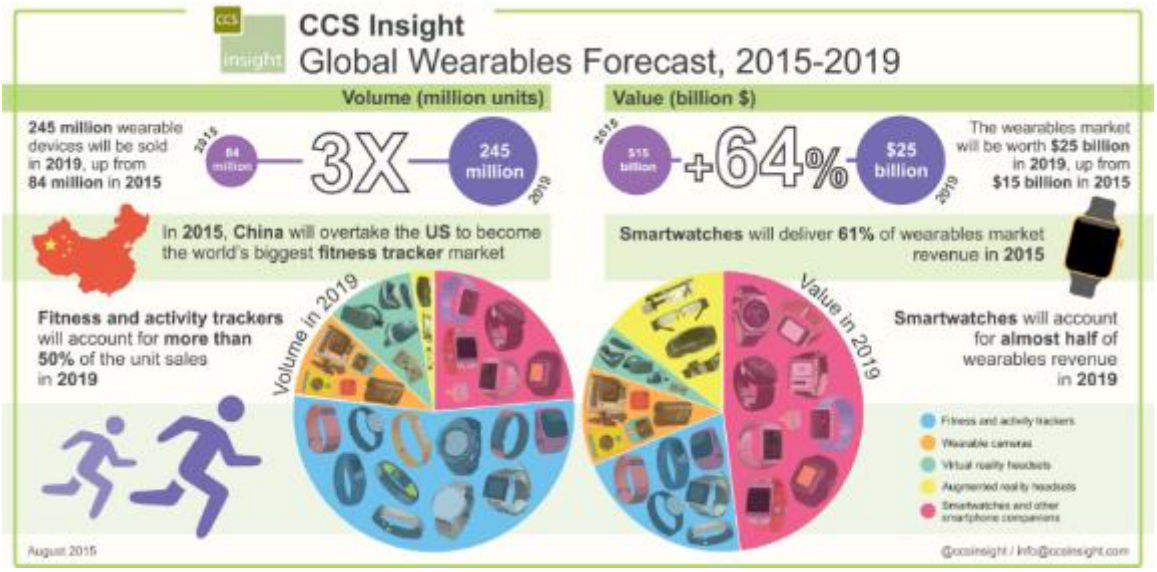

*Figure 1-19. Global wearable device market size. From CCS Insight. (*38*)*

However, the power supply for wearable devices seems to place a severe challenge to engineers. Short usage time and recurring charge of the wearable devices have been widely reported to be the factors that keep consumers away. Currently, most of the wearable devices are powered by a rechargeable battery. Limited by the small size and lightweight of the wearable devices, it is not feasible to integrate batteries with high capacity.

Wireless power transfer shows excellent potential as an energy supply method for wearable devices for its ease of integration and cheap cost. In 2007, Kurs et al. reported a wireless power transfer technology via magnetic resonances(*39*). Comparing to traditional wireless power transfer method, it demonstrated a long charging distance over two meters and maintained a high power (60 W).

1.4.2 Wireless power transfer (WPT) by magnetic induction

Wireless power transfer (WPT) is the transmission of electrical energy without physical conductive wires as a link(*40*). A typical WPT system includes four components (as shown in Figure 1-20),

1) Power source
2) Transmitting (Tx) coil
3) Receiving (Rx) coil
4) Load

A transmitting coil is driven by an alternating current (AC) provided by the power source to generate a time-dependent electromagnetic field. A power link is established between the transmitting coil and the receiving coil via inductive coupling. The time-varying voltage induced in the receiving coil is consumed by the load. Through this process, the power transfer is achieved wirelessly.

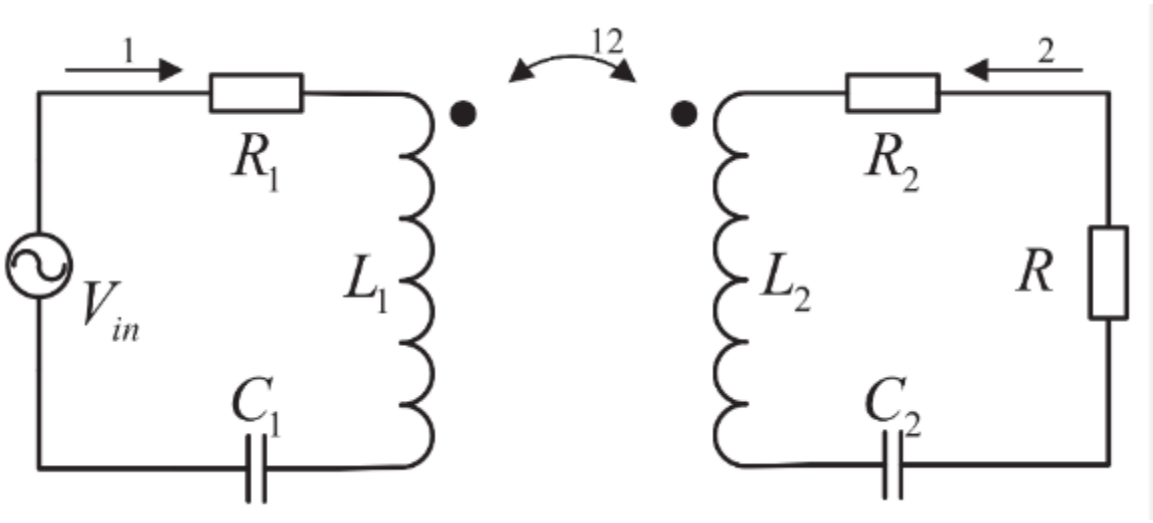

Figure 1-20. Equivalent circuit of a WPT system

In the inductive coupling WPT, the Tx and the Rx coils form a transformer. The AC in the Tx coil creates an oscillating magnetic field (B) by Ampere's law. The Rx picks the oscillating magnetic field, and an alternating electromotive force is induced by the Faraday's law of induction. The electrical energy wirelessly transferred dependents on the mutual inductance ***M*** between Tx and Rx and operation frequency. Capacitors are usually used to tune the resonant frequency of the system. Details will be discussed in Chapter 4.

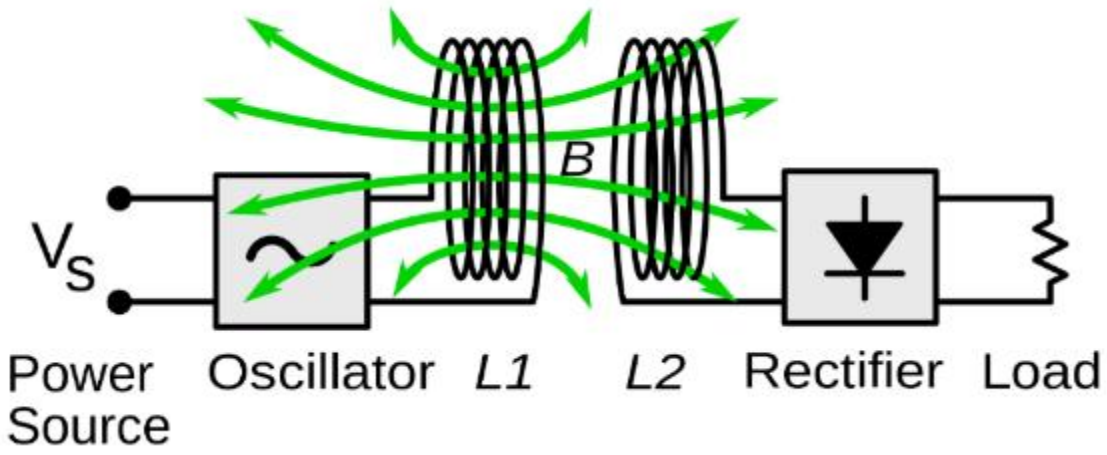

*Figure 1-21. Generic block diagram of an inductive wireless power system(*41*)*

1.4.3 Stretchable AgNW conductor

Tx and Rx coils are critical components of a WPT system. As mentioned in the previous section, the energy wirelessly transferred is directly related to the physical properties of the coils, such as resistance and size. Currently, the Litz wires are excellent as commercially available coils. The Litz wire coils demonstrate good conductivity and suitable for high-frequency applications (as shown in Figure 1-22)(*42*). However, the coils are stiff and cannot fit well to be embedded in wearable devices worn next to the skin. Also, with the rapid development of virtual reality and augmented reality, wireless charging for devices with display becomes the desired feature. Metal wires may block users' vision and introduces tremendous challenges for engineers during integration. To address this issue, mechanically stretchable and optically transparent wireless charging coils are needed for wearable electronics.

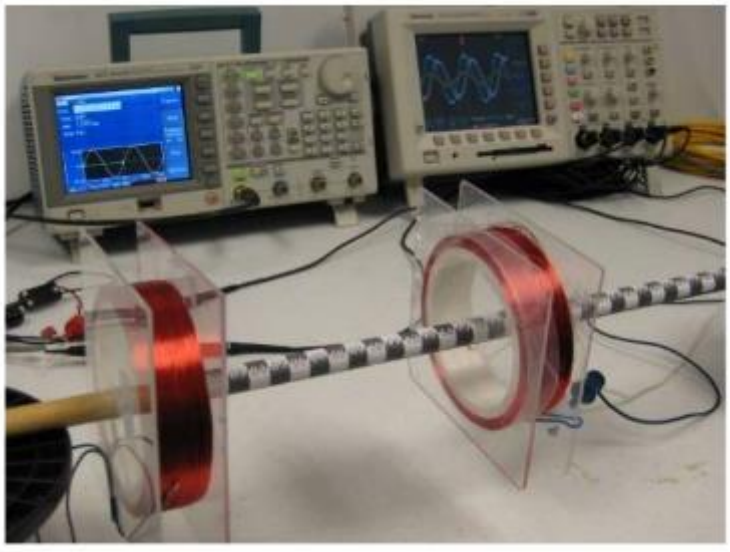

*Figure 1-22. Transmitting and receiving coils(*42*)*

In light of stretchable transparent conductor, silver nanowire (AgNW) has emerged as a candidate and garnered significant attention for applications in applications including organic light emitting diodes (OLED), thin-film transistors (TFT), organic photovoltaics (OPV), and electronic skins(*43*). AgNW forms a percolation network that allows charge carriers (electrons) conduct through. Our group pioneered the integration of AgNWs and stretchable polymer composites to develop stretchable electrodes with excellent optical properties. Yu et al. fabricated a stretchable transparent conductor by incorporating the AgNW network in a transparent polyacrylate elastomer. The AgNW network acts as the electrical conducting back-bone and provides an excellent electrical conductivity while maintaining high transparency(*44*). Hu et al. improved the performance of the AgNW/acrylate composite by adding an aromatic monoacrylate (Sartomer CN131) and acrylic acid (AA) to the precursor(*45*). The presence of carboxylic acid groups allows a good bonding between AgNWs and the polymer matrix, enhances the stretchability and durability of the as-fabricated transparent conductor.

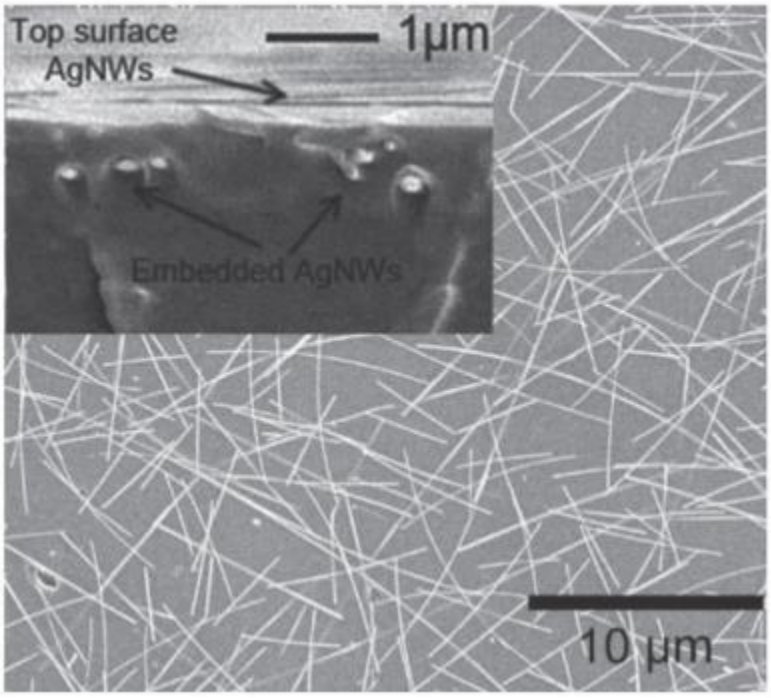

*Figure 1-23. Silver nanowire network in polyacrylate(*46*)*

1.5 Motivation and research scope of the dissertation

The development of EC technologies shows a promising future for EC cooling. However, it is necessary to point out that the electrocaloric technology is still in its early stage and requires efforts from both material and system sides. System design and reliability are two of the biggest hurdles limit EC technology from mass-scale adoption of EC technology. The previously reported heat switches experience low on-to-off ratio and consume a significant amount of parasitic power. Through EC nanocomposites exhibit substantial temperature changes, it is still challenging to develop large-area samples which

are required in EC devices. Therefore, it is of great interest to attack the problem from both material and system perspective.

The dissertation is divided into five chapters.

Chapter 1, the current chapter, gives an overview of the research field, including the overview of cooling technologies, the introduction of electrocaloric effect and other alternative cooling technologies, and the background of power supply for wearable electronics.

Chapter 2 covers the development of electrocaloric materials and measurements. Polyvinylidene fluoride (PVDF) based polymers are studied for their excellent electrocaloric performance and ease of processing. Since the first discovery of the Electrocaloric effect, its characterization poses a challenging problem for scientists for the small overall heat effect and high operating voltage. To measure the adiabatic electrocaloric temperature changes, experiments were designed, and both indirect measurement and direct measurement were studied.

Chapter 3 covers the material research effort to develop crosslinked P(VDF-TrFE-CFE) with enhanced electrical and mechanical properties. A controlled dehydrochlorination reaction was developed. The crosslinked polymer exhibits improved performance in several metrics important to the applications of P(VDF-TrFE-CFE), including anti-solvent property, enhanced dielectric constant and mechanical strength. The yield strength of c-P(VDF-TrFE-CFE) is 22.90 MPa, and its tensile stress is 45.56 MPa. Unlike the pristine terpolymer which melts around 130 ^{o}C, the crosslinked terpolymer can survive up to 250 ^{o}C; it behaves like an elastomer above the T_m. Weibull analysis reveals an improved electrical reliability of the crosslinked terpolymer. The E_b of the crosslinked

terpolymer is 445 MV/m, higher than the 325 MV/m for the pristine terpolymer. Further investigation is ongoing to examine the potential application of c-P(VDF-TrFE-CFE) for capacitive energy storage and electromechanical actuation.

Chapter 4 discusses the invention of an EC cooling device which is enabled by an electrostatically actuated heat switch. The Reversible electrostatic force reduces parasitic power consumption and allows efficient heat transfer through good thermal contacts with the heat source or heat sink. The EC device produced a specific cooling power of 2.8 watts per gram and a coefficient of performance (COP) of 13. The new cooling device is more efficient and compact than existing surface-conformable solid-state cooling technologies, opening a path to using the technology for a variety of practical applications.

Chapter 5 shows a stretchable transparent conductor based on silver nanowires (AgNWs)-polyurethane acrylate (PUA) composite with high conductivity and robustness under harsh mechanical treatment. A 10.6 ohm/sq thin film has a transmittance of 84% and is still conductive under a mechanical deformation up to 60% tensile strain. The maximum power of 59 mW (power transfer efficiency ~ 24%) is transferred wirelessly at a distance of 2 mm. A green light-emitting diode (LED) was wirelessly powered to illustratively demonstrate the functionality of the system. The negative adhesive transfer printing (NATP) is developed for the fabrication of the transparent wireless charger.

Finally, Chapter 6 summarizes the work and provides an outlook for future research.

2 Electrocaloric Thin Film Based on P(VDF-TrFE-CFE)

2.1 Introduction

Since the first discovery of the giant electrocaloric effect in 2006, researchers have made significant achievements in developing electrocaloric materials with high adiabatic temperature changes(*3*). Zhang et al. reported a Barium Strontium Titanate (BST)/PVDF based electrocaloric nanocomposite with an adiabatic temperature change around 50 K(*47*) at room temperature. Qian et al. demonstrated a dielectric liquid crystal with a significant electrocaloric effect(*48*).

Though it has been more than a decade since the first discovery of the giant electrocaloric effect, only a few electrocaloric cooling devices have been reported. It is beneficial to understand what the challenges and necessary materials requirements are. First of all, it is essential to have a material with significant temperature, and it has been the main focus of material research over the past decades. Second, to effectively transport heat flux, the active size or volume of the EC unit should be considerable. However, in the past research, most of the reported work is based on materials with an active area of millimeter level. Also, because a higher voltage is required to apply across the EC materials. The electrical reliability, especially for large samples, is challenging. Our material development effort is around these challenges to develop EC materials that can be used in EC devices.

PVDF based polymer was selected for its high EC response. Comparing to inorganic EC materials, EC polymer is compatible with the solution process method and ready for large scale fabrication. Unlike the PZT ceramic, its optimal operating temperature is around

room temperature. In addition, the PVDF based polymer is stable under a high electric field which is beneficial for long term device reliability.

2.2 Experimental Section

2.2.1 Synthesis of P(VDF-TrFE-CFE)

In this research, P(VDF-TrFE-CFE) terpolymer is used for is excellent EC performance and good processability. P(VDF-TrFE-CFE) terpolymer is synthesized using a suspension polymerization process by Piezotech (France). The process of synthesis P(VDF-TrFE-CFE) terpolymer is a radical polymerization process including(*49–51*),

1. Initiation:
    a. peroxide generated radical: $\mathrm{RO-OR} \rightarrow 2\mathrm{RO}\cdot$
2. Chain propagation:
    a. $2\mathrm{RO} + \mathrm{VDF} \rightarrow \mathrm{ROH} + \mathrm{VDF}\cdot$
    b. $\mathrm{VDF}\cdot + \mathrm{TrFE} \rightarrow \mathrm{VDF-TrFE}\cdot$
    c. $\mathrm{VDF-TrFE}\cdot + \mathrm{CFE} \rightarrow \mathrm{VDF-TrFE-CFE}\cdot$
3. Chain termination:
    a. $(\mathrm{VDF-TrFE-CFE})_n\cdot + \mathrm{VDF}\cdot \rightarrow (\mathrm{VDF-TrFE-CFE})_n - \mathrm{VDF}$

Potassium peroxodisulfate is a typical initiator for this reaction.

The product received is washed by the Soxhlet extractor with deionized water and ethanol as solvent repeatedly to remove impurities. Since P(VDF-TrFE-CFE) terpolymer is insoluble in water and ethanol, the ionic impurities are removed, and the polymer remains.

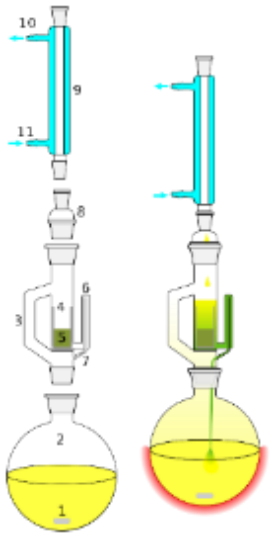

*Figure 2-1. A schematic representation of a Soxhlet extractor 1: Stirrer bar 2: Still pot (the still pot should not be overfilled and the volume of solvent in the still pot should be 3 to 4 times the volume of the soxhlet chamber) 3: Distillation path 4: Thimble 5: Solid 6: Siphon top 7: Siphon exit 8: Expansion adapter 9: Condenser 10: Cooling water out 11: Cooling water in(*52*)*

2.2.2 Fabrication of electrocaloric samples

Solution casting and spin coating methods were used to fabricate the EC thin films. The terpolymer of P(VDF-TrFE-CFE) (63.2/29.7/7.1 mol%, Piezotech Arkema group) was dissolved at 10 wt % in 2-Butanone (Spectrum Chemical) by stirring for two hours until the polymer was fully dissolved. The solution was filtered using a PTFE filter with a pore size of 0.2 μm and degassed using a bath-sonicator. Then spin coating EC polymer solution onto clean ITO glass for 1 minute, by changing the speed and time, thin films with different thickness can be yielded. After spin coating, anneal the film on a hot plate at 120 ^{o}C for 2 hours to remove solvent and improve crystallinity. 120 nm Al electrode was evaporated as designed as shown in figure 2-2

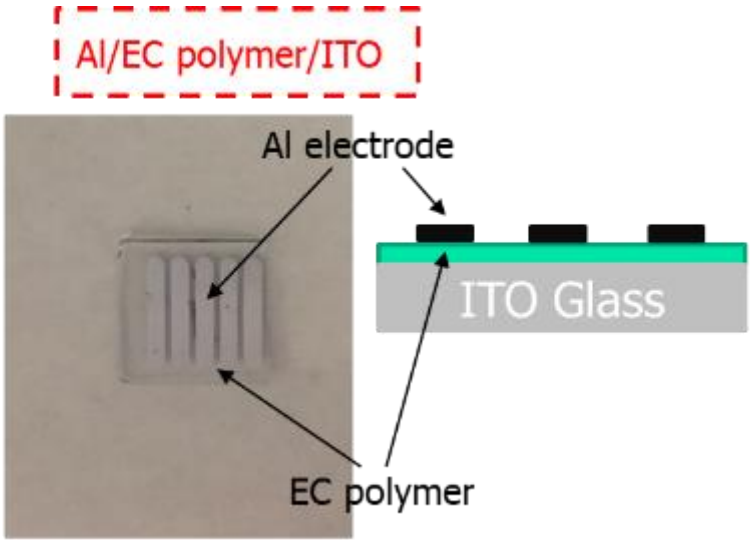

Figure 2-2. Illustration of P(VDF-TrFE-CFE) thin film on ITO glass

Table 2-1. Control thickness of spin coating thin films by concentration and spin speed

thickness/nm		speed/rpm		
		1000	2000	3000
Concentration	5% wt	470	410	290
	12% wt	3980	2750	2600

Solution Process of

To maximize the temperature change of electrocaloric material, we need to minimize the heat loss into the environment. Therefore, it is critical to fabricate free-standing P(VDF-TrFE-CFE) terpolymer films. Choi et al. developed a method of fabricating PVDF based polymer with PDMS as a substrate(*53*). The bonding between PVDF based polymer and glass is easily tuned by adding water. Therefore, we can firstly fabricate a thin film of P(VDF-TrFE-CFE) on glass and then debonding to yield free-

standing P(VDF-TrFE-CFE) thin film. The modified fabrication process of the free-standing EC film is as shown in figure 2-3.

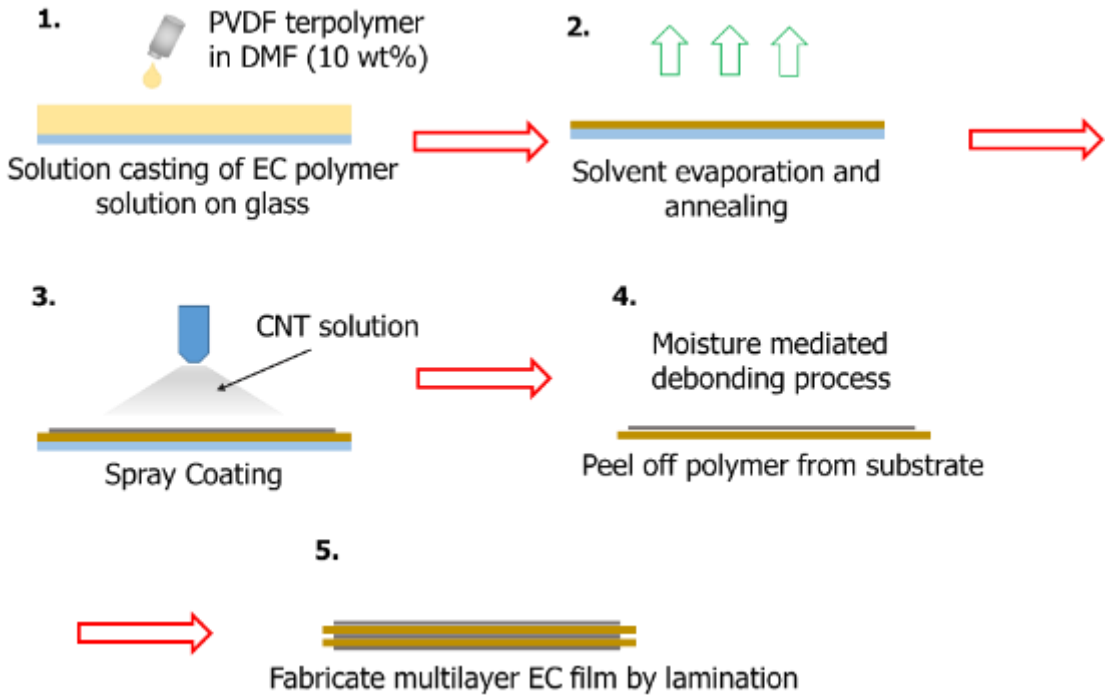

Figure 2-3. The fabrication process of free-standing EC films and the picture of the free-standing EC film

I. Solution casting: solution casting of the P(VDF-TrFE-CFE) on a clean glass substrate, by varying the concentration of the solution, films with different thickness can be fabricated.

II. Solvent evaporation: after solution casting, anneal the film in a vacuum oven at 120 ^{o}C for 2 hours to remove solvent and improve crystallinity.

III. Bonding of a supporting frame on top of the dry PVDF-based thin film.

IV. Hydration to weaken interfacial adhesion between the PVDF-based thin film and the glass plate by diffusion of water molecules along with the interface.

V. Debonding of the PVDF-based thin film together with the supporting film from the glass plate.

2.2.3 Fabrication of multilayer EC film

To increase the cooling power of electrocaloric materials, it is also necessary to build multilayers structure. We have developed a layer by layer coating method to fabricate multilayer free-standing electrocaloric polymer.

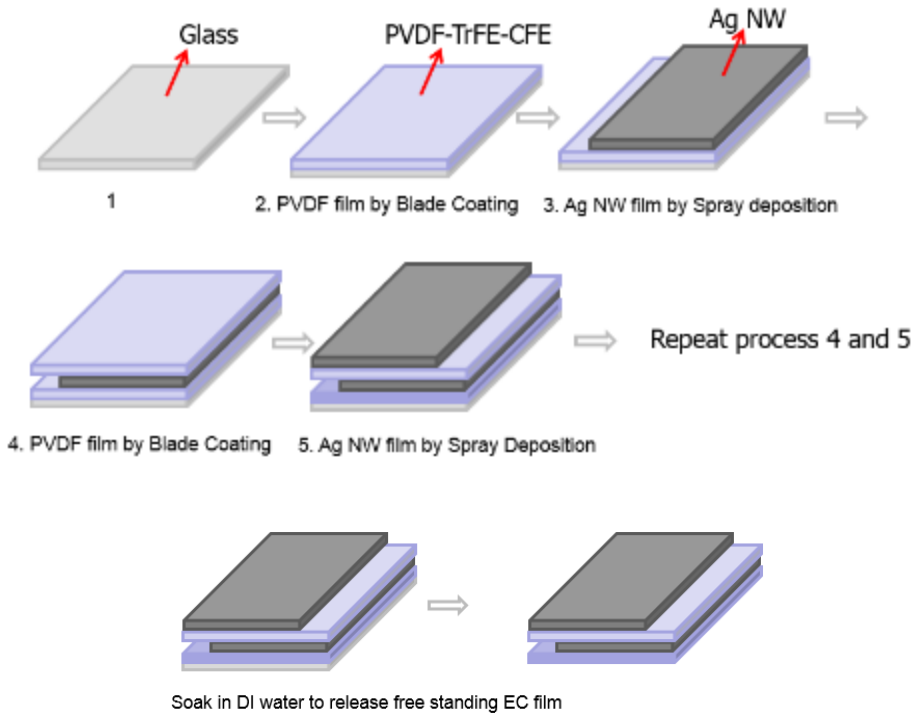

Figure 2-4. Method to fabricate multilayer free-standing electrocaloric polymer.

Figure 2-4 explains the process to fabricate the multilayer structure of the electrocaloric polymer. Here electrode can be AgNW, CNT or their mixture sprayed on to the polymer. Figure 2-5 shows the appearance of a multilayer electrocaloric polymer. EC polymer is transparent and flexible.

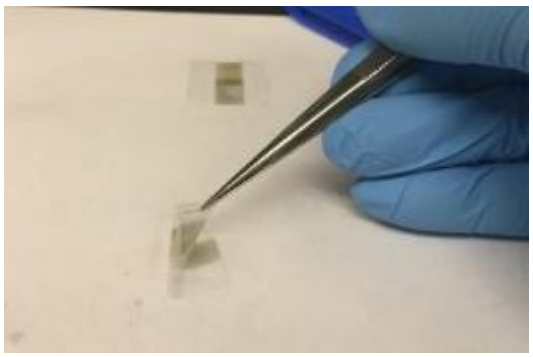

Figure 2-5. Multilayer P(VDF-TrFE-CFE) terpolymer with Silver nanowire as electrodes

2.3 Result and Discussion

2.3.1 Differential scanning calorimetry (DSC)

Differential scanning calorimetry (DSC) is an effective method to study the phase transitions of materials. Figure 2-6 shows the DSC of the PVDF terpolymer at a heating rate of 10 K/min. The positive direction of the y-axis represents an endothermic direction. The melting point of the terpolymer is 129 ^{o}C. it provides a reference temperature for materials annealing. The melting enthalpy is - 20.4 J/g, and we can estimate a crystallinity of the terpolymer to be around 60%.

It shows a broad curie transition peak around room temperature, which indicates the ferroelectric to paraelectric transition occurs across a broad temperature range and corresponds to the large EC performance of the terpolymer at room temperature.

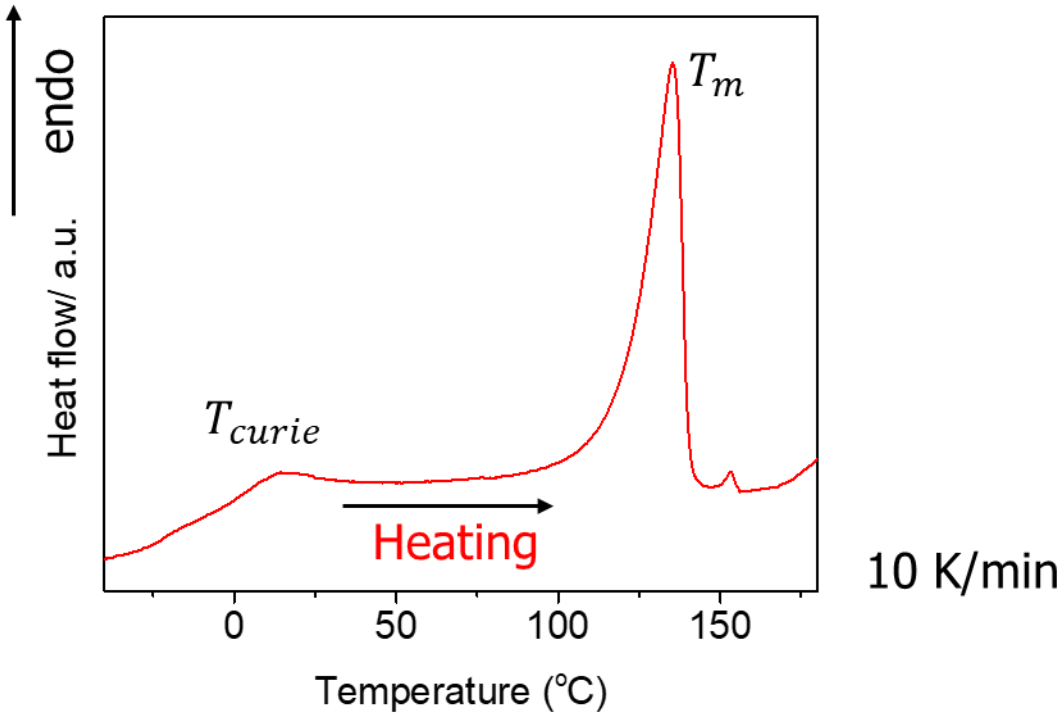

Figure 2-6. DSC of P(VDF-TrFE-CFE), heating rate = 10 K/min

2.3.2 Atomic Force Microscope (AFM) of EC film

The surface morphologies of the P(VDF-TrFE-CFE) thin film can be represented by the Atomic Force Microscopy (AFM) images. Below are topography images of the P(VDF-TrFE-CFE) terpolymer thin film surface. The left image shows the surface of the free-standing film facing glass when fabricated. The right image shows the surface of the free-standing film facing air instead. The samples showed rod-shaped crystallite structures. The rod is about 500 nm long and 50 nm wide. There are some pores on the surface facing air due to the evaporation of the solvent. The size of the crystallite is a good indicator of the coherence length of the terpolymer.

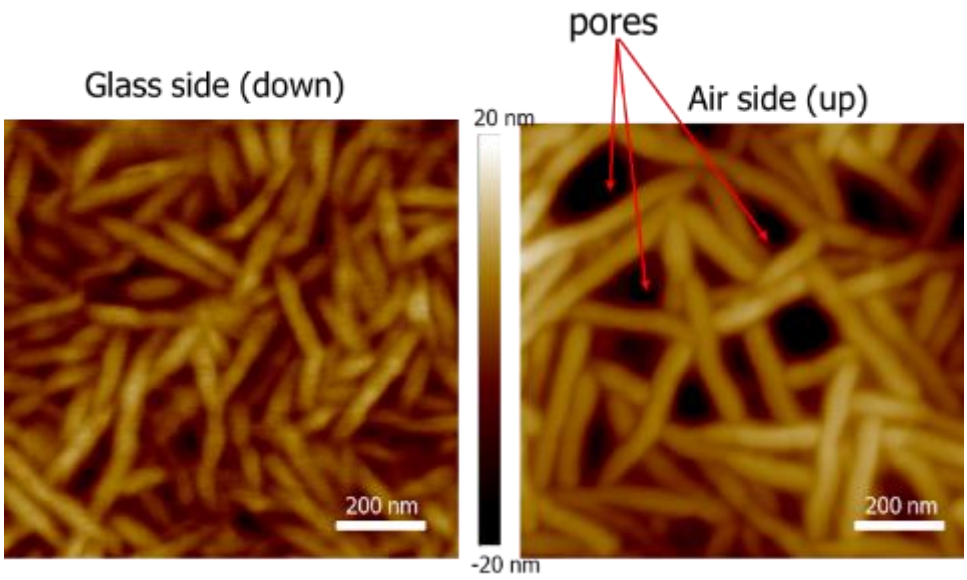

Figure 2-7. AFM image for the P(VDF-TrFE-CFE) terpolymer

2.3.3 Annealing process and X-ray Diffraction (XRD)

The annealing process plays an essential role in the P(VDF-TrFE-CFE) terpolymer's EC performance. For the electrocaloric applications, the crystalline size is critical since the dielectric, and the electrocaloric properties of the EC polymers rely on the polarization phase switching under the external electric field. A smaller crystalline size may contribute to a smaller energy barrier for the dipole orientation and result in a more significant polarization under a specific electric field(*54*). Also, a proper annealing process can enhance the crystallinity in the EC polymer and effectively improve the EC performance. Therefore, it is necessary to study the effect of the annealing process on the EC performance of P(VDF-TrFE-CFE) terpolymer.

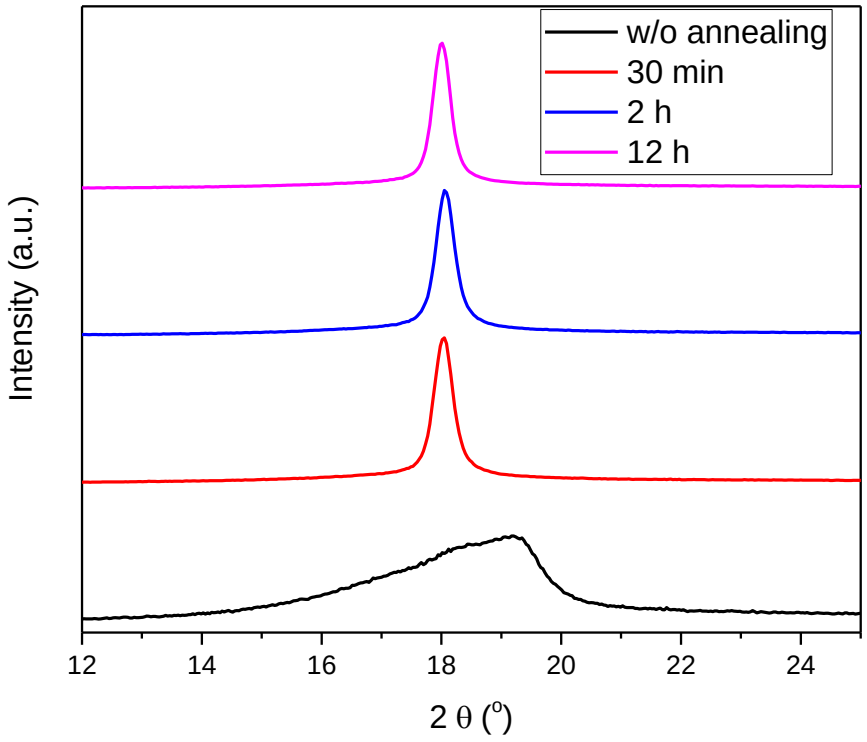

Figure 2-8. X-ray diffraction patterns of the P(VDF-TrFE-CFE) terpolymer with different annealing history

To study the phase compositions of the terpolymer, X-ray diffraction (XRD) was conducted. The P(VDF-TrFE-CFE) terpolymer film for XRD characterization is fabricated via the procedure described previously. Four samples with different annealing times were characterized, and the annealing temperature was 120 °C. The sample without annealing showed a broad peak of around 19.6°. The relatively low intensity and broad peak indicate a low crystallinity of the terpolymer without proper annealing. After annealing for 30 minutes, 2 hours, and 12 hours, the terpolymer exhibits one peak at 18.1°. According to Bragg's equation,

$$n \cdot \lambda = 2d \cdot sin\theta$$

where n is a positive integer, λ is the wavelength of the x-ray used, d is the interchain lattice space to measure, and θ is the incident angle. The as-fabricated terpolymer has an interchain lattice distance of 4.95 Å. Bao et al. reported a relationship between annealing process and ferroelectric relaxor behavior of PVDF based polymers(*55*). An interchain crystal space (d) of 4.95 Å reflects the terpolymer after annealing has a disordered 3/1 helical structure and TG/TG' conformation(*56*). For the terpolymer sample vacuum-dried at room temperature without further thermal annealing process, labeled as w/o annealing, the ferroelectric-like phase becomes predominant as indicated by the broad peak around 19^o - 20^o.

The Scherrer's equation is a good method to estimate the crystallite sizes (L) of the terpolymer.

$$L = 0.9\lambda/(Bcos\theta)$$

where λ is the wavelength of the x-ray, B is the full width at half the maximum of the peak (FWHM), and θ is the Bragg's angle. The crystallite sizes for the samples with no annealing, 30 minutes annealing, 2 hours annealing, and 12 hours annealing are 3.05 nm, 20.06 nm, 22.47 nm, and 23.41 nm respectively. The crystalline sizes are plateaued after 30 mins annealing.

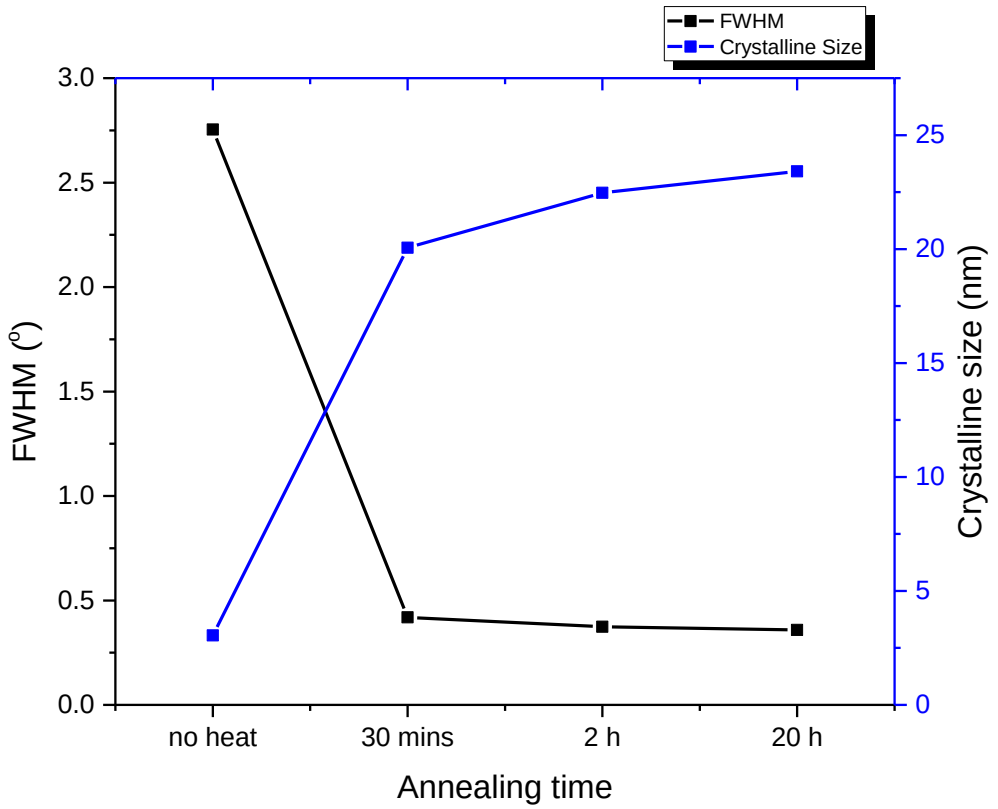

Figure 2-9. The full width at half the maximum of the peaks (FWHM) and crystalline sizes of P(VDF-TrFE-CFE) terpolymer with different annealing times

2.3.4 Indirect measurement of EC effect

Since the discovery of the ECE, its measurement has been a long-term focus of scientists. Due to the small thermal mass, it is challenging to measure the electrocaloric effect. General speaking, Electrocaloric effect measurement can be classified as two approaches, namely, indirect measurement and direct measurement. In indirect measurement, Maxwell's relation widely is used. By measuring polarization at a different temperature, entropy change and temperature change can be deduced. In direct measurement, the temperature change can either be recorded directly by Infrared camera or calculated from heat flux signal measured.

The indirect measurement of the electrocaloric effect is derived from the Maxwell relation, which relates the electrocaloric effect to the pyroelectric effect. The entropy change (ΔS) and the temperature change (ΔT) of electrocaloric materials which are represented as in the following equations.

$$\Delta S = -\int_{E_1}^{E_2} (\frac{\partial D}{\partial T})_E dE$$

$$\Delta T = -\frac{T}{\rho}\int_{E_1}^{E_2} \frac{1}{c_E} (\frac{\partial D}{\partial T})_E dE$$

where *D*=displacement of the dielectric materials sample under the electric field

E=electric field applied onto the sample

c_E=heat capacity of the dielectric material (specific heat)

ρ=density of the dielectric material

Following is the derivation of the previous equation

According to the first law of thermodynamics:

$$dU = TdS - PdV$$

Here *U* is internal energy, *P* is pressure, and *V* is volume; *dU* can be represented with total differentials form:

$$dU = (\frac{\partial U}{\partial S})_V dS + (\frac{\partial U}{\partial V})_S dV$$

Comparing 3-3 and 3-4 we have $T = (\frac{\partial U}{\partial S})_V$, P=-$(\frac{\partial U}{\partial V})_S$

$$\frac{\partial U}{\partial S}\frac{\partial U}{\partial V} = \left[\frac{\partial((\frac{\partial U}{\partial V})_S}{\partial S}\right]_V = \left[\frac{\partial((\frac{\partial U}{\partial S})_V}{\partial V}\right]_S$$

Substituting the values of *T* and *P*, we have a Maxwell relation:

$$\left[\frac{\partial P}{\partial S}\right]_V = -\left[\frac{\partial T}{\partial V}\right]_S$$

Similarly, for a dielectric material system in the electrocaloric effect, we assume there is no mechanical work but only electrical work. We also assumed it is an unstrained system under adiabatic conditions in thermal equilibrium. Therefore, we can express Gibbs free energy as

$$dG = -SdT - DdE$$

Here we can change two variables, namely electrical field and temperature, to yield the EC effect. Similarly, we have Maxwell relation $\left[\frac{\partial S}{\partial E}\right]_T = -\left[\frac{\partial D}{\partial T}\right]_E$. Therefore, with the above Maxwell relation, we can get

$$\Delta S = -\int_{E_1}^{E_2} (\frac{\partial D}{\partial T})_E dE$$

As we also know that

$$\Delta Q = -\Delta T * (c_E * \rho), \text{ and } \Delta Q = T * \Delta S = T^* \Delta S = -T \int_{E_1}^{E_2} (\frac{\partial D}{\partial T})_E dE$$

$$\Delta T = -\frac{T}{\rho} \int_{E_1}^{E_2} \frac{1}{c_E} (\frac{\partial D}{\partial T})_E dE$$

Therefore, as long as we measure the displacement change with electrical field and temperature, we can calculate the entropy and temperature change of the dielectric electrocaloric materials. Moreover, through analysis we found that a substantial polarization change with temperature is always desirable in order to achieve a sizeable electrocaloric effect, ferroelectric materials with high polarizations are candidates to investigate for electrocaloric effects. Meanwhile, a high breakdown field is crucial to harvest large ECE entropy change as the ordering of dipole units are controlled by the electric field. High electric field forces dipole units to arrange in order. EC polymers based on PVDF show their strength as their outstanding electrical stability.

The Displacement-Electrical field loops of P(VDF-TrFE-CFE) terpolymer were taken at room temperature with a frequency of 10 Hz. D-E loops with the maximum electric field of 100, 150, 200 and 250 MV/m were measured.

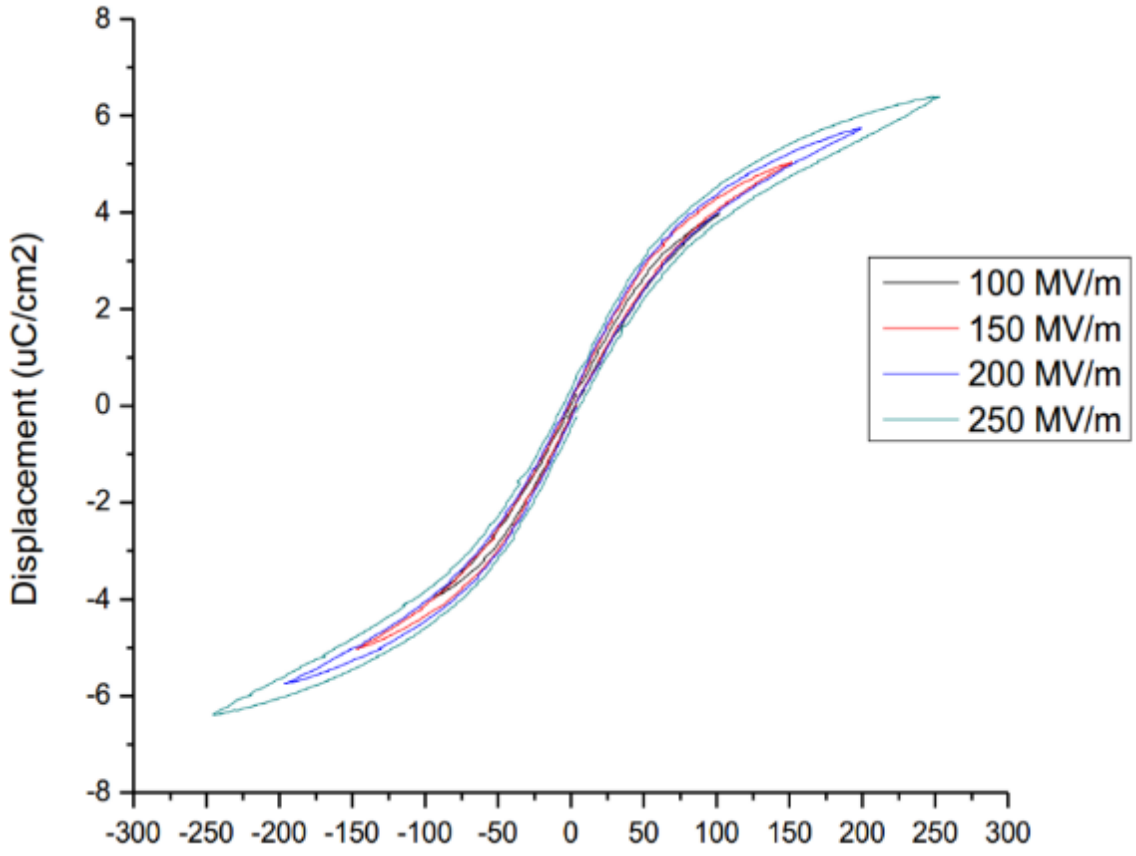

Figure 2-10. Hysteresis loop of P(VDF-TrFE-CFE) terpolymer under different electric field

Field strength	Loss (%)	Efficiency (%)
100 MV/m	8.1	91.9
150 MV/m	8.8	91.2
200 MV/m	8.9	91.1
250 MV/m	11.8	88.2

The EC temperature change of P(VDF-TrFE-CFE) terpolymer was measured indirectly by the Maxwell method. 2 micron P(VDF-TrFE-CFE) terpolymer was spin-coated onto ITO glass (1 by 1 cm). EC film was dried and annealed and ready for the measurement. As shown in figure 2-11, the displacement of the terpolymer decreases as the temperature increases. The physics behind this phenomenon is that as the temperature increase, the thermodynamic movement of the dipoles become more active and it will take a stronger electric field to reach the same level of polarization comparing to at lower temperatures.

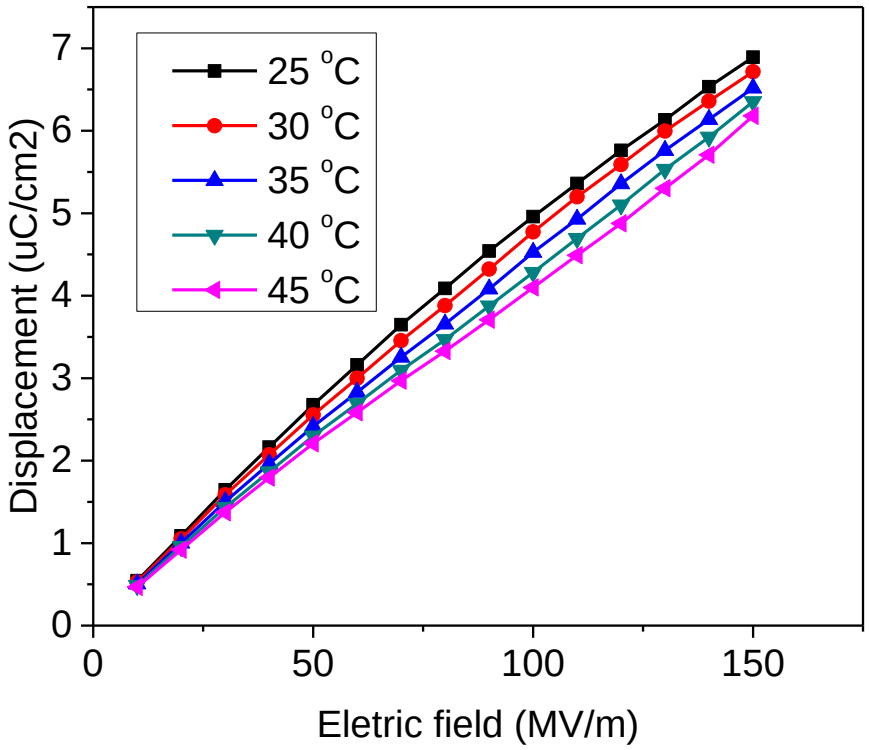

Figure 2-11. Displacement as a function of temperature

Figure 2-12 shows the temperature change measured by the indirect method under varying electric field and temperature.

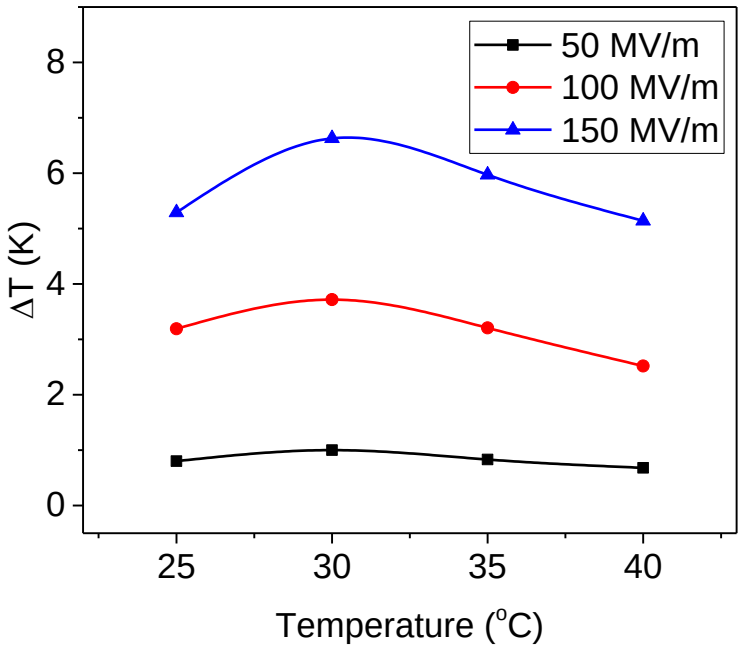

Figure 2-12. Indirect measurement of electrocaloric effect in different temperatures.

2.3.5 Direct measurement of EC effect

At the inception of the electrocaloric research, the indirect EC measurement has been beneficial for scientists to identify proper EC materials. Its easy set-up and few requirements on the sample size enabled the fast screening and developing of EC materials. However, the indirect EC measurement has its limits. It relies on the Maxwell equation and the accuracy of the measured temperature and displacement parameters. Also, in the indirect measurement, the specific heat of the EC materials is assumed to be constant under different electric fields which contradicts to reality. Compared to the earliest ECE investigation, direct ECE measure seems to be a straightforward task for the evaluation of the EC materials.

The direct measurement measures temperature change or heat flux generated by electrocaloric materials directly. It can be divided into two groups: temperature measurement and heat flux measurement. Up to now, there is no standard commercial equipment for electrocaloric measurement. Researchers have developed various systems to measure the electrocaloric effect directly. The direct methods can be further divided into two subgroups, namely the direct temperature measurement that detects temperature signal and calorimeter method that measures the heat flux signal.

A direct measurement records the temperature change of electrocaloric film by the infrared camera that was developed at UCLA. A 30 microns thick Free standing electrocaloric polymer (P(VDF-TrFE-CFE) terpolymer) was fabricated. Electrodes (carbon nanotube) was spray-coated onto both sides of EC film masked by PDMS. Kapton tape was used as a frame to hold the electrocaloric thin film.

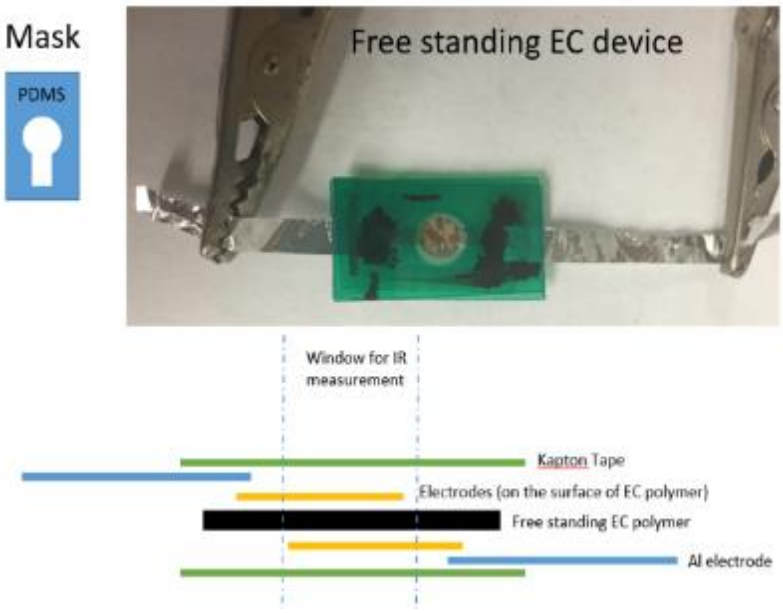

Figure 2-13. Illustration of direct electrocaloric effect measurement with infrared camera

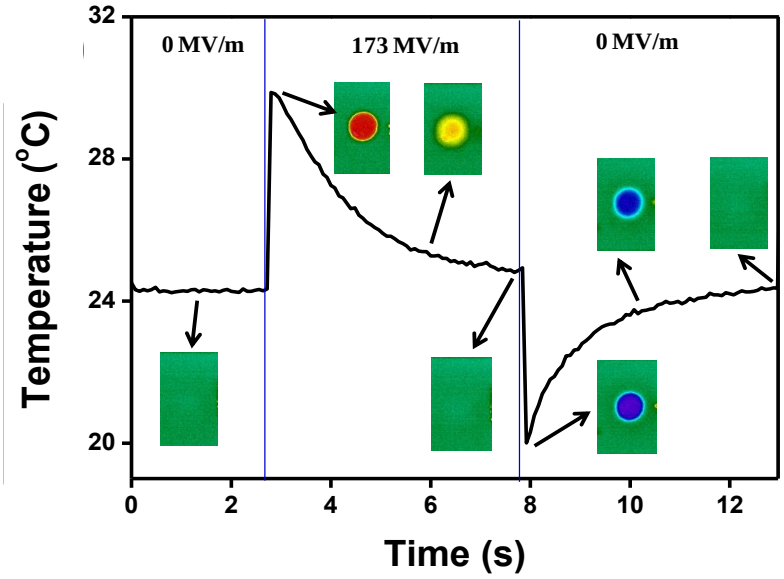

Figure 2-14. Temperature change as a function of the electric field, IR images were in the inset.

As shown in Figure 2-14, a peak temperature change of ~6 K for both cooling and heating can be achieved at 173 MV/m. When the electric field applied, the temperature jumped 6K immediately, and the lag is less than 0.1 s. For the cooling cycle, when the electric field was removed, the temperature of electrocaloric film decrease immediately 6 K within 0.1 s. Cycling test of temperature change at an electric field of 173 MV/m with a frequency of 0.1 Hz has been taken. As shown in figure 2-15, a total temperature difference of 12 K can be sustained even after 1 hour's test.

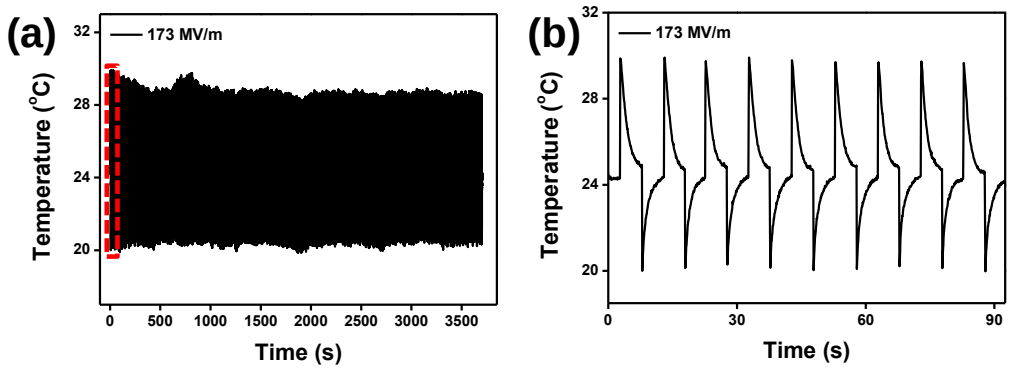

Figure 2-15. Cycling test of the temperature change as a function of electric filed (173 MV/m) with a frequency of 0.1 Hz up to 1 h.

The EC temperature change is field dependent. According to Landau-Devonshire Theory. The temperature change is a quadratic function of the electric field.

$$\Delta T = \frac{T\varepsilon_0}{2C}\left(\frac{d\varepsilon}{dT}\right)_{E=0} E^2$$

here T is the environmental temperature, C is the specific heat of the material, ε_0 is the vacuum permittivity, ε is the relative dielectric constant of the material, E is the electric field applied across the thin film. As we can see in this figure 2-16. The temperature change was only 1.3 at 50 MV/m, but increased significantly to 5 K around 83 MV/m.

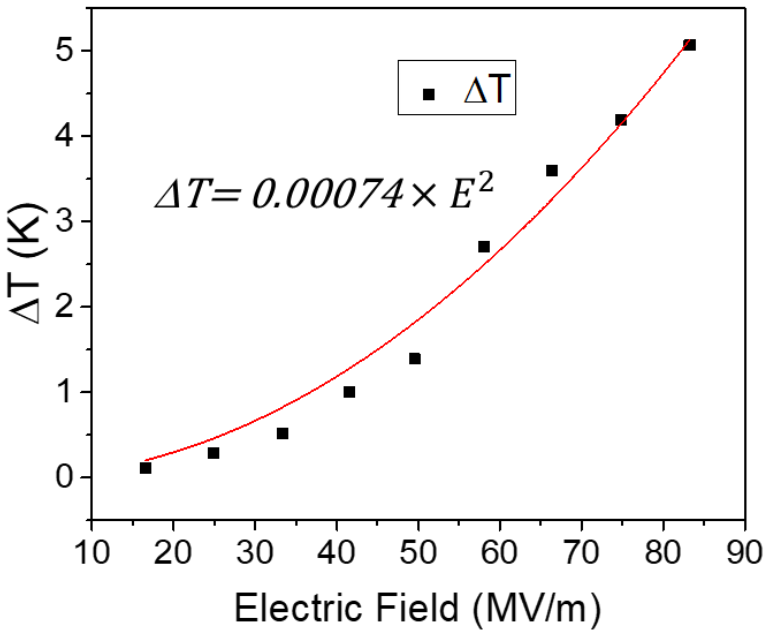

Figure 2-16. Measured Temperature vs electric field

2.4 Conclusion

In summary, the electrocaloric materials have been discussed in this chapter. To achieve a sizeable electrocaloric effect, a substantial entropy change rising from the polarization of materials is necessary. Besides, the dielectric material should respond effectively to the external field. Ferroelectric materials, which consist of many dipole domains, are candidates to have an electrocaloric effect. P(VDF-TrFE-CFE) is identified to be an excellent EC material for its high ECE temperature response and ease to process. Both direct and indirect methods were developed to characterize the EC materials. The Maxwell equations describe the relationship between the electrical displacement (D), the external electric field (E), and the temperature change (ΔT). The infrared camera has been widely used as a method for contactless temperature monitoring. Set-Up has been devised to measure the real-time EC temperature change directly. An EC temperature change of 6 K was observed in P(VDF-TrFE-CFE) terpolymer thin film with CNT as electrodes.

3 Crosslinked PVDF Terpolymer

3.1 Introduction

The rapid deployments of advanced electronics, electric vehicles, and power systems demand more and better performing energy-storage devices(*57, 58*). Among the various energy storage technologies, thin-film capacitors that store energy electrostatically on parallel electrodes and a dielectric spacer are characterized with fast charge/discharge rate, high power density, long cycle lifetime, yet very low specific energy density(*59*). The bi-axially oriented polypropylene (BOPP) capacitors represent the state-of-the-art film capacitors with ultra-high charge and discharge performance. Limited by the polymer's low dielectric constant (*K ~2.2*), BOPP-based capacitors achieve energy densities typically about 1-2 J/cm^3, which are several orders of magnitude lower than those of the batteries(*60*). Given the fact that capacitors take up to a quarter of the volume and weight of electric power systems, an improved energy density of the capacitors is directly translated to a reduction of the overall volume and weight of the power systems.

In general, the dielectric energy density (U_d) stored in a material is governed by the applied electric field (E) and the electric displacement (D), which is given by(*57*) $U_d = \int E\, dD$. For a linear dielectric material, such as BOPP whose dielectric constant is independent of the applied electric field, the energy density can be expressed as $U_d = \frac{1}{2}DE = \frac{1}{2}K\varepsilon_0 E^2$. where ε_0 is the vacuum permeability (8.85•10^{-12} F m^{-1}). To achieve a high energy density, it is critical to develop a dielectric material with both high breakdown field strength and high dielectric constant. Polymers are the preferred dielectric materials for its high breakdown field strength and low dielectric loss(*61*). However, the energy density of the dielectric polymers is limited due to their low *K (<10)*.

Poly(vinylidene difluoride) (PVDF)-based polymers are among the best-known polymers with high *K* values(*62–64*). In these polymers, a large polarization can be obtained because a large amount of 'C-F' bonds ensures a high dipolar density. The orientation and rearrangement of the dipoles in the crystalline phase contribute to large displacement response under external electric field(*65*). Chu et al. developed poly(vinylidene fluoride-co-trifluroethylene-co-chlorofluoroethylene) (P(VDF-TrFE-CFE)), a PVDF based terpolymer, which demonstrates a high energy density thanks to its high dielectric constant and relatively low polarization hysteresis(*63*). The terpolymer has also found other important applications, including solid-state cooling(*4*, *66*, *67*), electromechanical actuation(*24*, *25*, *68*), and non-volatile memory(*69*, *70*). In the P(VDF-TrFE-CFE) terpolymer, the CFE units are significantly larger than the VDF and TrFE units because of the introduction of a Cl atom. The CFE units frustrate the crystallinity of the terpolymer and produce relaxor ferroelectricity in the terpolymer. It effectively enhances the dielectric response of the terpolymer and improves the dielectric constant(*71*). On the other hand, the CFE units soften the polymer, leading to large-strain deformation under a high electric field. The electromechanical deformation distorts the resulting thin film capacitors and lowers the maximum electric field at which the terpolymer can be practically operated.

In this work, we investigated a method to functionalize and further crosslink P(VDF-TrFE-CFE) that overcomes the limitations of the terpolymer described above. P(VDF-TrFE-CFE) containing C=C double bonds (P(VDF-TrFE-CFE)-DB) in the polymer chain was synthesized through controlled dehydrochlorination catalyzed by an organic base, triethylamine (TEA). The C=C double bonds are thermally crosslinked with

the use of a peroxide. The resulting crosslinked P(VDF-TrFE-CFE), c-P(VDF-TrFE-CFE), exhibits promising properties such as improved breakdown field strength, anti-solvent property, and enhanced stiffness.

3.2 Experimental Section

3.2.1 Materials

P(VDF-TrFE-CFE) was purchased from Arkema and used as received. Dimethyl sulfoxide (DMSO, Sigma Aldrich, ACS reagent grade), benzoyl peroxide (BPO, Sigma Aldrich, ACS reagent grade), triethyamine (TEA, Sigma Aldrich, ACS reagent grade), N,N- dimethylformamide (DMF, Sigma Aldrich, ACS reagent grade) were used as received without further purification.

3.2.2 Synthesis of P(VDF-TrFE-CFE)-DB via controlled dehydrochlorination

P(VDF-TrFE-CFE)-DB containing C=C double bonds was synthesized from P(VDF-TrFE-CFE) following a reported procedure with modification(*72*, *73*). The dehydrochlorination reaction is illustrated in Figure 3-1. The typical procedure is as following, 2.0 g P(VDF-TrFE-CFE) terpolymer was dissolved by 60 mL DMSO in a flask and stirred. After the solution became clear, 1.5 mL triethylamine (TEA) was added slowly through a syringe. The reaction temperature was maintained at 50-60 ^{o}C for 20 h once the polymer was dissolved and the solution gradually turned yellow. The resultant mixture was precipitated in 5 vol% hydrochloric acid. Deionized (DI) water and acetone were used to wash the product repeatedly for three times and then the product was dried at room temperature under vacuum for 4 h.

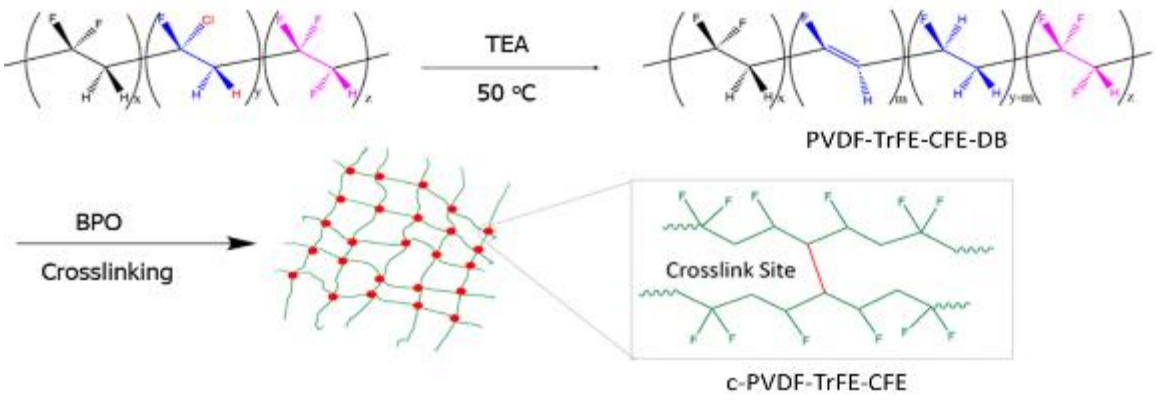

Figure 3-1. Scheme of the synthesis of P(VDF-TrFE-CFE)-DB and crosslinking reaction to form a network structure.

3.2.3 Synthesis of c-(PVDF-TrFE-CFE)

The resulting PVDF-TrFE-CFE-DB (0.5 g) was dissolved in N,N-dimethylformamide (DMF) at room temperature to afford a 10 wt% solution. Then, benzoyl peroxide (BPO, 5 mg) a free radical crosslinking initiator was added into the PVDF-TrFE-CFE-DB solution. The solution was kept stirred vigorously for 1 h. The solution was cast on a clean glass substrate and dried at 60 ^{o}C for 4 h in an oven. Finally, the film was cured at 120 C in a vacuum oven for 12 h to obtain the crosslinked terpolymer (c-P(VDF-TrFE-CFE)). The resulting polymer films was peeled off from the glass plate.

3.2.4 Characterization

^{1}H and ^{19}F NMR spectra were obtained using a Bruker 400 MHz spectrometer, and DMSO-D6 was used as the solvent. The mechanical tests were conducted by a dynamic mechanical analyzer (DMA, TA instruments RSAIII) at a constant displacement rate of 0.5 mm/s. The dielectric constant and loss were tested by an Agilent 4284A Precision LCR meter. The high voltage was supported by a high voltage amplifier (10/10B-HS, Trek). D-E loop of the EC fiber was measured at room temperature (TR66B, Radiant). The surface morphology of the substrates was analyzed with a Dimension Icon Scanning Probe

Microscope from Bruker (height mode). The crystal structure of P(VDF-TrFE-CFE) was recorded via X-ray diffraction (XRD, D8-GADDS, Bruker) with Cu Kα radiation at a scanning rate of 6° min^{-1} with 2θ ranging from 10° to 70°.

3.3 Result and discussion

3.3.1 Nuclear Magnetic Resonance (NMR) spectra

The synthesis of P(VDF-TrFE-CFE)-DB and c-P(VDF-TrFE-CFE) starting from commercially acquired P(VDF-TrFE-CFE) is illustrated in Figure 3-1. The dehydrochlorination of P(VDF-TrFE-CFE) could be carried out by treatment with thiethylamine, a weak nucleophilic agent. The chemical structure of the resulting P(VDF-TrFE-CFE)-DB containing C=C double bonds is confirmed by nuclear magnetic resonance spectra. On the ^{1}H NMR (Figure 3-2, 3-3), the multi peaks around 2.2-2.4 ppm and 2.5-3.4 ppm are related to the typical head-to-head and head to tail connection of the VDF units(*72*).

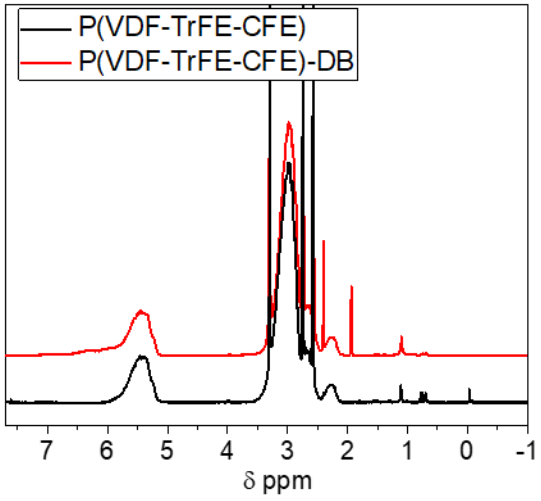

Figure 3-2. ^{1}H-NMR spectra of the original P(VDF-TrFE-CFE) and PVDF-TrFE-CFE-DB

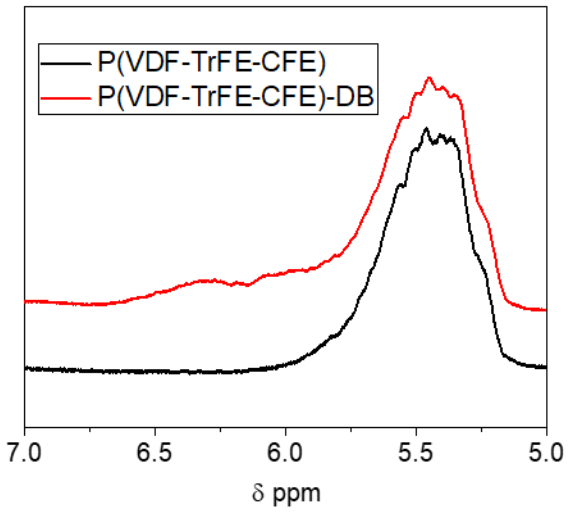

Figure 3-3. ^{1}H-NMR spectra of the original P(VDF-TrFE-CFE) and PVDF-TrFE-CFE-DB zoom in between 7.0 and 5.0 ppm. The shoulder peaks between 6.5 and 6 refers to the H atoms next to the double bonds.

The peak presenting at 5.2 – 5.9 ppm is identified as the protons on the TrFE (-CF*H*-CF_2-) unit. The broad peaks observed beyond 6 ppm are assigned to the protons on the double bonds (-CF_2-CF=C*H*- CF_2-). These peaks are not observed on the ^{1}H NMR of the pristine P(VDF-TrFE-CFE) terpolymer.

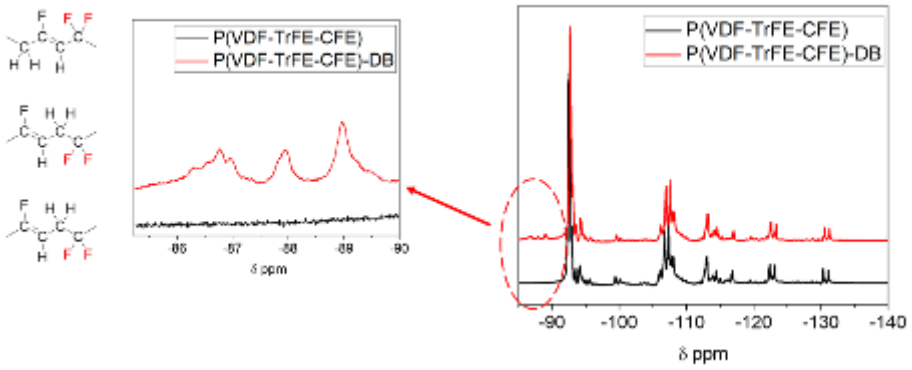

Figure 3-4. ^{19}F NMR spectra of P(VDF-TrFE-CFE) and P(VDF-TrFE-CFE)-DB. Left: ^{19}F NMR spectra between -85 ppm and -90 ppm to show the ^{19}F signals close to the double bonds. Right: ^{19}F NMR spectra between -80 ppm and -140 ppm

To further confirm the formation of double bond, ^{19}F NMR spectra of the original P(VDF-TrFE-CFE) and P(VDF-TrFE-CFE)-DB were studied (Figure 3-4). The structure consists mainly of VDF-VDF head-tail (-CH_2-C*F*$_2$-CH_2- C*F*$_2$-) sequence appearing around -92.5 ppm. The new peaks around -88 ppm in P(VDF-TrFE-CFE)-DB indicates the presence of the F atoms next to the double bond (-CF2CH=C*F*-CF2-) units.

3.3.2 Fourier transform infrared (FTIR) spectroscopy

Fourier transform infrared (FTIR) spectroscopy was also conducted to confirm the formation of the double bonds (Figure 3-5). The characteristic peaks around 1720 cm^{-1} are assigned to the -CF=CH- stretching(*72*).

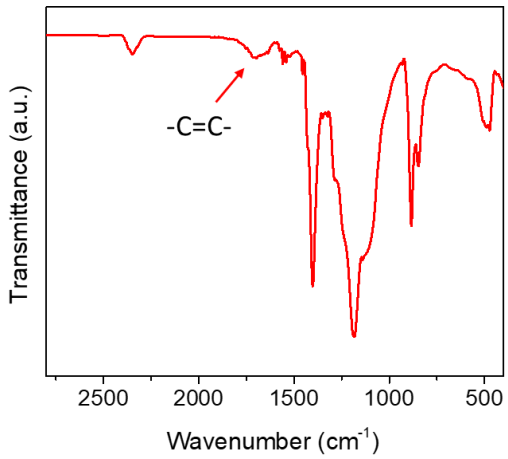

Figure 3-5. Fourier transform infrared (FTIR) spectroscopy of DB-P(VDF-TrFE-CFE)

3.3.3 Crosslinking characterization

The P(VDF-TrFE-CFE)-DB was co-dissolved with benzoyl peroxide, a free radical crosslinking initiator, and the solution was used to cast thin films. Exposure to high temperature (120 ^oC) crosslinked the C=C double bond. Figure 3-6 shows the pictures of the resulting c-P(VDF-TrFE-CFE) as well as the pristine P(VDF-TrFE-CFE) in a good solvent of the terpolymer (acetone). While the P(VDF-TrFE-CFE) dissolved gradually in

acetone, the crosslinked terpolymer could still retain its form in the solvent and restored to its original state after the solvent was evaporated, which is indicatively chemical crosslinking. The swelling ratio of the c-P(VDF-TrFE-CFE), which is defined as the volume ratio between the swollen polymer and unswollen polymer, was around 8. The network component ratio is called the "gel fraction". The gel fraction could be calculated as $f = \frac{m_1}{m_0} \times 100\%$, where m_1 and m_0 refer to the weight of the film remaining after being extracted with an good solvent (acetone), and of the original film respectively(*74*). For partially crosslinked polymer, a high gel fraction corresponds to a high crosslinking density. The measured gel fraction of the c-P(VDF-TrFE-CFE) was 93.3%, which indicates that the C=C double bond in P(VDF-TrFE-CFE)-DB could be crosslinked by the free radical initiator to form a network structure.

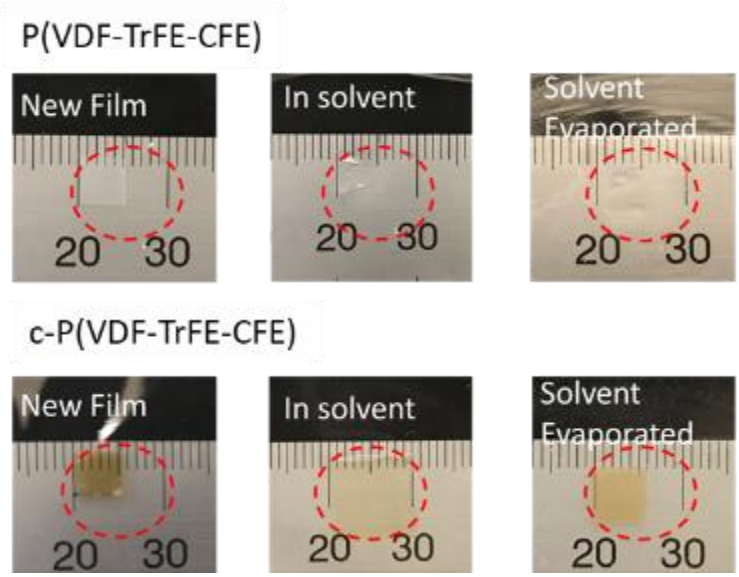

Figure 3-6. Solvent resistance test on pristine P(VDF-TrFE-CFE) and crosslinked PVDF-terpolymer films. The pristine P(VDF-TrFE-CFE) film dissolves in acetone. The crosslinked terpolymer film swells in acetone but reverts to its initial geometry once the solvent is removed. The test was conducted under room temperature (20 °C)

3.3.4 X-ray diffraction

To further understand the microstructure of the terpolymers, X-ray diffraction (XRD) spectra were measured and shown in Figure 3-7. The pristine terpolymer exhibits a single peak at 18.0° with the interchain lattice space of 4.96 Å (calculated from Bragg's equation, $2dsin\theta = n\lambda$) reflecting the terpolymer after annealing has a disordered 3/1 helical structure and TG/TG' conformation(*56*). For the crosslinked terpolymer, the broad peak between 17° to 20° can be deconvoluted into two peaks at 18.0 ° and 18.6 °, respectively. The 18.0° peak corresponds to a nearly identical interchain lattice space as in the pristine terpolymer (4.96 Å). The latter (18.6°, 4.8 Å) indicates the reflection in the ferroelectric crystalline phase(*75*).

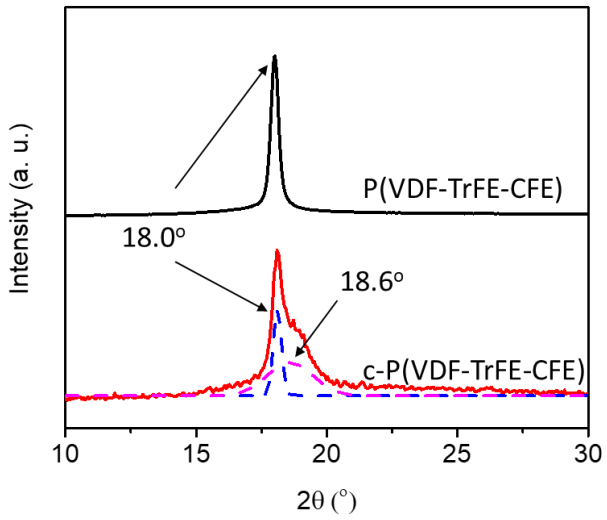

Figure 3-7. XRD of crosslinked and pristine PVDF terpolymer.

The crystallite size or coherence lengths (L) perpendicular to the crystallographic plane of the terpolymer corresponds to the size of polar or nonpolar domains. Scherrer's equation is a good method to estimate the crystallite sizes (L) of the terpolymer. $L = 0.9\lambda/(Bcos\theta)$, where λ is the wavelength of the x-ray, B is the full width at half the

maximum of the peak (FWHM), and θ is the Bragg's angle. The c-P(VDF-TrFE-CFE) has a wider peak at the half-maximum (0.380^{o}) than the pristine terpolymer (0.359^{o}) at 18.0^{o}. This reveals a decreased coherence length and crystallite size of the crosslinked terpolymer (22.3 nm vs 23.5 nm).

3.3.5 Differential scanning calorimetry

Figure 3-9 shows the DSC of both crosslinked and pristine P(VDF-TrFE-CFE) terpolymer. The melting point of P(VDF-TrFE-CFE) is 135 ^{o}C. In the crosslinked polymer, it is decreased to around 129 ^{o}C, which may be attributed to smaller crystal size as crosslinking usually introduces the defects along the polymer chains and limits the mobility of chain segments to assemble into larger crystals(*73*). The melting enthalpy of the crosslinked terpolymer is 16.6 J/g, which is slightly lower than 20.4 J/g for the pristine terpolymer. This can be explained by the decreased percentage crystallinity degree of the crosslinked terpolymer. The Curie temperature of a ferroelectric material is defined as the point where ferroelectric to paraelectric phase transition happens. In the pristine PVDF terpolymer, the Curie transition is a broad peak ranging from around -10 ^{o}C to 50 ^{o}C. In the crosslinked terpolymer the curie temperature peaks at 53.5 ^{o}C and the enthalpy involved in the transition (7.28 J/g) is larger than that observed for the pristine terpolymer (5.16 J/g). Both the XRD and DSC results strongly suggest that crosslinking leads to the reduced percentage crystallinity, smaller nanocrystallites, but larger switchable polarization.

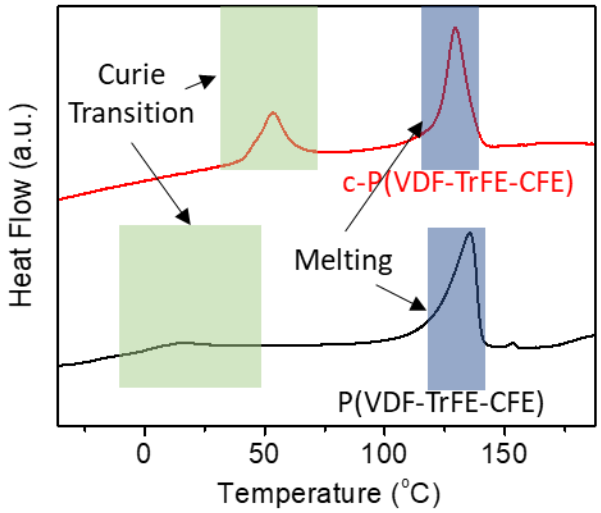

Figure 3-8. DSC of P(VDF-TrFE-CFE) and c-P(VDF-TrFE-CFE), the Curie transition and melting process are marked with green and blue respectively

3.3.6 Enhanced mechanical property

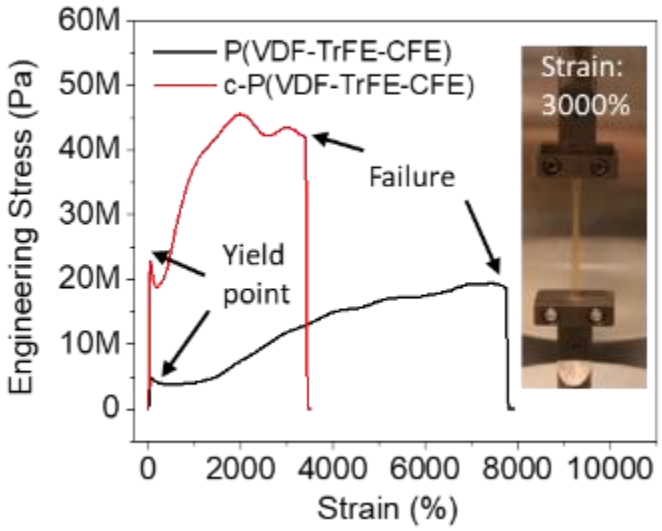

Figure 3-9. The stress-strain curve for P(VDF-TrFE-CFE) and c-P(VDF-TrFE-CFE). strain rate: 0.5 s^{-1}, displacement speed: 0.5 mm/s, test temperature: 20 °C, film thickness: ~ 30 μm, in-set picture: c-P(VDF-TrFE-CFE) at 3000% strain

The mechanical properties of the crosslinked terpolymer were investigated and the stress-strain curves of the pristine and crosslinked terpolymer are presented in Figure 3-9. The test was conducted under room temperature (20 ^{o}C) and the strain rate was kept constant at 0.5 s^{-1}. Like other semi-crystalline polymers, the stress-strain curves contain the stages of elastic deformation, plastic deformation with typical necking process, strengthening caused by the formation of the fibrillar structure at high strains, and final failure(*76*). The formation of crosslinking network limits the lamellae slipping and chain pulling-out from the lamellae(*77*). The elongation at break decreases accordingly with the formation of crosslinking network. Both the yield and tensile strength of the crosslinked terpolymer are improved. The yield strength of c-P(VDF-TrFE-CFE) increases significantly to 22.90 MPa, comparing to that of the pristine terpolymer (4.84 MPa). The tensile strength of the pristine terpolymer is 19.3 MPa, which is lower than that of crosslinked terpolymer (45.6 MPa).

DMA is an effective technique to study materials' mechanical properties and identify phase transitions across broad temperature ranges. Figure 3-10 presents the storage moduli (E') and the loss factors ($\tan\delta$) of the pristine and crosslinked terpolymers. As a result of forming a crosslinked network, the storage modulus of c-P(VDF-TrFE-CFE) at room temperature (20 ^{o}C) is increased 3 times compared to the uncrosslinked sample. The storage moduli of the pristine and crosslinked terpolymers both decrease with increasing temperature. The melting point and the curie temperature identified via the DMA method match well with the DSC analysis. The pristine terpolymer melts around 130 ^{o}C indicated by the precipitous decline of the storage modulus and rapid increase of the loss factor. The

crosslinked terpolymer exhibits rubbery elasticity 140 °C and 250 °C with small loss factor above the T_m. The storage modulus of the c-P(VDF-TrFE-CFE) is almost constant around 2 MPa in this region(*78*). Figure 3-10 (c) presents an elasticity test of the c-P(VDF-TrFE-CFE) film (thickness ~ 50 μm, length ~ 10 mm, width ~ 5 mm) at 170 °C. The thin film was stretch up to 100% strain and it restored to its original length quickly (< 1 s) once the external force was removed.

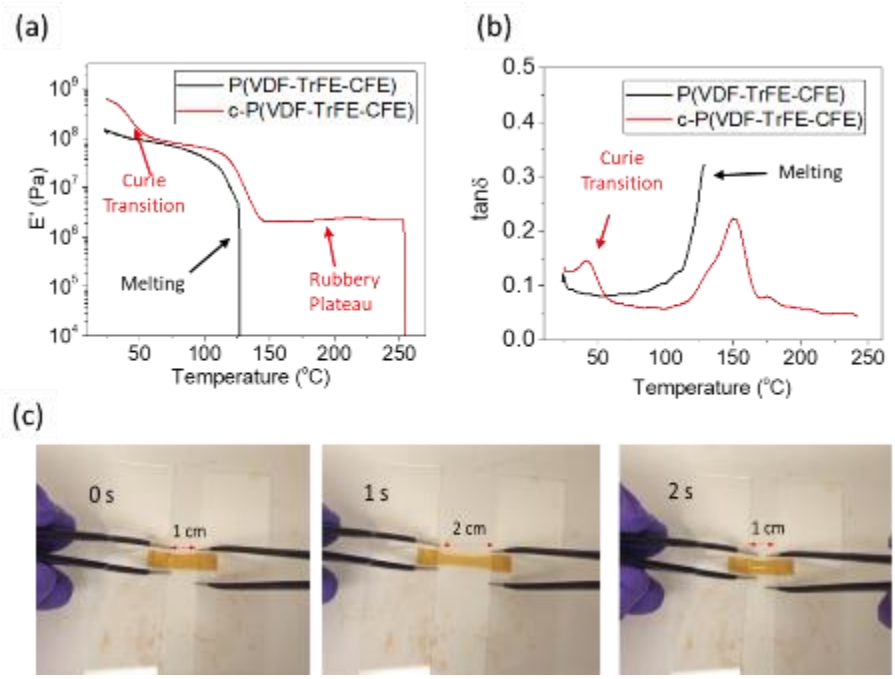

Figure 3-10. (a) Storage modulus as functions of temperature for P(VDF-TrFE-CFE) and c-P(VDF-TrFE-CFE), test frequency: 1 Hz. (b) Loss factors as functions of temperature for P(VDF-TrFE-CFE) and c-P(VDF-TrFE-CFE), test frequency: 1 Hz. (c) Elasticity test of the crosslinked terpolymer at 170 °C

3.3.7 Dielectric constant of crosslinked PVDF terpolymer

To examine the influence of crosslinking on the dielectric properties of the P(VDF-TrFE-CFE) terpolymer, dielectric constant, and dielectric loss were measured as functions of frequency at room temperature.

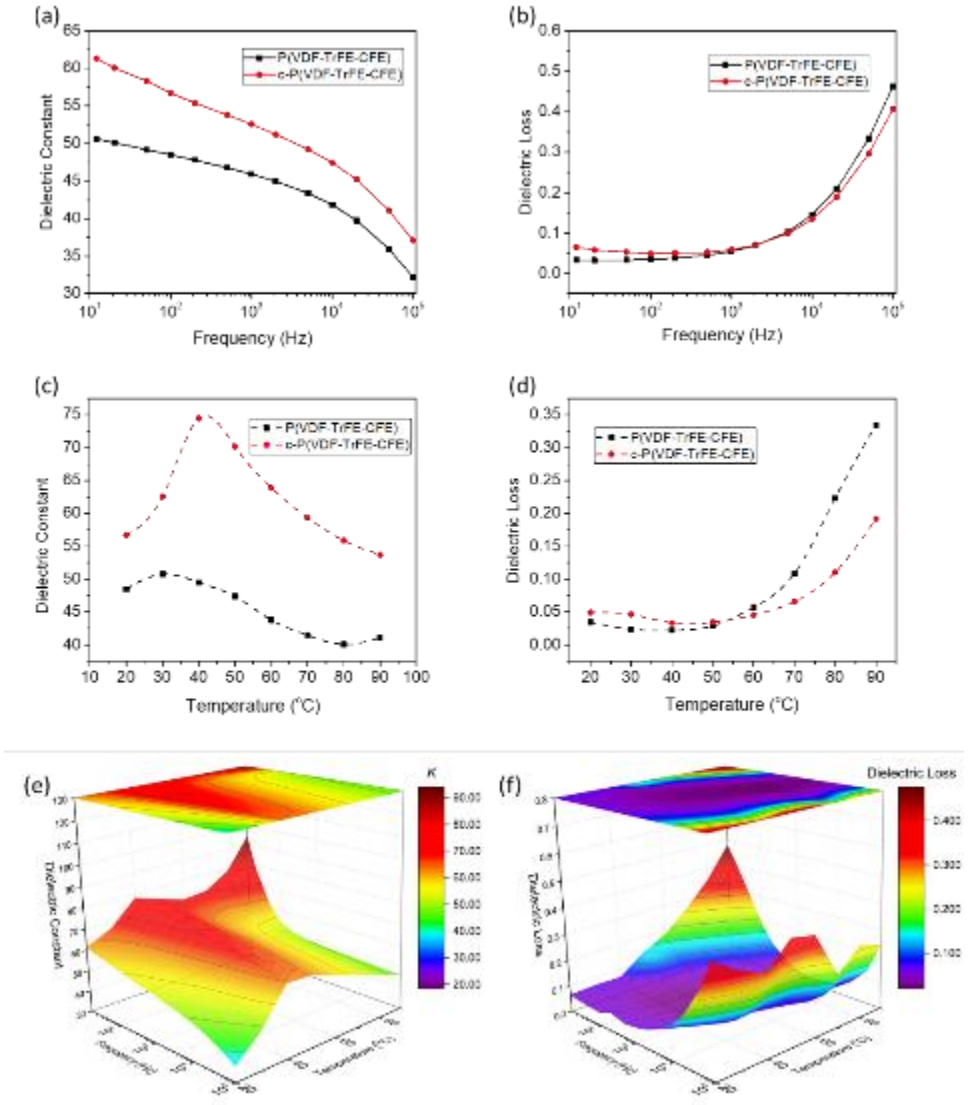

Figure 3-11. (a) Dielectric constant and (b) loss as functions of frequency for P(VDF-TrFE-CFE) and c-P(VDF-TrFE-CFE) at room temperature (20 °C). (c) Dielectric constant and (d) loss as functions of temperature for P(VDF-TrFE-CFE) and c-P(VDF-TrFE-CFE) at 100 Hz.

As shown in Figure 3-11 (a), c-P(VDF-TrFE-CFE) demonstrates an increased dielectric constant as compared to the pristine PVDF terpolymer, between 10 Hz and 100 kHz. At 1 kHz, the c-P(VDF-TrFE-CFE) has a dielectric constant of 53, which is about 15% higher than that of the P(VDF-TrFE-CFE). The dielectric loss of the crosslinked terpolymer is slightly higher than that of the uncrosslinked one in the low-frequency range (< 1 kHz) but lower in the high-frequency range (> 1 kHz). Previous studies(*79*) and the DSC and XRD results above reveal that crosslinking leads to smaller nanocrystallites and thus larger switchable dipoles. The enhanced dielectric constant of the c-P(VDF-TrFE-CFE) may also be attributed in part to the increased amorphous-crystalline interface area(*65*, *73*, *80*). Figure 3-11 (c) and (d) shows the temperature dependences of the dielectric constant and the dielectric loss at 100 Hz. The dielectric constant spectra of P(VDF-TrFE-CFE) and c-P(VDF-TrFE-CFE) both have a broad dispersive peak slightly higher than room temperature, which is a typical characteristic of relaxor ferroelectric materials[24]. The dielectric constant of c-P(VDF-TrFE-CFE) peaks at 75 at 40 ^{o}C, which is about 50% higher than the peak value of the uncrosslinked terpolymer at 30 ^{o}C. Figure 3-11 (e) and (f) present the 3D graphs of the dielectric constant and the dielectric loss of the crosslinked terpolymer as functions of temperature and frequency. The dielectric constant of the crosslinked peaks around 40 ^{o}C (from 10 Hz to 100 kHz) and 90 ^{o}C (<100 Hz). For the dielectric constant peak near the Curie temperature, the rotational motions of the dipolar groups contribute to the high dielectric constant (78 at 10 Hz and 40 ^{o}C)(*81*, *82*). As the frequency increases, these rotational motions of the dipolar cannot keep up with the electric field. The dielectric constant of both the pristine and the crosslinked terpolymers decrease as the frequency increases due to the slow relaxation (> 10 us) of the microcrystals in the terpolymers(*73*),

which corresponds the jump of dielectric loss around 10 - 100 kHz. The high-temperature peak corresponds to the annealing process in the crystalline regions(*81*, *83*). When the temperature is close to the melting point (129 ^{o}C), the polymer chains are flexible, and the dipolar units can move smoothly. It leads to a high dielectric constant (~93 at 10 Hz and 90 ^{o}C) and sizable dielectric loss (~0.47 at 10 Hz and 90 ^{o}C).

3.3.8 Hysteresis loops

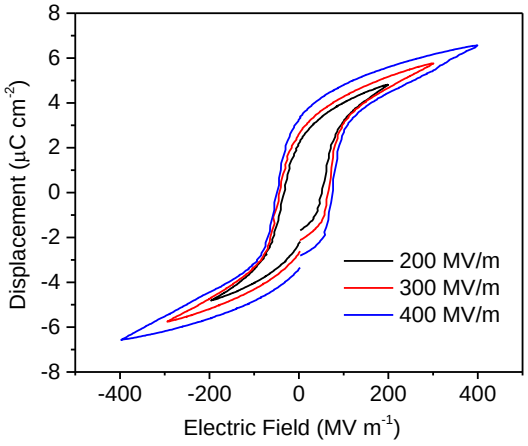

Figure 3-12. Dipolar displacement electric field loops for crosslinked PVDF terpolymer at different electric fields at room temperature (20 ^{o}C), test frequency = 10 Hz.

The ferroelectric properties of the crosslinked PVDF terpolymer was studied with the displacement-electric field hysteresis measurement. Figure 3-12 shows shows the hysteresis loops at different electric fields; the crosslinked film can operate at an electric field up to 400 MV/m. At 400 MV/m, the displacement reaches 6.8 $\mu C/cm^2$. Compared to the pristine PVDF terpolymer (Figure 3-13), the crosslinked terpolymer shows a decreased displacement under the same external electric field.

Figure 3-14 shows the D-E hysteresis loops of the crosslinked PVDF terpolymer at different temperatures. The hysteresis loop becomes narrower with increasing temperature from 20 ^{o}C to 40 and 60 ^{o}C, and this feature corresponds to the shifted curie temperature

(53.5 ^{o}C) revealed in the DSC data. When the temperature increases, the polymer goes through the ferroelectric-paraelectric transition.(*84*)

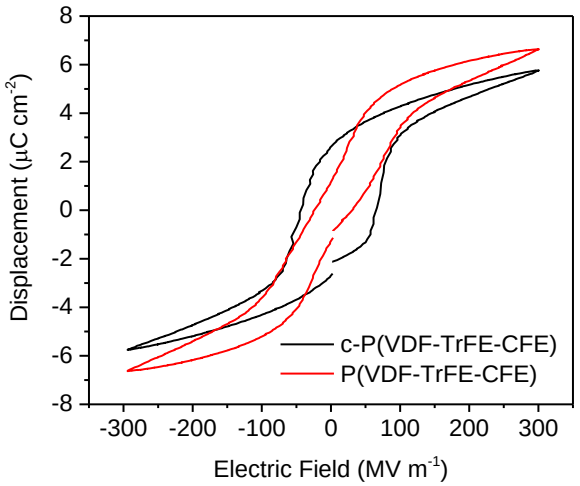

Figure 3-13. Hysteresis loops of c-P(VDF-TrFE-CFE) and P(VDF-TrFE-CFE), tested frequency = 10 Hz.

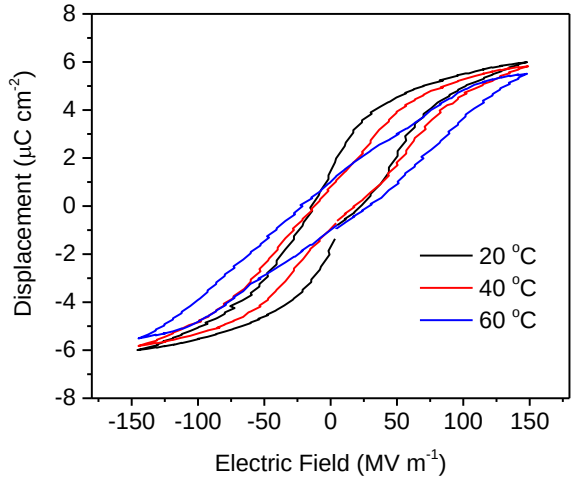

Figure 3-14. Hysteresis loops of crosslinked PVDF terpolymer at different temperatures, test frequency = 10 Hz

3.3.9 Breakdown strength

For the estimation of the electric reliability of the polymer films under high voltage, two-parameter Weibull statistic may be used to calculate the breakdown strength. The cumulative probability of electric breakdown at the tested field $P(E) = 1 - exp\left[-\left(\frac{E}{E_b}\right)^{\beta}\right]$, where E_b is the scale data characterizing the breakdown field strength of the tested material. High E_b represents good electrical stability. And β is the slope that evaluates the measured data. The larger β is, the narrower the distribution of the breakdown points is. Figure 3-15 shows the experimentally measured values. The E_b of the crosslinked terpolymer is 445 MV/m, higher than the 325 MV/m for the pristine terpolymer. Because the breakdown possibility follows exponential rule, a high breakdown field strength means a significant decrease of breakdown possibility under the same electric field.

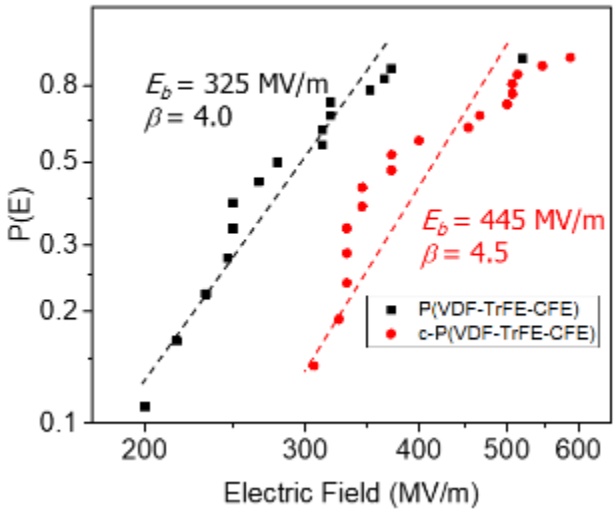

Figure 3-15. Weibull distribution of breakdown strength of P(VDF-TrFE-CFE) and crosslinked P(VDF-TrFE-CFE).

There are several common causes of electrical breakdown, including thermal breakdown, electromechanical breakdown, and breakdown caused by space charge. The

crosslinked terpolymer is stiffer, which may be the main contributing factor for higher electromechanical strength and thus the observed greater breakdown field strength.

3.3.10 Energy density

The combination of high dielectric constant and high breakdown field of the crosslinked terpolymer make it a good candidate for dielectric energy storage applications. Figure 3-16 represents the energy density of the crosslinked and pristine PVDF terpolymer calculated using $U_d = \int E\, dD$. At the same external field, the crosslinked terpolymer exhibits lower energy density due to the decreased measured displacement. However, the enhanced breakdown field strength enables the crosslinked PVDF terpolymer to stay operable at electric field up to 445 MV/m (E_b). The maximum energy density calculated is 15.2 J/cc, which is higher than the maximum energy density of 11.3 J/cc for the pristine terpolymer.

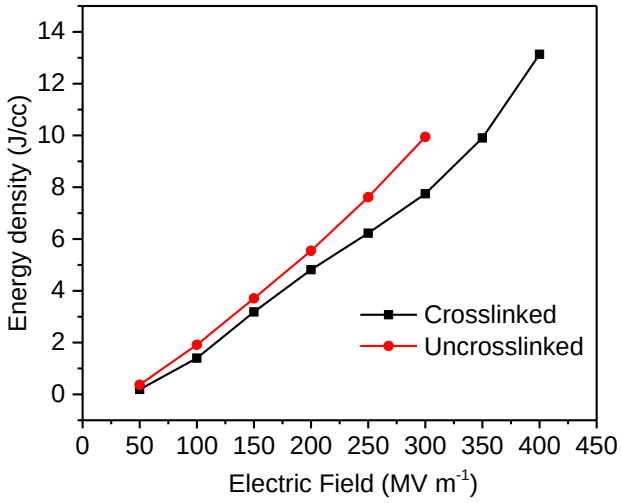

Figure 3-16. Energy density of crosslinked and pristine PVDF terpolymer at room temperature

3.4 Conclusion

In summary, a chemically crosslinked P(VDF-TrFE-CFE) terpolymer has been synthesized. Dehydrochlorination of pristine P(VDF-TrFE-CFE) can be obtained by treatment using triethylamine. The reaction introduces C=C double bonds onto the polymer chain which are further crosslinked using a typical free radical initiator. The crosslinked polymer exhibits improved performance in several metrics important to the applications of P(VDF-TrFE-CFE), including anti-solvent property, enhanced dielectric constant and mechanical strength. The yield strength of c-P(VDF-TrFE-CFE) is 22.90 MPa, and its tensile stress is 45.56 MPa. Unlike the pristine terpolymer which melts around 130 ^{o}C, the crosslinked terpolymer can survive up to 250 ^{o}C; it behaves like an elastomer above the T_m. Weibull analysis reveals an improved electrical reliability of the crosslinked terpolymer. The E_b of the crosslinked terpolymer is 445 MV/m, higher than the 325 MV/m for the pristine terpolymer. Further investigation is ongoing to examine the potential application of c-P(VDF-TrFE-CFE) for capacitive energy storage and electromechanical actuation.

4 Electrocaloric cooling device

4.1 Introduction

Vapor-compression refrigeration systems, commonly used in air-conditioners for buildings and automobiles, refrigerators for food storage, and processing plants, rely on the phase change of refrigerants driven by mechanical compressors, a technology developed over two centuries ago. While effective for many applications, vapor-compression systems have their disadvantages. They are bulky, complex, and difficult to scale down to meet the cooling demands of modern technologies, such as mobile devices, wearable electronics, and flexible electronics. The coefficient of performance (COP), the amount of heat removed per electrical energy consumed, is also low, typically 2-4 for vapor compression refrigerators(*85*). Existing refrigerants also have high global warming potentials and present an environmental risk upon leaking or improper disposal(*9*).

Solid-state cooling systems are more recent alternatives that do away with the need for compressors and refrigerants. Thermoelectric coolers based on the Peltier effect produced in bismuth antimony telluride have found several applications. However, these systems typically exhibit a COP even lower than that of vapor-compression refrigeration systems. Further, the ceramic materials tend to be expensive, restricting their use to small-scale applications. Solid-state refrigeration based on the electrocaloric (EC) effect has been proposed as a more efficient alternative that can also be used to realize compact low-profile devices(*86*). The EC effect is a thermodynamic phenomenon where a reversible

temperature change of dielectric material is achieved by the modulation of its dipolar entropy under an applied electric field(*3*, *4*, *47*).

Current EC materials such as relaxor ferroelectric ceramics and polymers have shown promising material properties(*3*, *4*). Lead zirconium titanate ($PbZr_{0.95}Ti_{0.05}O_3$) exhibits a large adiabatic temperature change (ΔT) of 12 ˚C at 226 ˚C with an associated theoretical maximum heat removal of 4 J/g. Various poly(vinylidenefluoride) (PVDF) - based ferroelectric polymers have been investigated with increasing interest due to their large isothermal entropy change, lightweight, and adaptability to complex form factors and low-temperature processing conditions. Among this class of polymers, poly(vinylidenefluoride-ter-trifluoroethylene-ter-chlorofluoroethylene) (P(VDF-TrFE-CFE)) has been reported with a calculated ΔT of 12℃ at 55 ℃ corresponding to a maximum heat removal density of 18.4 J/g(*4*). Nanocomposites comprised of either P(VDF-TrFE-CFE) or (P(VDF-TrFE)) with nanosized Boron Nitride or other ceramics have also been reported with similarly high EC performance(*47*).

Even though numerous publications have reported materials with high EC performance, the realization of practical solid-state cooling devices based on the EC effect remains a major challenge. Among the reported EC cooling devices, there is no experimentally obtained COP data(*36*). The highest reported specific cooling power of 0.018 W/g is still orders of magnitude smaller than the theoretically calculated values based on intrinsic material properties(*87*). One practical challenge of implementing EC cooling devices stems from the fact that electrocaloric materials need to be physically transported between a heat sink and the heat source in sync with the application and removal of electric

fields. An electric motor and transmission may be used, but such a design lowers the COP and increases the size and overall complexity of the system.

4.2 Experimental section

4.2.1 Fabrication of the EC polymer stack

The terpolymer of P(VDF-TrFE-CFE) (63.2/29.7/7.1 mol%, Piezotech Arkema group) was dissolved at 8 wt % in 2-Butanone (Spectrum Chemical) by sonication for 2 h. Then the solution was filtered using a PTFE filter with a pore size of 0.2 μm and degassed using a bath-sonicator. P(VDF-TrFE-CFE) films were prepared by casting the solution on glass substrates, drying at room temperature overnight, and curing at 90 ˚C for 2 h. The thickness of the films is 30 μm. CNT solution was spray-coated onto the EC polymer films using a predefined mask (2 × 7.5 cm^2) to form uniform CNT electrodes with a sheet resistance of 6.5 kΩ/□. Two EC polymer films were peeled off their glass substrates and then attached with an overlapping region of 2 x 5 cm^2 using a laminator (SircleLam 336-6R). The EC polymer films were laminated with one CNT electrode sandwiched between the EC polymer films and the other CNT electrode residing on top of the EC polymer stack. A third CNT electrode was spray-coated on the bottom side of the EC polymer stack using the mask. Finally, the laminated EC polymer stack with three CNTs electrodes was annealed at 120 ˚C for 16 h in a vacuum oven to remove the residual solvent further and increase the crystallinity of the P(VDF-TrFE-CFE) polymer films. The crystallinity and crystal size increased after annealing at 120 °C for 16 h which further increased ΔT, based on X-ray diffraction of the P(VDF–TrFE–CFE) films.

4.2.2 Preparation of carbon nanotubes solution

P3-SWNTs (6 mg), purchased from Carbon Solution, Inc., were dispersed in a mixture of isopropyl alcohol (18 ml, IPA) and deionized water (2 ml, DI water) using a bath sonicator (VWR B9500A-DTH) for 2 h. The solution was then centrifuged at 8500 rpm for 15 min, and the supernatant was used as the carbon nanotube solution.

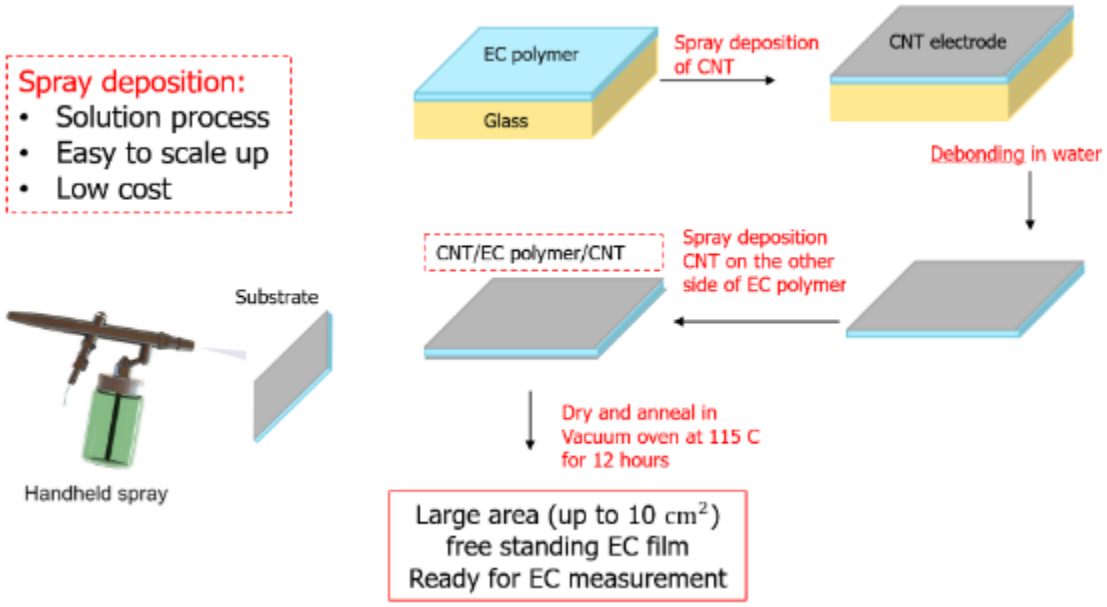

Figure 4-1. Spray coating CNT electrode onto EC polymer

4.2.3 Adiabatic temperature measurement

IR camera has been widely used in magnetocaloric and elastocaloric studies(*8*) and seems to be a good technique for the EC characterization thanks to its non-contact nature and high spatial resolution. In this work, an IR camera (ICI, 9320-C) with a frame rate of 10 Hz was used for the real-time temperature measurement of P(VDF-TrFE-CFE) thin film. The experiment set-up is, as shown in Figure 4-2 and Figure 4-3. Metal electrodes like evaporated aluminum are reflective in IR range and are not suitable for accurate temperature measurement. Single-walled Carbon Nanotubes (CNTs) electrode was sprayed on both sides of the film as electrode and the active area was a 6 mm-diameter

circular with overlapping electrodes. The free-standing EC thin film was hold by laser-cut PET frame with adhesive. The IR camera was focused on the plane of the EC sample. Electric fields from 17 to 86 MV/m (square wave, 0.1 Hz) were applied across the EC film and the EC temperature change was instantaneous (< 0.1 s) as the electric field switching between on and off. Figure 4-5 represents the EC temperature change as a function of applied electric field. The temperature change is 5.1K at 83.3 MV/m.

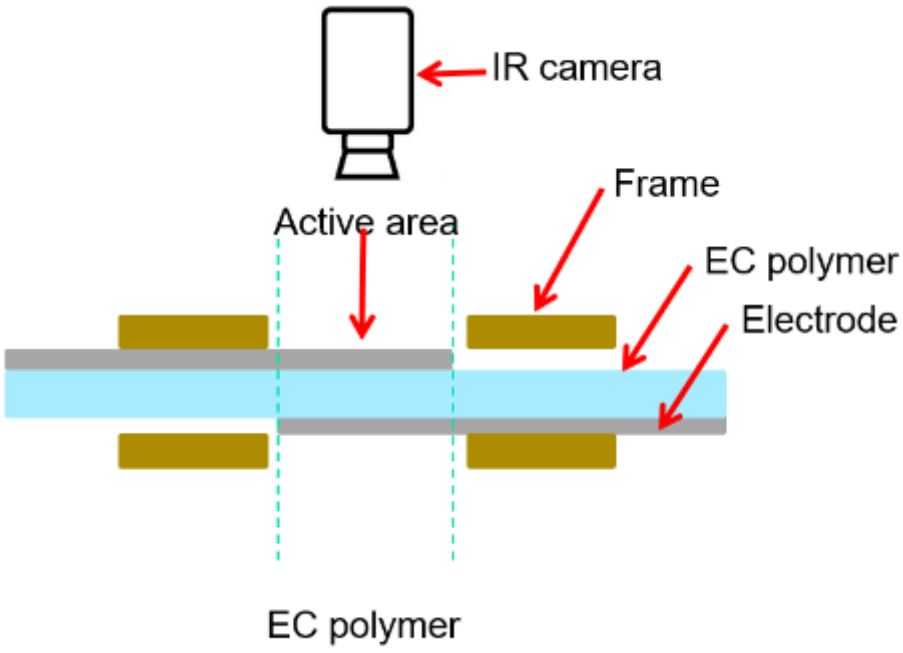

Figure 4-2. Temperature change measurement set-up.

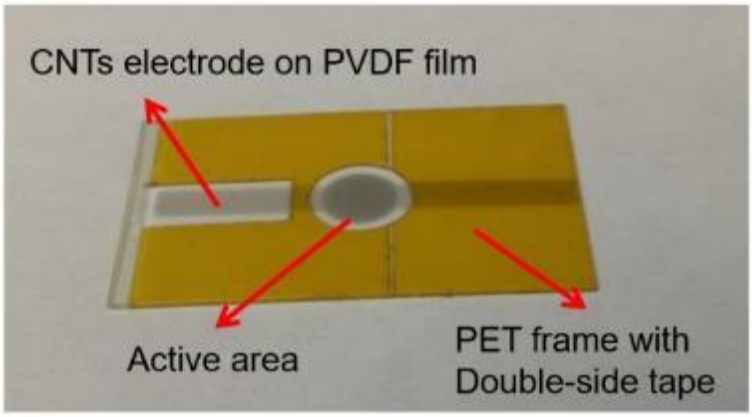

Figure 4-3. Illustration of PVDF film with CNTs electrode ready to measure.

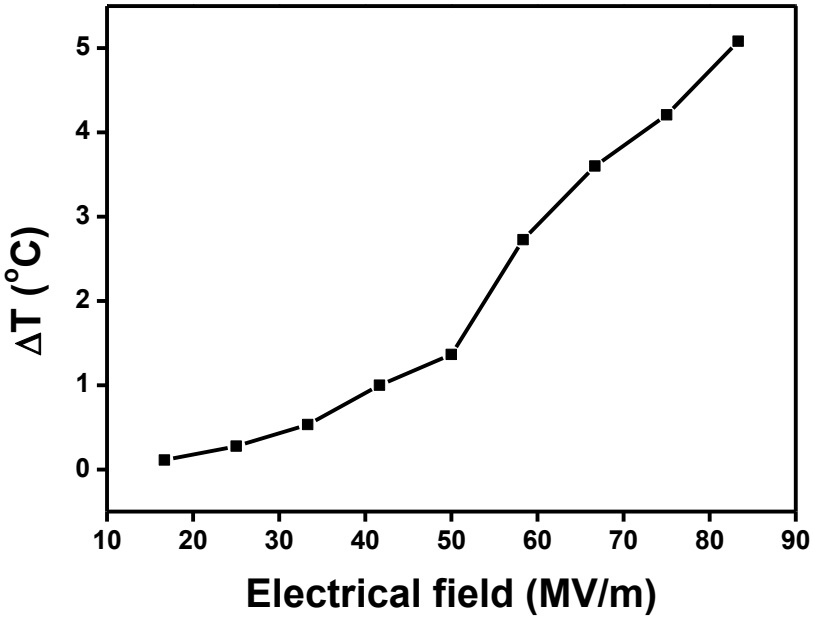

Figure 4-4. Adiabatic temperature change of an EC polymer stack as a function of applied electric filed.

4.3 Results and Discussion

4.3.1 Electrocaloric refrigeration device

Here, we report an EC refrigeration device architecture where electrostatic actuation is employed to rapidly transport a flexible EC polymer stack between a heat source and a heat sink. The electrostatic force not only moves the EC material but promotes the formation of intimate thermal contact between the EC polymer stack and the heat source/sink during each cycle. A compact solid-state cooling device measuring 7 cm × 3 cm × 0.5 cm has thus been realized, achieving a COP of 13 at a heat flux of 29.7 mW/cm^2. This heat flux corresponds to a specific cooling power of 2.8 W/g, which is the highest reported value of solid-state refrigeration to date. The previous record had a COP of only 1.9 and specific cooling power of 2 W/g(*88*). The thin-film EC cooling device is flexible and can conform to curvilinear surfaces. It also operates without the noise and complexity of a conventional cooling system.

The architecture of the EC cooling device is illustrated in Figure 4-5. P(VDF-TrFE-CFE) is selected as the active EC material due to its large entropy change, large ΔT near room temperature, and mechanical flexibility. Single-walled carbon nanotubes (CNTs) are used to form the electrodes of the EC film due to their mechanical compliance, thermal stability, and oxidation resistance. The P(VDF-TrFE-CFE) solution was drop-cast onto a glass substrate, and the resulting polymer film was annealed at 90 ˚C. A dispersion of CNTs in an isopropyl alcohol and water mixture was spray-coated onto the polymer film. One of the as-prepared films was laminated directly on top of another with only one CNT layer sandwiched between the EC films. The overlap of the CNT areas across the polymer

films defined the active area (2 × 5 cm^2) for the EC effect. The bottom surface of the stack was also spray-coated with CNTs to complete the fabrication of a two-layer EC polymer stack: CNT/P(VDF-TrFE-CFE)/CNT/P(VDF-TrFE-CFE)/CNT with a total thickness of 60 μm. The EC laminate was then placed in a vacuum oven at 120 ˚C for 16 h to remove the residual solvent and to raise the degree of crystallinity and thereby enhance the polarizability of the polymer(*89*).

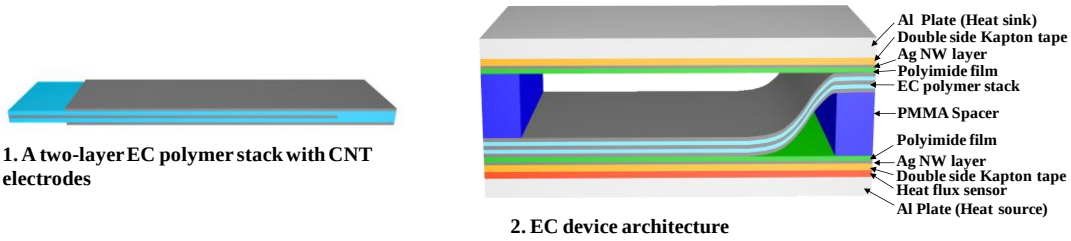

Figure 4-5. A solid-state EC cooling device. Schematic illustration of the EC polymer stack and solid state cooling device (not to scale).

The EC cooling device comprises two laminate sheets 7 cm × 3 cm in area separated by a 6 mm thick spacer made of Poly(methyl methacrylate). Each laminate sheet consists of a double-sided Kapton™ tape, a polyimide film, and a silver nanowire percolation network layer inserted in between. The nanowire percolation layer serves to act as one electrode of the electrostatic actuator. The EC polymer stack is mounted on one end between the left spacer and the lower laminate and the other end between the right spacer and the upper laminate as illustrated in Figure 4-5. For testing convenience, a 6.3 mm thick aluminum plate is attached to the outer sticky surface of each of the Kapton™ tape. The plate acts as the heat source and sink, respectively. A heat flux sensor is inserted between the aluminum plate heat source and the Kapton™ tape for *in-situ* thermal measurement.

First, thin copper wires were attached onto each CNTs electrode with carbon grease covered by scotch tape to form low resistance junctions between CNTs electrodes and copper wires. Second, the EC polymer stack was elastically bent into an S-shape and fixed onto a PMMA frame that functions as a 6 mm spacer. Third, a heat flux sensor (OMEGA HFS-4) was bonded to an aluminum plate (7.5 cm × 3.5 cm × 6.3 mm) using double-sided Kapton tape that was spray-coated with a thin silver nanowire layer (Zhejiang Kechuang Advanced Materials Co., Ltd). Fourth, a polyimide film with thickness of 15 μm was coated on the surface of the silver nanowire layer, forming a heat source structure of aluminum plate/ heat flux sensor/ Kapton tape/ silver nanowire layer/ polyimide. Fifth, a heat sink was fabricated similarly to the heat source but without the attachment of a heat flux sensor. Finally, the heat source and heat sink were attached onto the top and bottom sides of the PMMA frame to complete the fabrication of the P(VDF-TrFE-CFE) cooling device.

The EC polymer stack forms an S-shape in its cross-sectional view. The stationary ends of the S-shaped film allow the film to make good thermal contact with the electrodes of the top or bottom aluminum plate(*90*). During operation, the S-shaped EC film moves up and down like a flexure spring driven by electrostatic forces when a voltage is applied between one of the silver nanowire layers and the corresponding outer CNT layer on the EC stack facing the silver nanowire layer. Because of its lightweight and low bending stiffness, the EC stack could be shuttled rapidly between attachment to the upper and lower laminates with response time (less than 30 ms) and total energy consumption (of only ~ 0.02 W). This electrostatic actuation is compact, noiseless, and does not incur frictional

forces which could induce material damage and cause energy consumption and thus parasitic heating (see further description of the electrostatic actuation below).

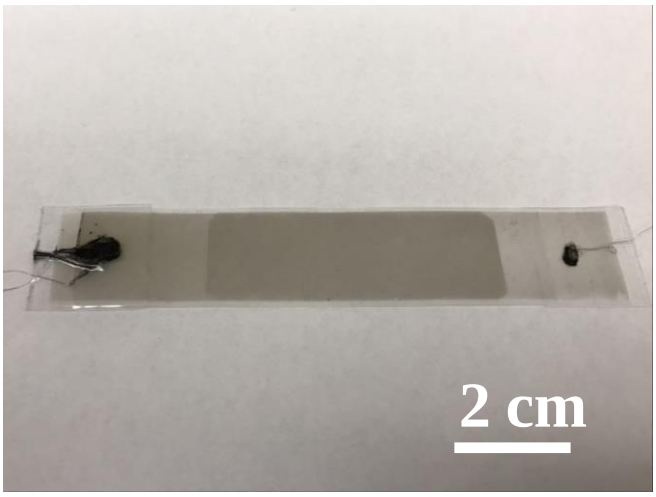

Figure 4-6. Photograph of a freestanding two-layer P(VDF-TrFE-CFE) stack with CNTs electrodes.

Figure 4-6 shows a photograph of a freestanding two-layer P(VDF-TrFE-CFE) stack with an active area of 2 × 5 cm^2 defined by 14 nm thick CNT electrodes on both sides. Infrared thermal images of the free-standing EC polymer stack film taken immediately after an electric field of 58.3 MV/m was applied (upper image) and removed (lower) at ambient conditions are shown in Figure 4-8.

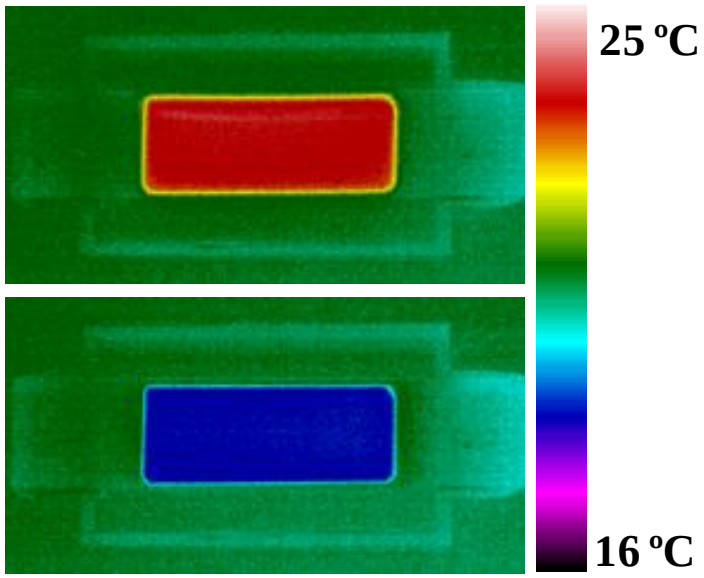

Figure 4-7. IR thermal images of P(VDF-TrFE-CFE) film following application and removal of a 58.3 MV/m electric field.

The instaneous (adiabatic) temperature increase of the EC film when an electric field is applied results from the dipole orientation in the relaxor ferroelectric polymer and consequent decrease of entropy in the system.

Figure 4-8 shows the side view of the EC polymer device when the EC polymer stack is electrostatically actuated to form thermal contact with the bottom and top aluminum plate surfaces, respectively. The actuation is achieved by applying an electrostatic field across the polyimide film of either the bottom or top plate to drive the movement of the EC polymer stack. The electrostatic force that acts to move the EC polymer stack is determined by the electric field across the air gap. The air gap is much smaller near the attachment point.

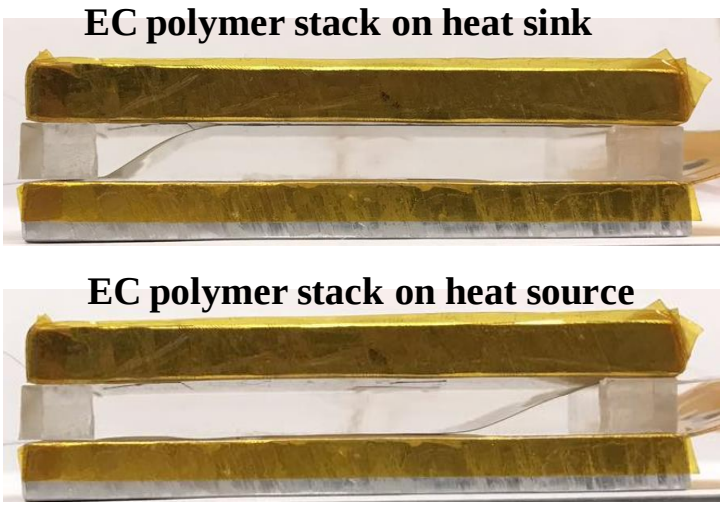

Figure 4-8. Photograph of side view of EC polymer stack on heat sink (top) and heat source (Bottom) by electrostatic force.

At this point, assuming that the thickness of the polyimide layer is much larger than its surface roughness, the pressure acting to move the film is

$$P_{contact} = \varepsilon_0 \varepsilon_r E_{contact}^2 = \frac{\varepsilon_0 \varepsilon_r V^2}{d_{polyimide}^2}$$

where E is the applied electrostatic field, ε_0 is vacuum permittivity, ε_r is the dielectric constant of polyimide. The ε_r of the polyimide used in this study is 4. Under an applied electrostatic field of 61 MV/m, this pressure is approximately 133 kPa, equivalent of 1.32 atmospheric pressure. Away from the attachment point, the pressure is dominated by the air gap. The air gap is largest at the point where the film attaches to the opposite electrode. The pressure at this point is

$$P_{gap} = \varepsilon_0 \varepsilon_r E_{gap}^2 = \frac{\varepsilon_0 \varepsilon_r V^2}{d_{gap}^2}$$

Since $d_{gap} >> d_{polyimide}$, this later pressure is much less. While P_{gap} may not be great enough to move the EC stack, the bending of the film allows for the film to progressively

attach a greater length to the active electrode (that to which the voltage is applied). In other words, the attachment point moves across the length of the film until all of the film, except for the small section needed to span the attachment point to the opposite electrode is move to the active electrode. This approach to electrostatic actuation has been used to move films for valve and the shape of the edge of the film gives his type of actuator the name "S-shaped film actuator" (e.g. Sato [1994]) and may be used when the bending stiffness of the film can be overcome by the electrostatic forces.

4.3.2 Operation mechanism

When an electric field is alternately applied across the top silver nanowire electrode and the top CNT layer of the EC stack and the bottom silver nanowire electrode and the bottom CNT layer of the EC stack, the EC polymer stack shuttles between the two aluminum plates. The electrostatic pressure on the film that is now in contact with the polyimide is roughly given by $P_{contact} = \varepsilon_0 \varepsilon_r E_{contact}^2 = \frac{\varepsilon_0 \varepsilon_r V^2}{d_{polyimide}^2}$. This pressure increases the thermal contact between the EC stack film and polyimide and thus facilitates the heat flux between the EC material and the aluminum plates. This is confirmed by the measured heat flux during the cooling cycle of an EC polymer stack when an electric field of 66.7 MV/m (square wave, 0.8 Hz, 50% duty cycle) was applied across the P(VDF-TrFE-CFE) films. As shown in Figure 4-9, as the electrostatic field is increased from 0 to 61 MV/m, the heat flux is increased from -8.3mW/cm2 to -29.7mW/cm2, a 258% enhancement in heat flux. To avoid issues with electrical breakdown, the electrostatic field was set to a maximum of 61 MV/m.

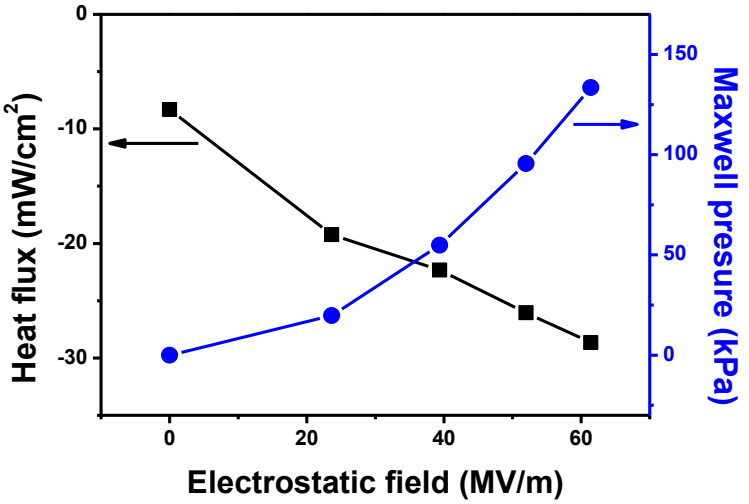

Figure 4-9. Heat flux and Maxwell pressure as a function of electrostatic field (negative heat flux indicates cooling).

Figure 4-10 shows the working mechanism of the present EC cooling device. One operating cycle consists of four main steps: 1) electrostatic actuation of the EC polymer stack towards the bottom aluminum plate (heat sink), 2) electrocaloric heating of the EC polymer stack, 3) electrostatic actuation of the EC polymer stack towards the top aluminum plate (heat source), and 4) electrocaloric cooling of the EC polymer stack. For simplicity of circuitry design, the EC cooling device is fabricated with a common cathode by connecting the two outer CNT electrodes of the EC polymer stack with a thin copper wire. The inner (middle) CNT electrode of the EC polymer stack serves as the anode to apply an electric field across the P(VDF-TrFE-CFE) film for electrocaloric heating. The silver nanowire films function as the anode to apply an electrostatic field across the polyimide for electrostatic actuation.

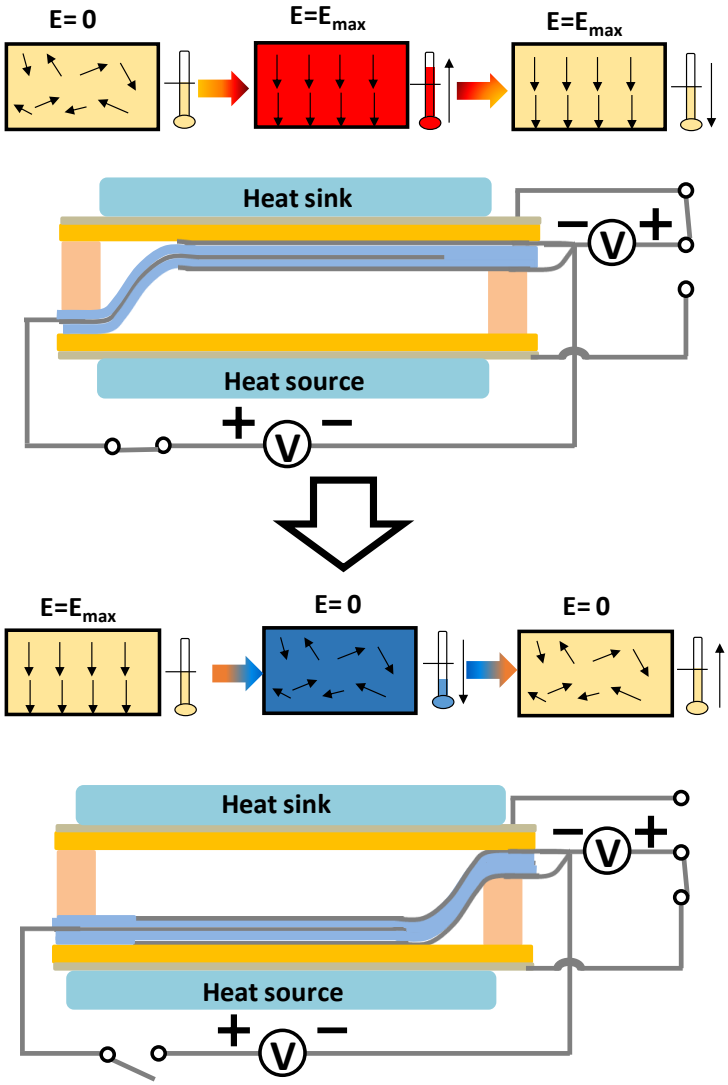

Figure 4-10. Schematic diagram of the working mechanism of the P(VDF-TrFE-CFE) cooling device. The electrostatic field drives the actuation of the EC polymer stack towards the heat sink or heat source, and the respective displacement of the EC polymer film during or heat source, and the respective displacement of the EC polymer film during operation of the device.

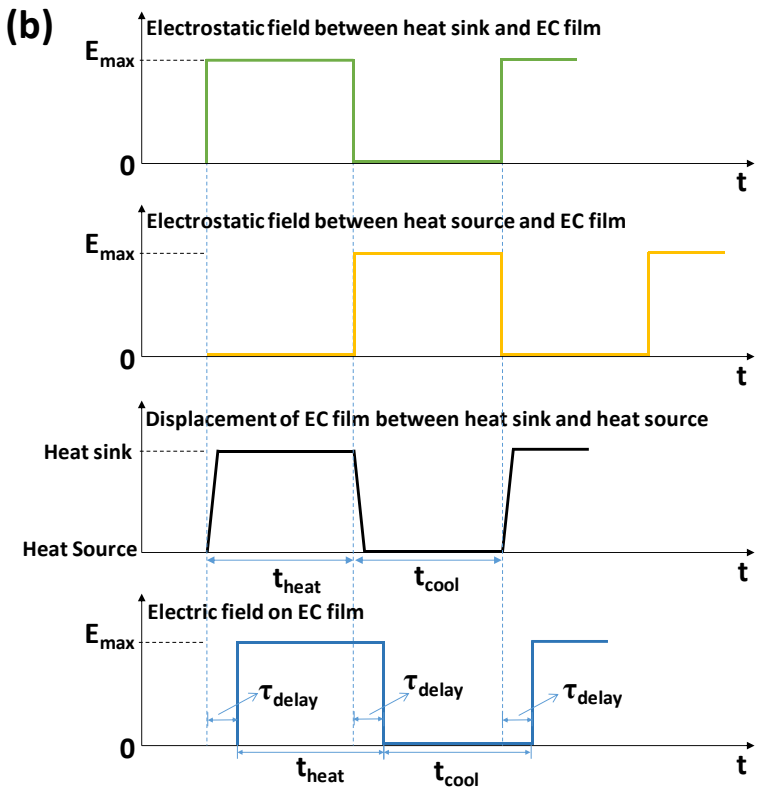

Figure 4-11. Time domain illustration of the cooling cycle.

Voltage switching for electrostatic actuation is controlled by an electric relay to switch between the silver nanowire anodes of the heat source and heat sink. During one cycle of heat transfer, an electrostatic field is first applied between the silver nanowire on the heat sink with the outer CNT electrodes to generate an electrostatic pressure to transport the EC polymer stack towards the heat sink. The time required to move the EC polymer stack from the heat source to the heat sink is roughly 0.03s, but a short delay (τ_{delay} = 0.15 s) is preprogrammed in the EC wave form to allow for the EC polymer stack to form sufficient thermal contact with the polyimide before applying an electric field across the P(VDF-TrFE-CFE) film. When an electric field is applied across the P(VDF-TrFE-CFE) film for electrocaloric heating, and the molecular dipoles becomes orderly aligned, the resulting decrease in entropy increases the temperature of the EC polymer film. A

temperature gradient is thus created causing heat to be transferred from the EC polymer stack to the heat sink. After a predefined time of heating, t_{heat}, the electrostatic actuation is switched using the electric relay to transport the EC polymer film towards the heat source. After another a short delay, τ_{delay}, electrocaloric cooling occurs by switching off the electric field across the P(VDF-TrFE-CFE) film to allow for the dipoles within the polymer to become randomly aligned. The entropy of the film increases while heat is transferred from the heat source to the EC polymer stack during a predefined time of cooling, t_{cool}, thus completing one cycle of heat transfer.

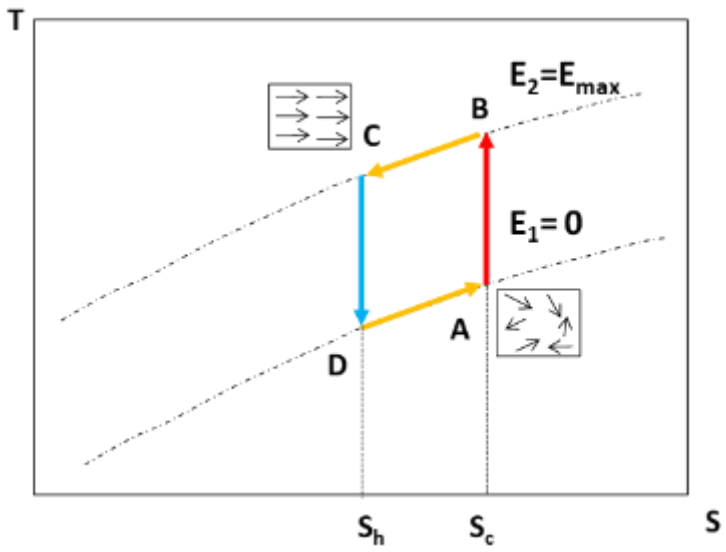

Figure 4-12. Thermodynamic refrigeration cycle driven by the electrocaloric effect.

Figure 4-12 shows one possible thermodynamic refrigeration cycle based on the electrocaloric effect. At point A, no electrical field is applied (E = 0), and the dipoles within the electrocaloric material (ECM) are oriented randomly. When an external electric field is applied (A→ B), the dipoles in the ECM start to align along the electric field. The temperature of the ECM increases rapidly, while the entropy is approximately constant due to the short time for heat exchange (ΔQ = 0). This step is similar to the compression step

in a conventional vapor compression refrigeration cycle. In the next step (B→C), the electric field is kept constant, and there is finite heat transfer from the ECM to the environment, causing the temperature and entropy of the ECM to decrease. During step C→D, the external electric field is removed, and the dipoles return to a state of disorder. Like A→B, C→D is also approximated as adiabatic due to short time available for heat transfer. The entropy is unchanged whereas the temperature rapidly decreases. At point D, the ECM reaches its lowest temperature. In step D→A, the ECM absorbs heat from the load, and the temperature and entropy of the ECM are increased. Finally, the system returns to its original state, A.

4.3.3 Power consumption measurement

The power consumption of the P(VDF-TrFE-CFE) cooling device was further investigated. Details of the circuitry and calculation to measure power consumption are shown in Figure 4-13. The electric energy consumption of the EC device in an EC cycle can be calculated using

$$W_{EC} = \int_{t1}^{t2} V_{EC} \times I_{EC} dt$$

where W_{EC} is the electrical work done in one EC cycle, V_{EC} and I_{EC} are the measured operating voltage and current, respectively.

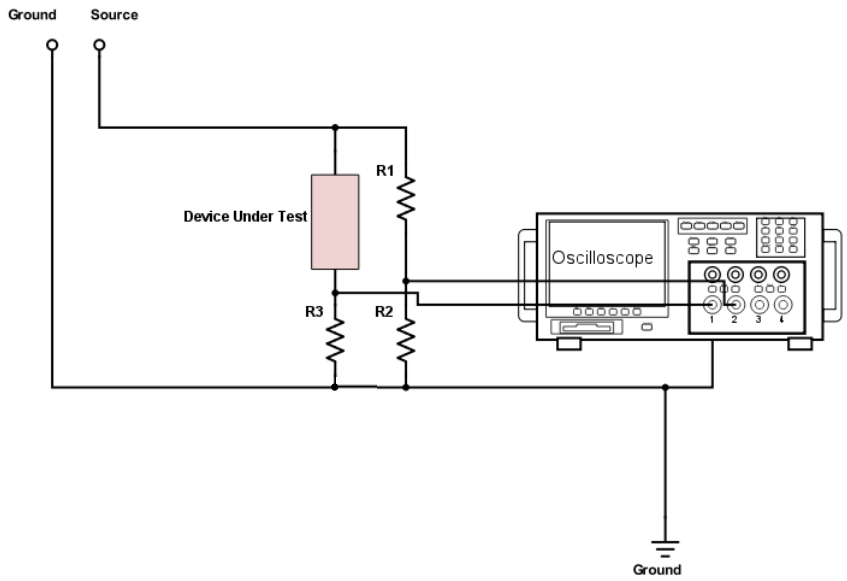

Figure 4-13. The voltage divider circuitry used to measure electric current and voltage for calculation of electrostatic power consumption.

In order to calculate the power consumption, it was necessary to measure both the applied voltage and the electric current through the EC polymer stack. The voltage divider circuitry used to measure the current and voltage is shown in Figure 4-14. A computer-connected oscilloscope is used to record the current and voltage of the Device Under Test (DUT). Channel 1 and Channel 2 was used for the current and voltage measurements, respectively. To measure the EC current and voltage by an oscilloscope, resistors R1 (= 2000 MΩ), R2 (= 220 KΩ), and R3 (= 2.7 KΩ) were used in the voltage-divider configuration. Dummy devices (resistors: 1 MΩ, 2 MΩ) were tested at 1000 V, 2000V, and 3000 V for calibration.

Based on this assumption, the following equations can be used for the calculation of the current and voltage of EC cooling device:

$$I_{EC} = \frac{V_{Ch1}}{R3}$$

$$V_{EC} = \frac{V_{Ch2}}{R2} \times (R1 + R2) - V_{Ch1}$$

Here V_{Ch1} and V_{Ch2} are the reading of Channel 1 and Channel 2 of the oscilloscope. I_{EC} is the current of the device, and V_{EC} is the voltage of the device.

Figure 4-15 shows the voltage and current of an EC device at 0.8 Hz, and the calculated power consumption averaged over one cycle is determined to be 2 mW/cm^2 under an applied electric field of 66.7 MV/m and an electrostatic field of 61MV/m.

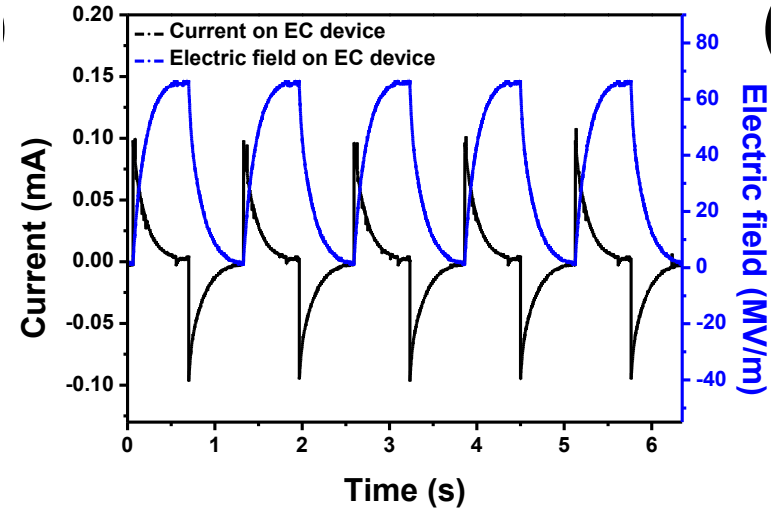

Figure 4-14. Power consumption of EC film under applied electric field of 66.7 MV/m.

4.3.4 Transient heat flux measurement

Leakage was found to be insignificant when compared to the charging and discharging currents of the EC film. Additionally, when the P(VDF-TrFE-CFE) cooling device operated without an electric field, there was no observed heat flux. This lack of heat flux indicates that joule heating from the electrostatic actuation is negligible.

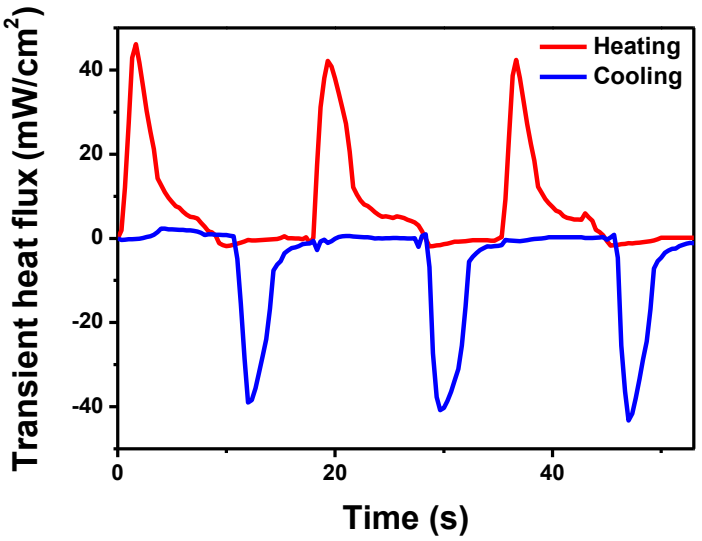

Figure 4-15. Comparison of heat flux measured by the heat flux sensor in both heating and cooling modes with an applied electric field of 50 MV/m and frequency of 0.06 Hz.

Joule heating from the electrocaloric effect was also found to be insignificant by comparing the heat flux in both heating and cooling modes with an applied electric field of 50 MV/m and a frequency of 0.06 Hz as show in Figure 4-15. During the cooling mode, an electric field is applied across the P(VDF-TrFE-CFE) film when the EC polymer stack is electrostatically attached to the heat sink, and the heat flux sensor on the heat source measures the heat flux due to cooling when the applied electric field is zero. Alternatively, in heating mode an electric field is applied when the EC polymer stack is electrostatically attached to the heat flux sensor. The same heat flux sensor now measures electrocaloric heating. If joule heating due to the electrocaloric effect generates an excessive amount of heat across the film, then the measured heat flux in the cooling mode would be smaller than the heat flux in the heating mode. The similar heat flux in both modes suggests that joule heating in the EC polymer stack is therefore insignificant. To verify that the measured effects are not transient, the heat flux of the P(VDF-TrFE-CFE) cooling device after

continuous operation for > 1 hr was found to have no deviation from the initial heat flux as shown in Figure 4-16. This measurement also supports the notion that joule heating within the device is not significant.

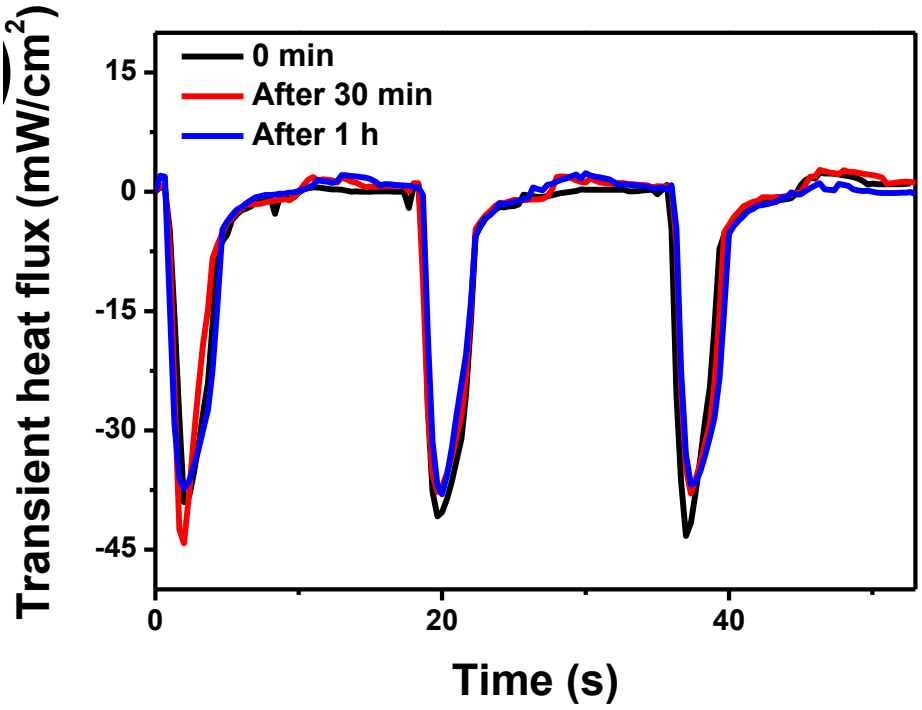

Figure 4-16. Cyclic testing of heat movement transport from the heat source to the EC polymer stack with an applied electric field of 50 MV/m and frequency of 0.06 Hz.

4.3.5 Device optimization

The average heat flux of the cooling device can be increased by operating at a higher frequency. Even at a frequency sufficiently low to allow the time required for the electrocaloric effect of the EC polymer stack to reach the change in temperature, as well as the time required for the movement of the EC polymer stack and the formation of a good thermal contact during τ_{delay}, the average heat flux is still less than optimal. Heat transport can be improved when the applied voltage on EC film was increased (See Figure 4-17). Under the applied EC electric field of 91.7 MV/m at the frequency of 0.05 Hz, 111.3

mJ/cm^2 of heat was moved in each cycle with a transient peak heat flux at 130 mW/cm^2. The average heat flux under this operation is 5.57 mW/cm^2.

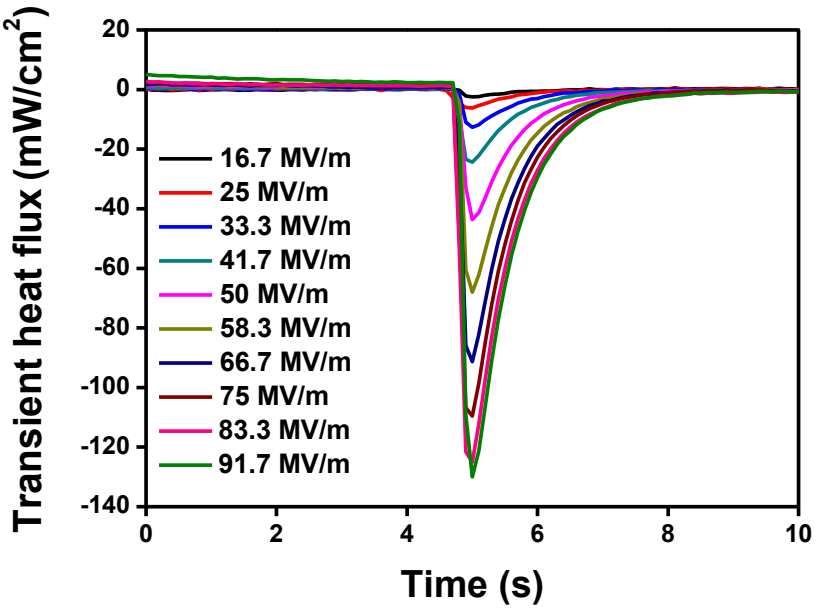

Figure 4-17. Heat transport as a function of applied voltage on EC polymer film with frequency of 0.05 Hz.

A higher average heat flux can be achieved at a higher frequency as shown in Figure 4-18. Figure 4-18 shows a direct relationship between average heat flux and frequency of a P(VDF-TrFE-CFE) cooling device under an applied electric field of 66.7 MV/m. Although the electrostatic actuation of the EC polymer stack can be much higher frequencies, the optimal frequency of the P(VDF-TrFE-CFE) cooling device was limited to 0.8 Hz. This limitation correlates closely with the expected value when the rate of heat dissipation from the heat sink to air is taken into account. In other words, the P(VDF-TrFE-CFE) cooling device transfers heat from the heat source to the heat sink faster than heat could be transferred from the heat sink to air at an operating frequency of 0.8 Hz.

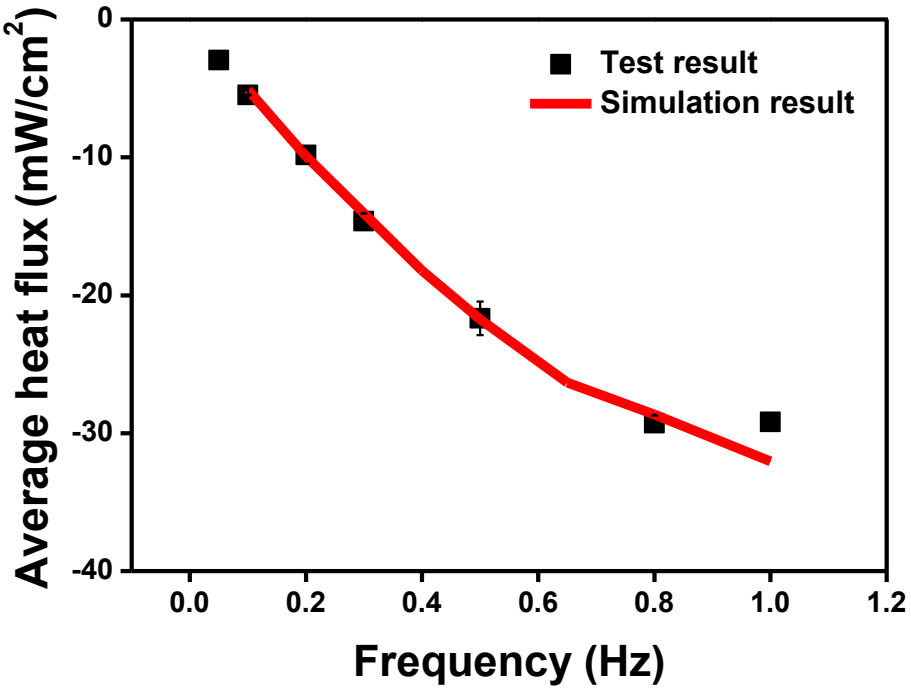

Figure 4-18. Heat flux as a function of different frequencies of operation. Simulation results, which were obtained by numerically solving the transient heat conduction equation using the finite volume method, agree well with the experimental value.

Another way to maximize heat flux is by optimizing the electric field of the EC polymer stack. Figure 4-19 shows the heat flux of a P(VDF-TrFE-CFE) cooling device operated at a frequency of 0.8 Hz as a function of the applied electric field. At a frequency of 0.8 Hz, the maximum electric field was set at 66.7 MV/m to avoid electrical instability of the P(VDF-TrFE-CFE) cooling device.

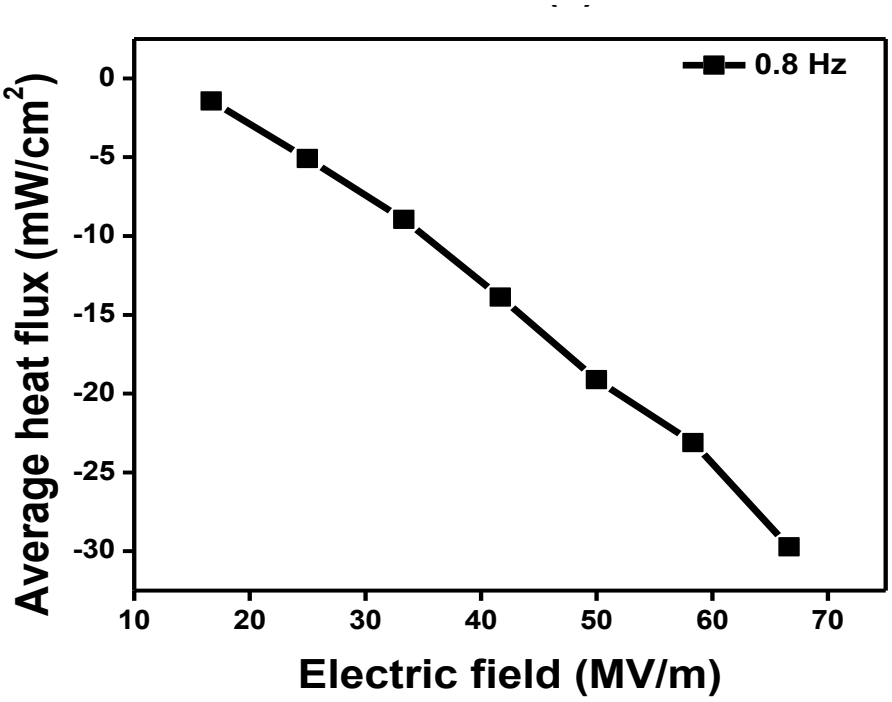

Figure 4-19. Heat flux of EC polymer film as a function of different applied electric field at 0.8 Hz.

Further refinement of the material processing or lamination techniques could allow for an increase in the maximum electric field and thus allow for significantly greater heat flow per cycle. Even without further improvements, a heat flux of 29.7 mW/cm^2 under an applied electric field of 66.7 MV/m was achieved, which corresponds to a specific cooling power of 2.8 W/g. This specific cooling power is 155 times higher than the highest reported cooling power of 0.018 W/g, calculated based on experimentally obtained heat flux data of other EC devices(*35*, *87*, *91*).

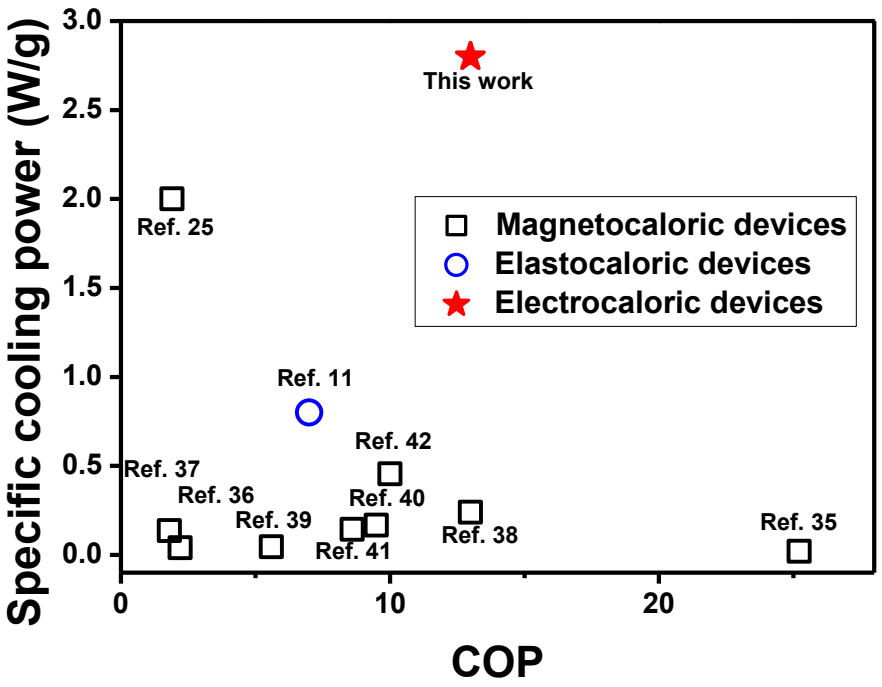

Figure 4-20. Specific cooling power with corresponded COP is compared with those of control magnetocaloric and elastocaloric devices.

Other than specific cooling power, COP is widely used to characterize the performance of active cooling devices(*8*, *92*). Based on calculation of $COP = \frac{Q_{transferred}}{W_{in}} = \frac{Heat\ transferred}{Electrical\ work\ in}$, a COP of 13 was reached with the P(VDF-TrFE-CFE) cooling device under an applied electric field of 66.7 MV/m at a frequency of 0.8 Hz. To date, there is no other experimentally obtained COP data in EC cooling devices. Figure 4-20 compares COP and specific cooling power of the P(VDF-TrFE-CFE) cooling device (filled symbol) with experimentally obtained COP and specific cooling power of magnetocaloric and elastocaloric devices in the reported literature (open symbols). The P(VDF-TrFE-CFE) cooling device reaches a specific cooling power of 2.8 W/g with a COP of 13, setting a new mark for solid state refrigeration.

4.3.6 Stress test of the EC cooling device

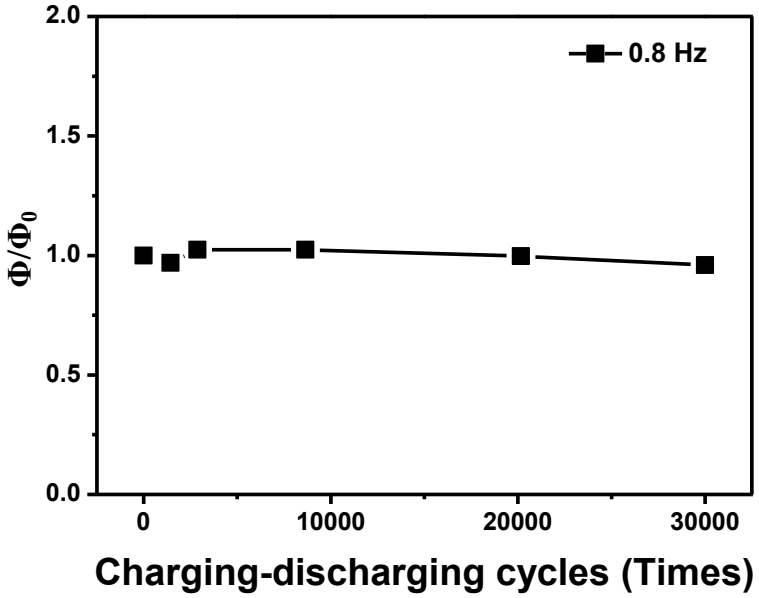

Figure 4-21. Measured heat flux change (Φ/Φ0) during repeated cycles of charging-discharging at the applied electric field of 50 MV/m (square wave, 50% duty cycle)

Figure 4-21 shows the heat flux change (Φ/Φ_0) during 30,000 cycles of charging-discharging at the applied electric field of 50 MV/m. The average heat flux of the EC device decreased by 4%. EC polymer stack did not show any signs of electrical failure or other damage. The EC device remained intact and functional after the test. The operational lifetime is expected to be much longer than 30,000 cycles, because in a separate measurement, the instantaneous breakdown electric field strength of the EC polymer was shown to be greater than 300 MV/m. The electrostatic force is uniform across the surface of the EC polymer stack. Localized stress concentration and friction induced failure often observed with externally driven mechanisms such as motors mechanically driven are minimized in the present EC device.

4.3.7 Cooling performance characterization

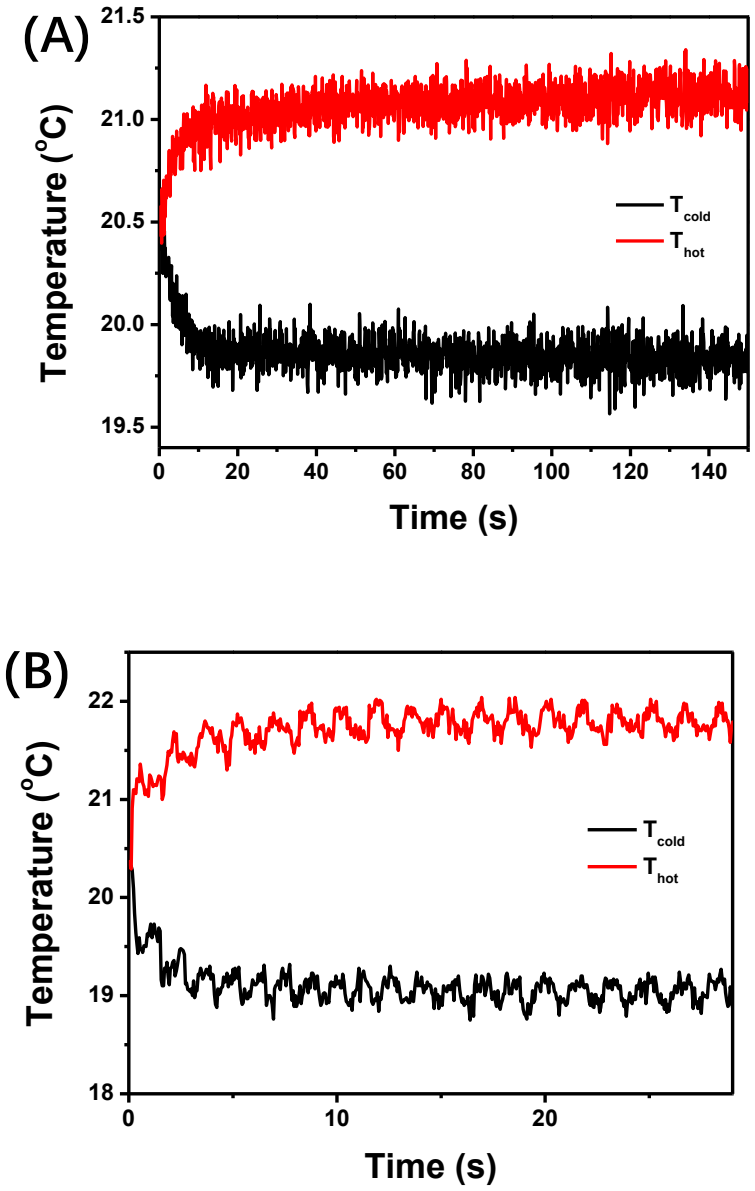

Figure 4-22. Measured temperature span between (A) thick Al (6.3 mm of thickness) heat sink and heat source, (B) thin PET (100 μm of thickness) heat sink and heat source.

Figure 4-22 shows the temperature span measured between the heat sink and source at 66.7 MV/m. With the thick aluminum block (6.3 nm thickness) used as the heat sink and source, the temperature span was 1.4 K. In the experiment, thermocouples were attached on the Al heat sink and heat source with Kapton tape (50 μm of thickness) to measure the

temperature. Note that there was a hump on the heat sink and heat source when the thermocouple was attached. This weakened the electrostatic effect between the EC polymer stack and heat sink or heat source, and thus the thermal contact was worse than in the actual EC devices. At the applied electric field of 66.7 MV/m, the heat flux was -15.9 mW/cm^2, about ½ of that in the EC devices. So, the practical temperature span should be higher than 1.4 K in the EC devices. To obtain a larger temperature span, EC devices were fabricated using carbon nanotube-coated polyethylene terephthalate (PET) film (100 μm of thickness) to replace the the Al heat sink and heat source. The temperature span increased to 2.8 K as shown in Figure 4-22(b).

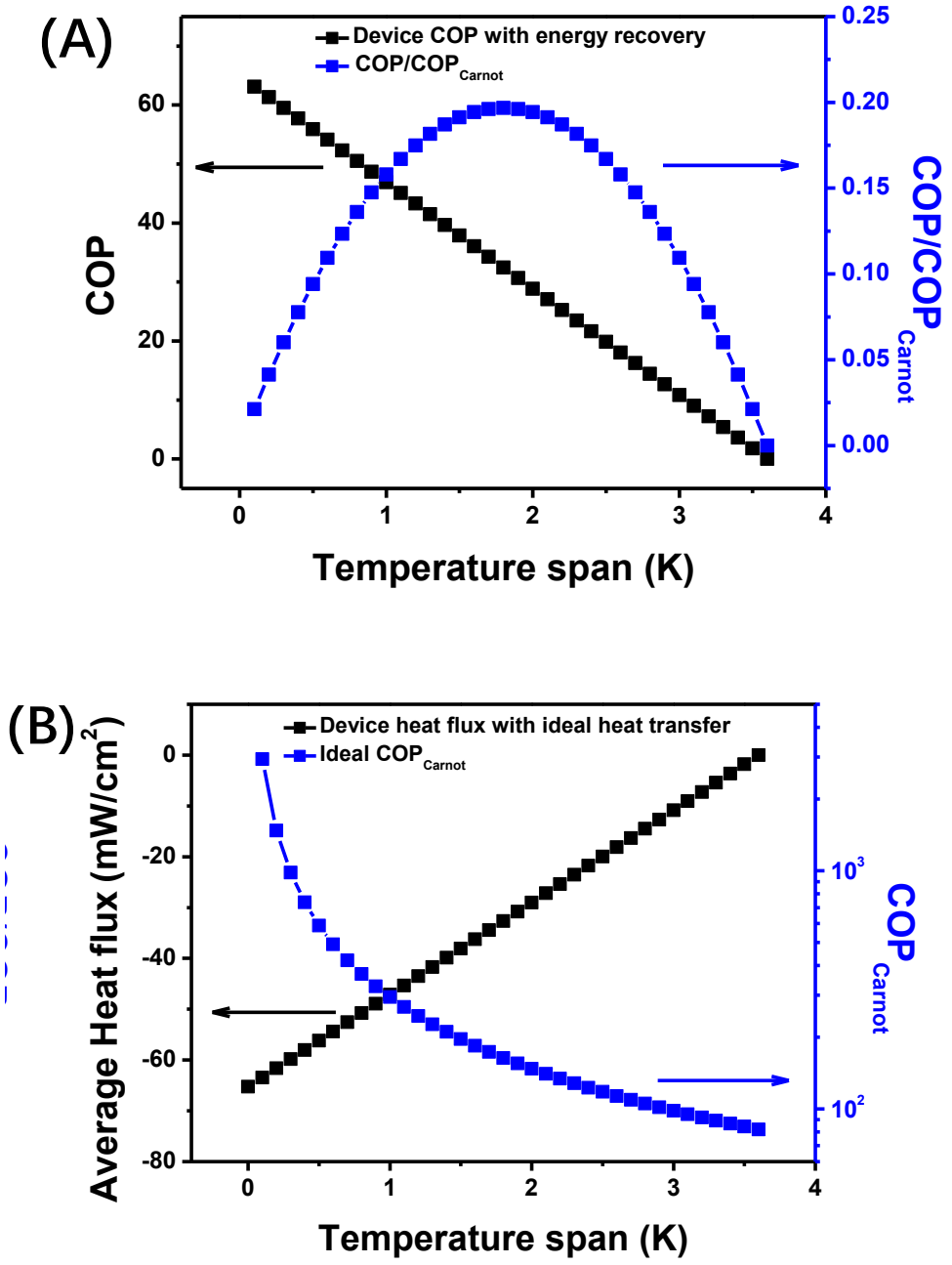

Figure 4-23. Simulated COP of the EC device, COP/COPCarnot and average heat flux as a function of temperature span between heat sink and heat source.

Figure 4-23 shows the simulated COP, COP/COP_{Carnot}, average heat flux and COP_{Carnot} as a function of temperature span between heat sink and heat source. Parasitic heat loss is ignored in the simulation. Heat capacities of the heat sink and heat source are

assumed to be much larger than the heat capacity of EC polymer stack, and the temperature of heat sink and heat source are constant. In each cycle, the thermal equilibrium between heat sink and source and EC polymer stack is reached and the temperature of the EC polymer stack is the same as heat sink and source after heat transfer. An energy recovery rate of 56% is used. These assumptions are made in order to best represent the experimental EC device, where aluminum plates are used as heat source and sink. The thermal capacity of these plates is much higher than the EC polymer stack since they have 194 times larger mass. The energy input data are used to calculate the COP. The measured adiabatic temperature change of EC polymer stack is 3.6 K. Due to the low temperature span of EC cooling device between thick Al heat sink and heat source, COP/COP_{Carnot} is smaller than elastocaloric, thermoelectric and some magnetocaloric devices. However, the specific cooling power and COP of EC device are much higher than these devices. So the temperature span between thinner heat sink and heat source will be larger, and COP/COP_{Carnot} will be improved.

Since the S-shaped EC polymer stack is inherently flexible, a flexible P(VDF-TrFE-CFE) cooling device was fabricated to demonstrate the potential to conform to curvilinear surface of objects to be heated or cooled. Figure 4-24a displays a flexible EC cooling device consisting of a transparent flexible frame made of conductive CNTs coated on a 100 μm thick PET that serves as the components for electrostatic actuation. The S-shaped EC polymer stack was fixed to a Polydimethylsiloxane (PDMS) frame spacer with a thickness of 4 mm.

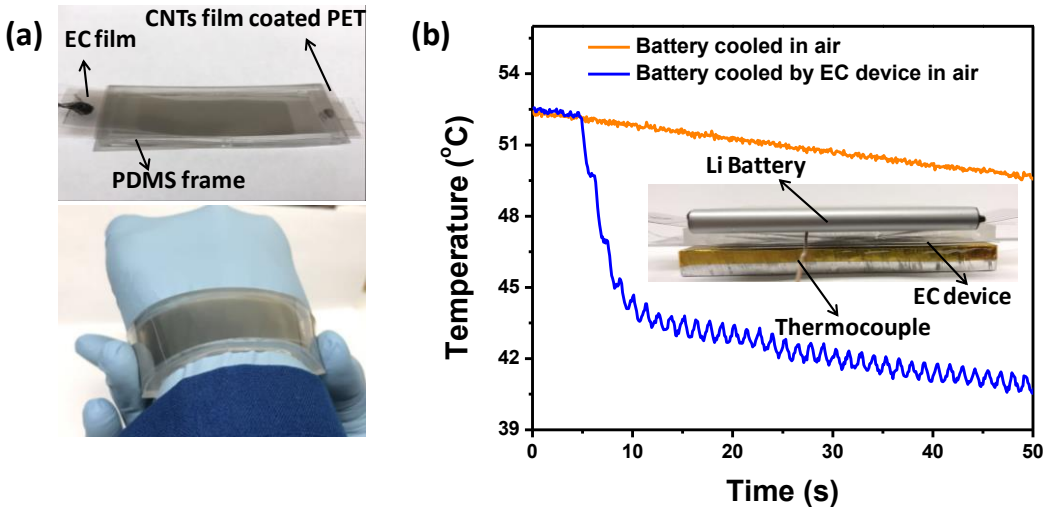

Figure 4-24. Performance of the flexible EC cooling device. (a) Photograph of flexible EC device. (b) Temperature change of overheated smartphone battery with and without EC cooling device. The inset is overheated battery on the top of the EC device.

The device geometry is 7 cm x 3 cm x 0.5 cm. Its cooling power was demonstrated by attaching it onto a typical smartphone battery (Samsung Galaxy S4). Under high workloads in a smartphone, the battery heated to 52.5 ˚C. When allowed to cool in air, the surface temperature of the battery measured with a surface mount thermocouple decreased by 3 ˚C in 50 s (Figure 4-24b). After the flexible EC cooling device was attached to the battery, the surface temperature of the battery was observed to decrease by 8 ˚C in the first 5 s with EC cooling activated under an applied field of 66.7 MV/m at 0.8 Hz. Overheating of smartphone batteries under high workloads creates a fire hazard, and prolonged use under thermal overload causes reduced battery lifetime and fatigue of other materials and components in the smartphone. Our flexible cooling approach could potentially solve this problem.

4.4 Conclusion

In conclusion, a solid-state cooling device with a high specific cooling power of 2.8 W/g and a COP of 13 has been obtained based on an electrostatically actuated P(VDF-TrFE-CFE) polymer stack. Thanks to the light weight of the EC polymer stack, electrostatic forces can rapidly transport the S-shaped EC polymer stack while promoting intimate thermal contact between the EC material and the heat source/heat sink. An EC polymer cooling device with a flexible form factor has also been demonstrated. The high COP, high heat flux, compact and flexible form factor operation should find applications in wearable and mobile devices where no current active cooling technologies are suitable.

5 Stretchable Transparent Wireless Charging Coil

5.1 Introduction

Wearable electronics, such as smartwatch, VR (Virtual Reality)/AR(Augmented Reality) smart glasses, and E-textiles, are an emerging technology platform that is reshaping the way people interact with the surrounding world(*93*). Powered by rapidly evolving telecommunication technologies and the ever-growing computing capabilities of microchips, these devices make ubiquitous computing possible and pervasive in daily life. Wearable devices are adapted for human comfort by using both aesthetically pleasing and functionally versatile designs. This is achieved by creating flexible, light-weighted, and sometimes even stretchable materials. Scientists are challenged to achieve high levels of integration of various functionalities including displays, microprocessors, sensors, batteries, communications units, etc., via novel design and innovative materials. Specifically, the limited lithium-ion battery (LIB) power source can be a critical issue causing short operational/standby times and frequent charging(*94*). To mitigate this issue, energy harvesting technologies like solar cells, thermoelectric generators, and nano-generators have been reported(*95–97*). However, the intermittent nature and low power output of these technologies is an inevitable problem that limits their use as power sources for wearable electronics.

Wireless power transfer (WPT), through which electrical energy is transferred without wires as a physical link, is widely regarded as a promising and preferable power recharging method for wearable electronics. Comparing to traditional technologies, i.e. charging via cord, wireless charging shows many advantageous qualities. Firstly, WPT relies on the receiving coil to harvest electromagnetic energy and requires no openings to

charge. This makes it much easier to design and fabricate wearable devices that meet the user requirements and can survive in harsh environments (e.g., waterproof and dust-proof). Secondly, as a contact-free technology, WPT can be used to power or recharge devices where installing cables is costly and infeasible, especially for medical applications like pacemakers and bladder urine monitoring(*98–101*). Traditionally, wireless charging coils have been fabricated by patterning metals on rigid substrates or directly from metal wires. It is challenging to make these coils compatible with the soft and flexible components of wearable devices; this shortcoming suggests the need for more ductile alternatives. Xu et al. reported a wireless charging system enabled by serpentine wire connections embedded in a polymer. The device can be stretched to 3 times its original length and still keeps its original functionality(*102*). Jeong et al. introduced a liquid alloy based stretchable wireless charging coil fabricated by liquid alloy atomization process(*103*). The coil can survive cycling between 0% and 25% strain over 1,000 cycles. These reported devices can achieve high flexibility and wireless charging for wearable electronics, but the fabrication processes are cumbersome and incompatible with the solution-based process. The materials used are costly and expensive to scale up. Additionally, as AR/VR technologies are rapidly adopted, the display becomes an essential part of many wearable electronics. Metal wires may block users' vision and introduces tremendous challenges for engineers during integration. To address this issue, mechanically stretchable and optically transparent wireless charging coils are needed for wearable electronics.

Silver nanowire (AgNW) is considered one of the most promising stretchable and transparent conductors thanks to its mechanical compliance and electrical conductivity(*46*). Recently, AgNWs have been extensively studied for various applications including organic

light emitting diodes (OLED)(*43*, *104*), thin-film transistors (TFT)(*105*), organic photovoltaics (OPV)(*106*, *107*), and electronic skins(*108*). Yu et al. fabricated a stretchable and transparent conductor by incorporating the AgNW network in a transparent polyacrylate elastomer(*44*). The AgNW network acts as the electrical conducting back-bone and provides an excellent electrical conductivity while maintaining high transparency. Hu et al. improved the performance of the AgNW/acrylate composite by adding an aromatic monoacrylate (Sartomer CN131) and acrylic acid (AA) to the precursor. The presence of carboxylic acid groups allows a good bonding between AgNWs and the polymer matrix, enhances the stretchability and durability of the as-fabricated transparent conductor.

Here we present the successful development of transparent and stretchable wireless charging coils, using the negative adhesive transfer printing (NATP) method. The work includes the following components: (1) The stretchable transparent conductor is based on AgNW-polyurethane acrylate (PUA) composite with high conductivity and robustness under harsh mechanical treatment (bending and stretching). (2) The NATP method is designed to pattern highly conductive transparent electrode by removing AgNWs within the negative area. Unlike other transfer methods(*109*, *110*), the NATP keeps the high conductivity of the printed area, avoids contamination and disconnection between AgNWs. A 50 μm wide AgNW strip was printed to demo the precision and resolution of the NATP method. The NATP's resolution is primarily determined by the stamps. High-resolution elastomeric stamps have been developed for transfer printing and fabrication of microelectronics like micro light emitting diode (micro-LED) through "pick-and-place" technique(*111–113*). It is feasible to scale NATP down for high-resolution printing. (3)

The as-fabricated stretchable transparent coil is used as the receiver coil for wireless charging and can drive a LED bulb at full brightness range. The wireless charging coil is still functional after 1000 times bending and stretching cycles. (4) The wireless charging coil is optimized and studied using finite element analysis.

5.2 Experimental section

Materials. Silver nanowire (AgNW) was purchased from Kechuang Adv. Mater. Tech Co. Ltd. (average diameter: 23-35 nm; average length: 10-20 μm), 2,2-dimethoxyl-2-phenylacetophenone (99%, DMPA) was obtained from Sigma-Aldrich. UA (CN990), and EBA (SR540) were supplied by Sartomer. VHB was purchase from 3M.

AgNW-PUA Composite Fabrication. AgNWs solution was used as received and diluted to around (2mg/mL) in isopropanol (IPA). a Meyer rod was used to coat the AgNW onto a glass substrate. By coating the AgNW repeatedly, we can get AgNW network with higher conductivity and lower sheet resistance. The adhesive stamp was applied onto the AgNW layer and was heated up to 100 C for 10 mins. The adhesive stamp was removed as well as the AgNW under it. A precursor solution consisting of CN990 (UA), SR 540 (EBA), and DMPA (photoinitiator) (weight ratio 100:20:1) was coated onto the printed AgNW pattern. An ultraviolet curing machine (Dymax ultraviolet conveyor equipped with 2.5 W/cm^2 Fusion 300S type "H" ultraviolet curing bulb) was used to cure the composite at a speed of 1.0 feet per min for one pass before peeling off as a free-standing AgNW-PUA conductive composite.

Characterization: The transmittance of the as-fabricated AgNW-PUA was measured by Shimadzu UV-1700 spectrophotometer. The stretching and relaxing tests were performed on a motorized linear stage with a built-in controller (Zaber Technologies). A Keithley 2000 digital multimeter was used to monitor resistance changes. Strain and resistance data were recorded via a custom-made LabView code. All measurements were carried out at room temperature. Agilent 33250A Arbitrary function generator was used to supply AC power to the Tx coil. Rigol DS1054Z was used to record the electric power received by the

Rx end. SEM was performed on a JEOL JSM-6701F scanning electron microscope. AFM measurements were carried out in PeakForce QNM (Quantitative NanoMechanis) mode on a Bruker dimension icon scanning probe microscope at ambient conditions. A commercial silicon cantilever (RTESPA-150) was used in this study with a typical radius of curvature of ~8 nm and a nominal spring constant of ~5 N/m.

5.2.1 Fabrication of AgNW-PUA nanocomposite

The fabrication process of the stretchable transparent coil is illustrated in Figure 4-1. The aspect ratio (length-to-width) of AgNWs is a critical factor to achieve high stretchability and conductivity(*114*). Long AgNWs provides longer percolation paths and reduces the density of inter-nanowire contacts where the contact resistance plays a significant role. AgNWs with an aspect ratio around 1,000 was used as a conductive backbone in the composite (Figure 5-2). The Meyer rod coating technique is a scalable fabrication process to yield high-quality AgNW transparent conductor(*115*). To prepare a uniform layer of AgNWs ready for NATP, AgNW solution was rod-coated on a slice of clean glass. Coating times can be adjusted to yield an AgNW layer with different conductivity.

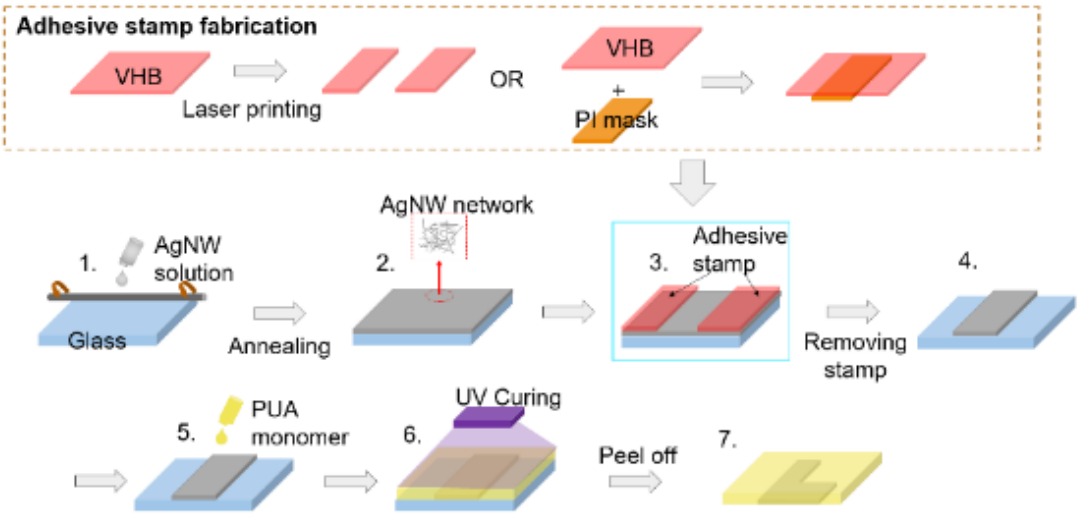

Figure 5-1. Schematic illustration of the steps of the NATP method.

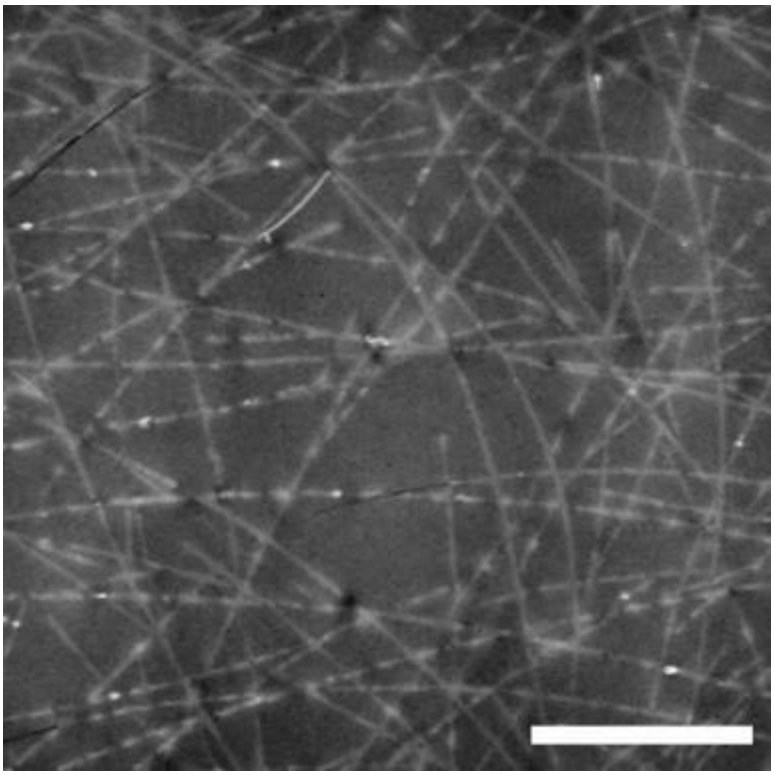

Figure 5-2. AFM of AgNW-PUA nanocomposite. Sheet resistance ~ 10 ohm/sq. Scale bar is 2 micron.

For a successful negative transfer print, it is critical to identify a stamp material that is compatible with the material to be printed. Polydimethylsiloxane (PDMS) rubber has

been widely studied for its excellent processability and mechanical properties(*113*). However, limited by the weak bonding between AgNWs and PDMS surface, it is not feasible to use PDMS as the NATP stamp. A commercially available adhesive elastomer VHB (an acrylic elastomer film from 3M) is an excellent material to use as the negative printing stamp thanks to its excellent bonding strength and ease to process. The carboxylic acid functional group and carboxylic ester groups of VHB tend to have a strong bonding with the AgNWs and facilitate the transfer process(*43–45*). The negative of the desired pattern was laser-printed and directly applied to the AgNW layer. To further enhance the interaction between adhesive stamp and AgNWs, thermal treatment at 100 ^{o}C for 10 min was applied before the negative stamp was peeled off the glass substrate. The AgNWs not covered by the adhesive stamp was remained on the substrate and retained the high conductivity and good transparency.

Figure 5-3.Optical image of printed AgNW pattern on glass (sheet resistance: 6 Ohm/sq)

Figure 5-3 shows the printed AgNW pattern on the glass as the letters “U”, “C”, “L”, and “A”. To further increase the conductivity, AgNW patterns on glass were heated to 150 C for 10 mins to ensure good wire-to-wire contact(*45*, *109*).

The precursor of PUA was then was onto the printed AgNW pattern on glass and UV-cured. PUA is a rubbery polymer copolymerized by a siliconized urethane acrylate oligomer (UA) and an ethoxylated bisphenol A dimethacrylate (EBA). UA provides high transparency and excellent mechanical properties, especially stretchability. EBA enhances the bonding between AgNWs and the polymer matrix for better compatibility between the polymer component and metallic nanowire to suppress delamination and formation of voids and cracks while bending, stretching and twisting. The PUA films fabricated for wireless charging coils has a UA:EBA ratio of 5:1(*43*). A scotch tape test was done to test the robustness of AgNW-PUA composite. After 100 tests, the conductivity of AgNW-PUA composite did not change, showing a strong bonding between the PUA matrix and AgNW network.

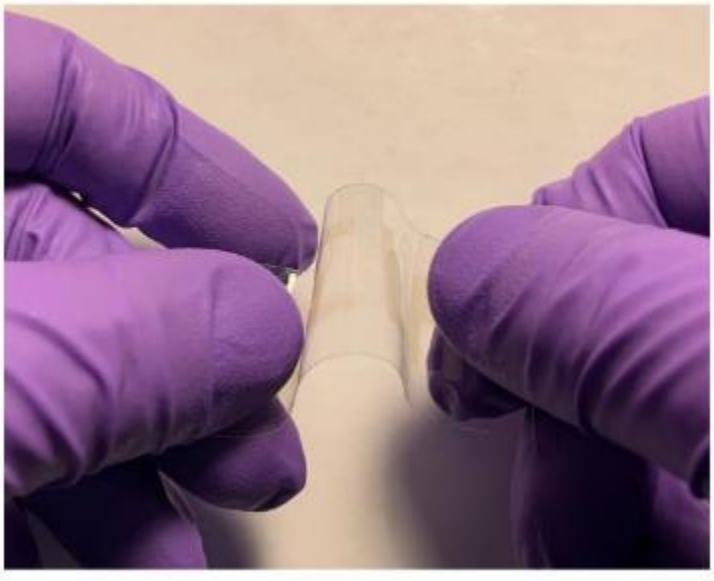

Figure 5-4.Photograph of a free-standing AgNW-PUA composite with the printed pattern

Figure 5-4 presents a photograph of a free-standing AgNW-PUA thin film with printed AgNW patterns. The conductive region remained highly conductive (~ 6.3 Ohm/sq) and transparent. The NATP technique can potentially print a wide range of shapes and sizes. To demonstrate its precision, a stripe around 50 microns wide was printed, and the edge is smooth and clear-cut (Figure 5-5).

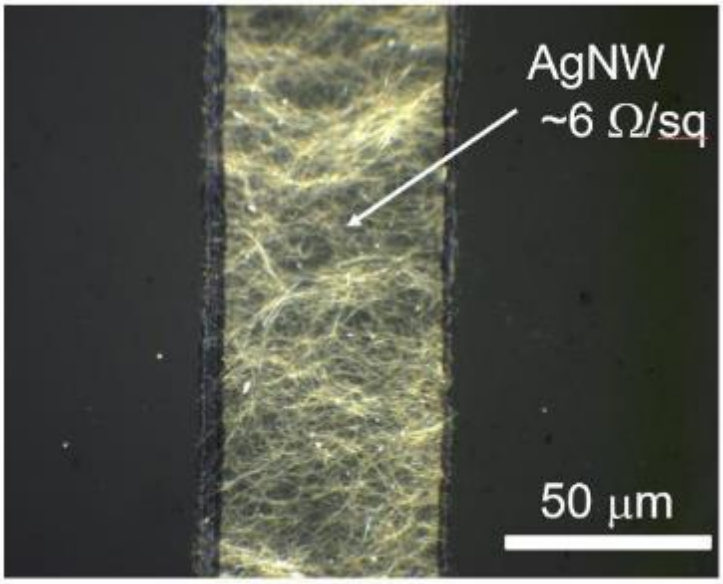

Figure 5-5. Optical microscope image of a line of AgNW printed by the NATP method to show its resolution (reflectance optics)

The photograph is taken by a reflective microscope. It is noteworthy that the AgNWs have an average length of 30 microns. For the AgNWs locate near the edge, the shear-force between the stamp and AgNW network cuts the AgNWs.

5.2.2 Characterization of NATP fabricated AgNW-PUA

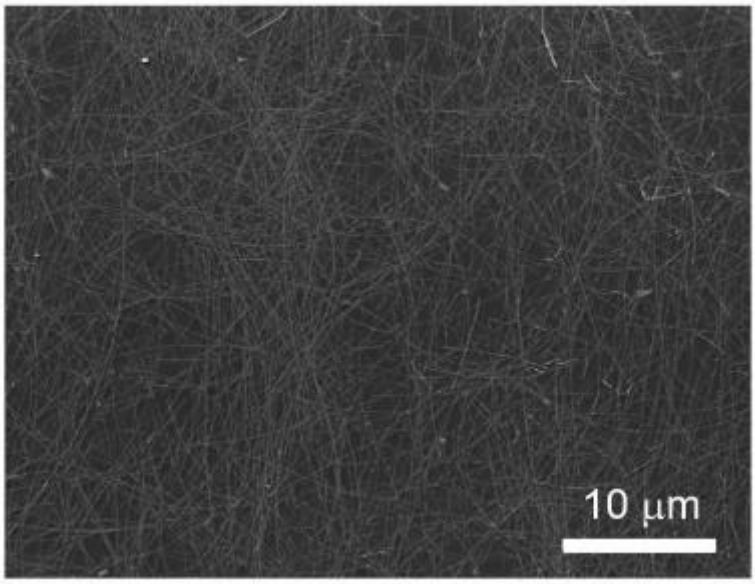

Figure 5-6. SEM image of the conductive surface of the NATP-printed AgNW-PUA composite (sheet resistance: ~ 6 Ohm/sq).

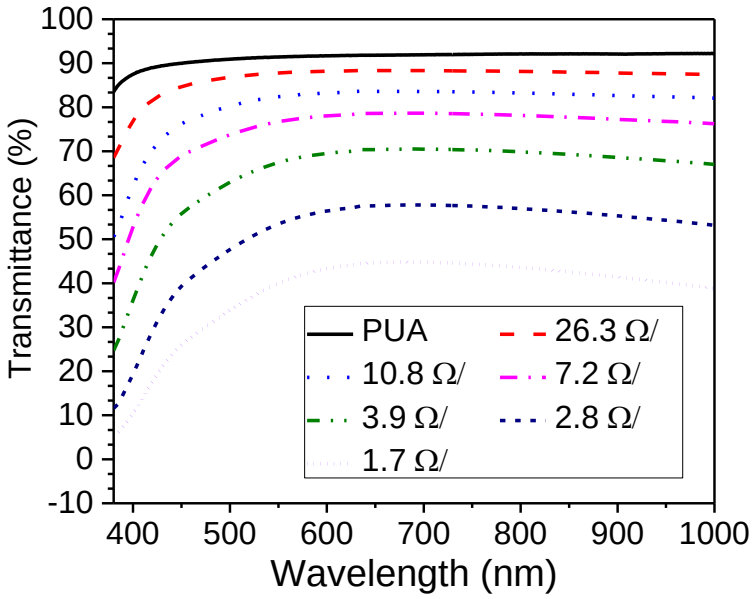

Figure 5-7. Transmittance spectra of AgNW-PUA composites with difference sheet resistances. PUA thickness is 90 micron.

The AgNWs printed by the NATP method is well dispersed and embedded in the PUA matrix (Figure 5-6). The sample has a sheet resistance of 6.3 ohm/sq. Figure 5-7

shows the transmittance spectra of the AgNW-PUA composite with various sheet resistance. The composite films are around 90 μm thick and the blank PUA film has a transmittance of 92% in the wavelength range of 400 nm to 1000 nm. The transmittance at 550 nm is 88% when the sheet resistance is 26.3 ohm/sq; 84% at 10.6 ohm/sq; 79% at 6.3 ohn/sq; 70% at 3.9 ohm/sq; 58% at 2.8 ohm/sq and 45% at 1.7 ohm/sq, which are comparable to the commercial indium tin oxide (ITO)/polyethylene terephthalate (PET) electrodes[19]. The following equation can be used to describe the relationship between the transmittance and sheet resistance for the thin transparent conductive film(*116*):

$$T(\lambda) = (1 + \frac{188.5}{R_S}\frac{\sigma_{Op}(\lambda)}{\sigma_{DC}})^{-2} \quad (1)$$

where $T(\lambda)$ is the transmittance at wavelength λ, R_S is the sheet resistance of the characterized thin film, $\sigma_{Op}(\lambda)$ is the optical conductivity at wavelength λ, and $\sigma_{DC}$is the direct current (DC) conductivity of the film. σ_{DC}/σ_{Op} is a dimensionless number used as a figure of merit to describe the transparency at given sheet resistance for transparent conducting films. A high σ_{DC}/σ_{Op} ratio indicates a low sheet resistance at given transmittance. For the AgNW fabricated by the NATP method, σ_{DC}/σ_{Op} is around 300 (Figure 5-8).

Because of the localized surface plasmon resonance, the AgNWs shows a high absorbance in the deep blue region (around 400 nm)(*117*).

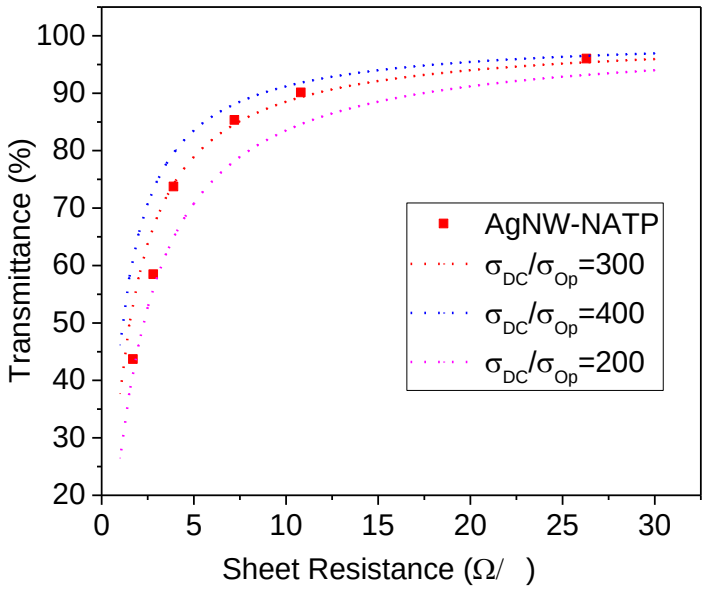

Figure 5-8. The sheet resistance of AgNW-NATP vs. its transmittance

The mechanical properties of the composite are largely dominated by those of the PUA elastomer because the thickness of AgNWs layer (~100 nm) is several orders of magnitude lower than that of the elastomeric substrate (~90 μm). To evaluate the flexibility of the as-fabricated AgNW-PUA composite, a cyclic bending test was conducted. The set-up is shown in the inset photograph of Figure 5-9. A linear stage was used for precise control of the bending radius. The curvature radius of the AgNW was 3 mm, and the resistance of the AgNW-PUA strip was measured dynamically during the test. The original sheet resistance of the AgNW-PUA composite was 3.9 ohm/sq and increased only by 7.5% to 4.2 ohm/sq after 600 cycles. Bending shows little mechanical or electrical damage to the stretchable transparent coil thanks to its high flexibility and strong bonding between the PUA and AgNWs.

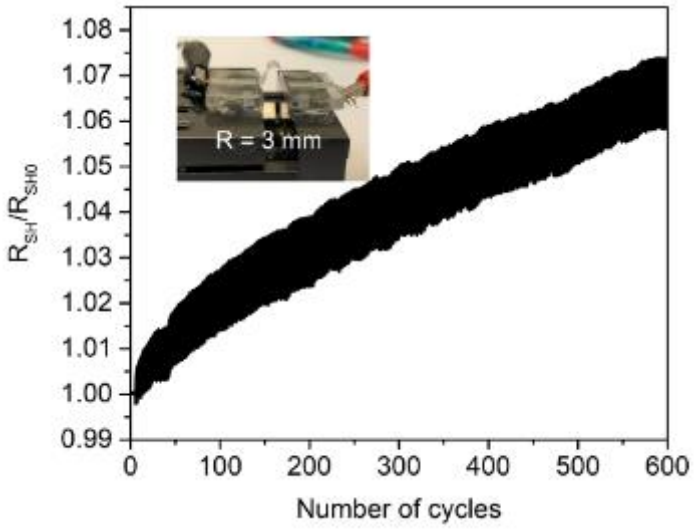

Figure 5-9. Normalized transient resistance of AgNW-PUA during cyclic bending and releasing (bending radius: 3 mm).

To further investigate the stretchability of AgNW-PUA composite, a uniaxial strain up to 60% was applied to samples with different AgNW densities and conductivities. As shown in Figure 5-10, At 10% strain, the sheet resistances of the 10.8 ohm/sq sample increased to 24.0 ohm/sq, and 10.4 ohm/sq, 4.7 ohm/sq, 4.4 ohm/sq, and 2.2 ohm/sq for 7.2 ohm/sq, 3.9 ohm/sq, 2.8 ohm/sq, and 1.7 ohm/sq samples respectively.

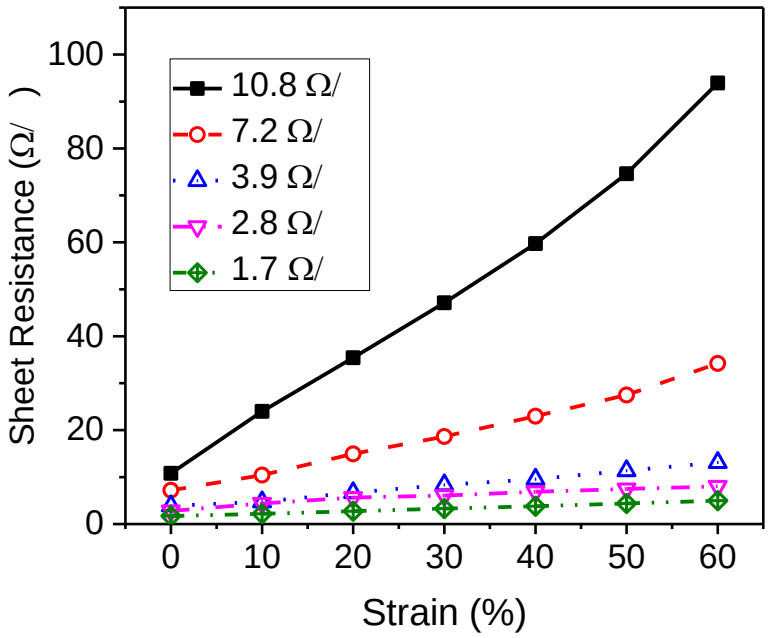

Figure 5-10. Sheet resistance of the composites as a function of tensile strain.

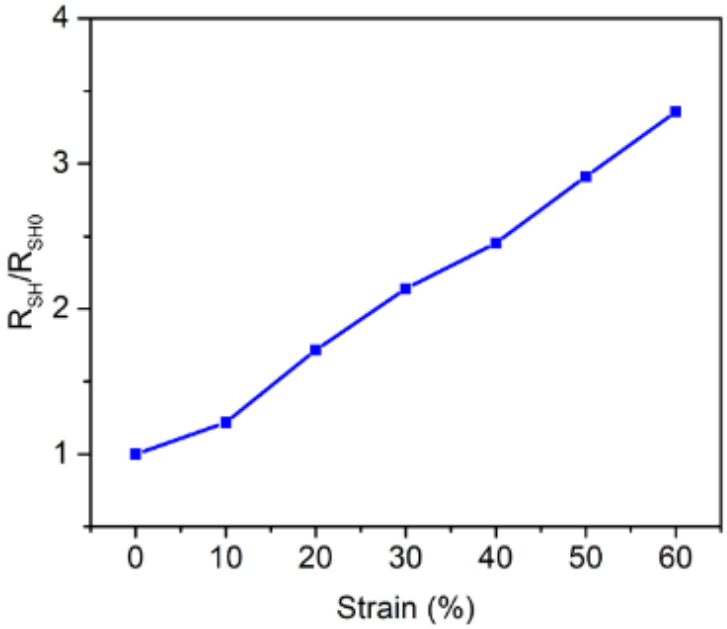

Figure 5-11. Normalized sheet resistance change of the 3.9 Ohm/sq sample verse tensile strain.

The AgNW-PUA samples with low sheet resistance tended to have less sheet resistance increase when stretched. It is because within the conductive composite, AgNW

network acts as the conducting back-bone and the junction resistance is critical for the overall conductivity(*115*).

For composites with low sheet resistance, the AgNW layer is denser and the alternative charge pathways can be taken when the sliding and disjointing between AgNWs occurs. Figure 5-11 represents the normalized sheet resistance change of the 3.9 Ohm/sq sample verse tensile strain. Under a strain of 50%, the sheet resistance of the stretched composite is still less than 3 times (11.4 ohm/sq) of the original value (3.9 ohm/sq).

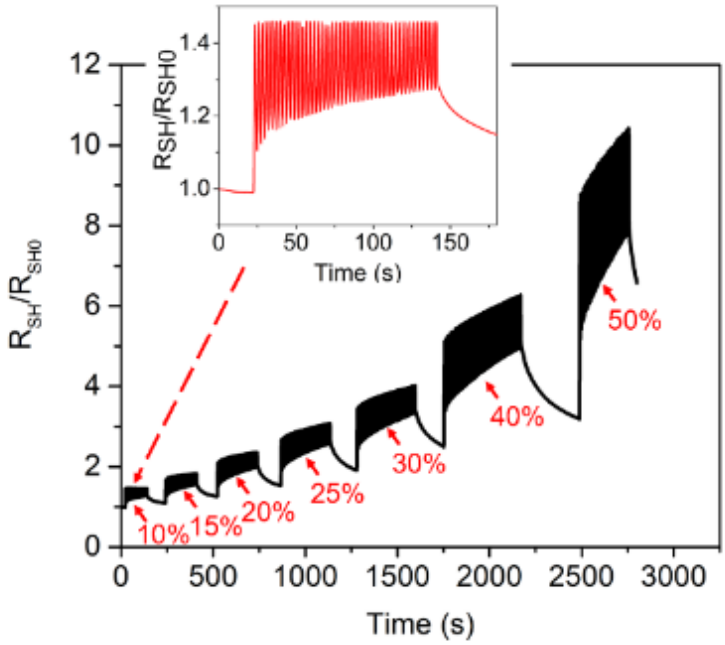

Figure 5-12. Normalized transient resistance of AgNW-PUA during cyclic tensile stretching and releasing.

Figure 5-12 illustrates the normalized transient resistance of the AgNW-PUA composite (3.9 ohm/sq) during cyclic tensile stretching and releasing test. Figure 5-13 and Figure 5-14 show comparison between AgNW-PUA composite fabricated by the NATP method and other transparent conductors reported. The AgNW-PUA composite demonstrates transmittances similar to ITO coated PET and unparalleled advantages such as easy processability and excellent stretchability.

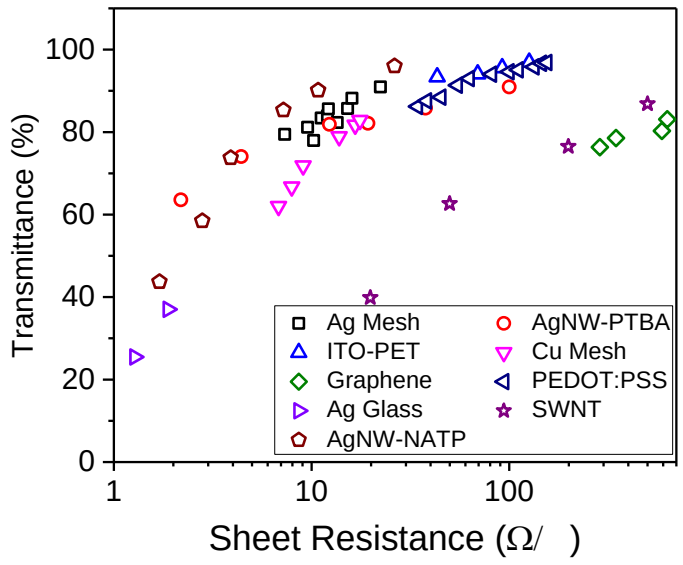

Figure 5-13. Plots of transmittance (at 550 nm wavelength) as a function of sheet resistance of Ag mesh[34], AgNW-thermoplastic-poly(t-butylacrylate) composite (AgNW-PTBA)[19], ITO coated on PET (ITO-PET)[19], copper mesh[35], graphene, PEDOT:PSS[36], Ag thin film on

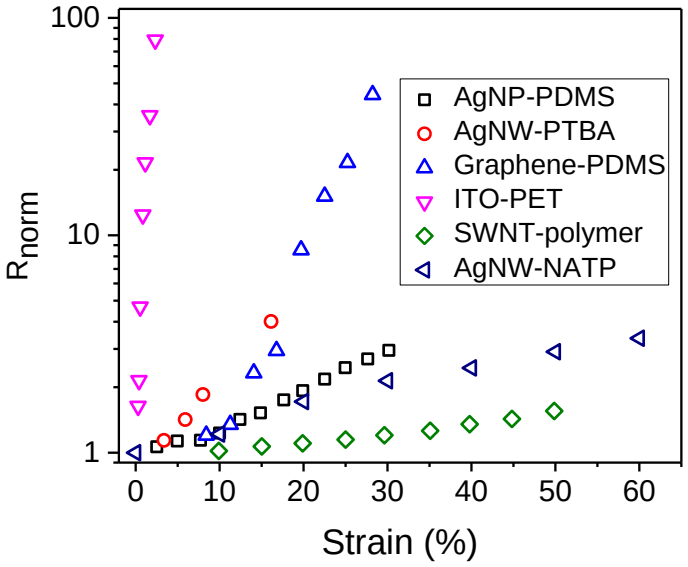

Figure 5-14. Plots of normalized resistance of various stretchable conductor as a function of tensile strain including silver nanoparticle on PDMS (AgNP-PDMS)[37], AgNW-PTBA[19], graphene on PDMS[38], ITO-PET[19], SWNT-polymer[19], and AgNW-NATP (this work).

5.3 Result and discussion

5.3.1 WPT coil design and optimization

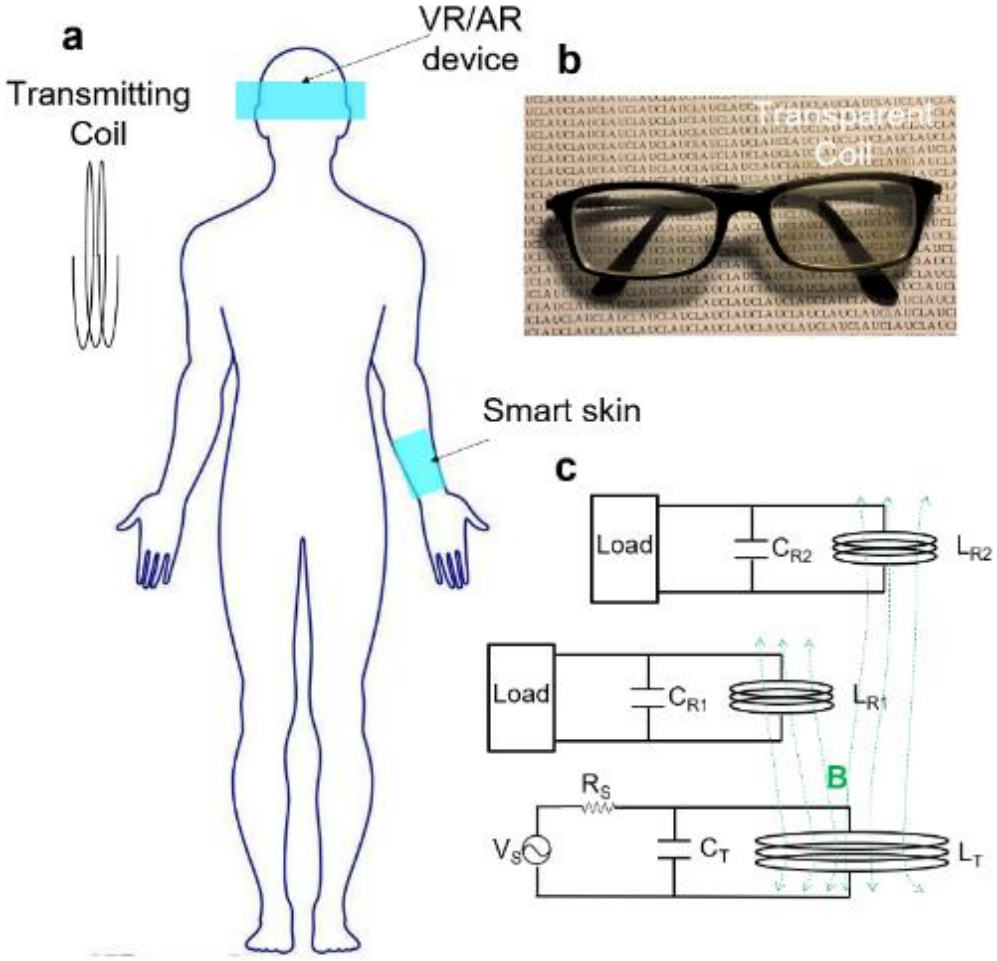

Figure 5-15. (a) Concept diagram of multi-device wireless power transfer. (b) WPT coil on glasses. (c) Circuit schematic of the WPT system consisting of one transmitter and two receivers.

Based on the stretchable transparent AgNW-PUA composite, a conceptual diagram of wireless power transfer system for wearable devices is illustrated in Figure 5-15(a). A transmitting (Tx) coil acts as the power source and generates oscillating electromagnetic waves. The receiving (Rx) coils harvest the energy wirelessly through inductive coupling. When sinusoidal alternating current (AC) is applied across the Tx coil, an oscillating magnetic flux is generated. The Rx couples the time-varying magnetic flux and an

alternating current (AC) is induced. Since the transmission of electromagnetic wave requires no medium, the power transfer can be established without physical contact and across gaps.

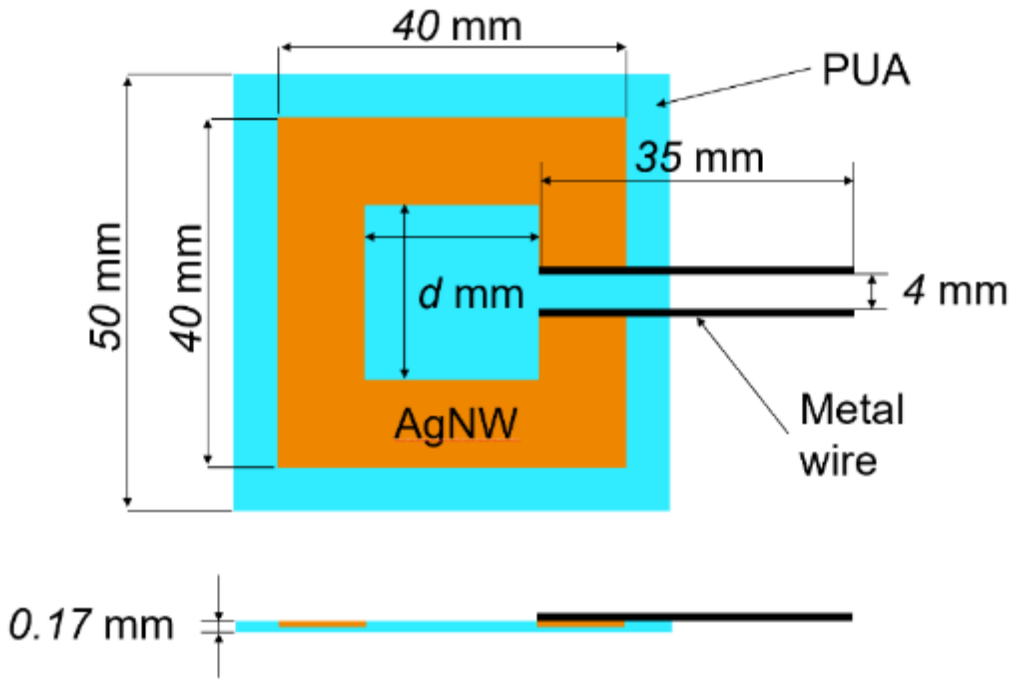

Figure 5-16. physical diagram of the single-turn coil in this work.

Kurs et al. demonstrated an efficient energy transfer of 60 watts over 2 meters via WPT(*39*). Because of the excellent transparency, flexibility and stretchability of the AgNW-PUA fabricated via the NATP method, it shows a great potential acting as the Rx coil for wearable electronics. Figure 5-15(b) presents a photograph of the WPT coil on glasses and illustrate the feasibility to integrate the transparent Rx coil onto AR devices without blocking the users' vision. The coil has a sheet resistance of ~ 3 ohm/sq. The physical diagram is shown in Figure 5-16 of Supporting Information. Finite element analysis was conducted for the coil optimization (Figure 5-17, 18, 19).

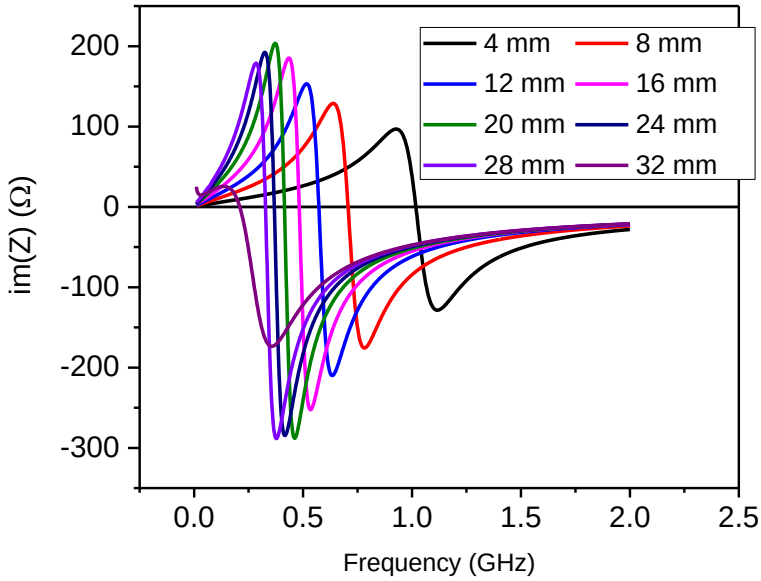

Figure 5-17. The simulated imaginary impedance of the coils with different inner opening widths (d mm) . The physical diagram of the coil as shown in Figure 5-16. sheet resistance is 3 ohm/sq.

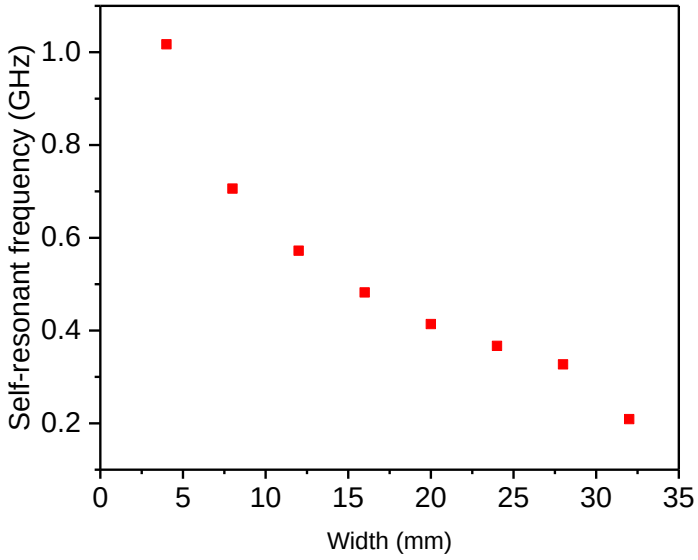

Figure 5-18. Simulated self-resonant frequencies of coils as a function of the opening size (d mm).

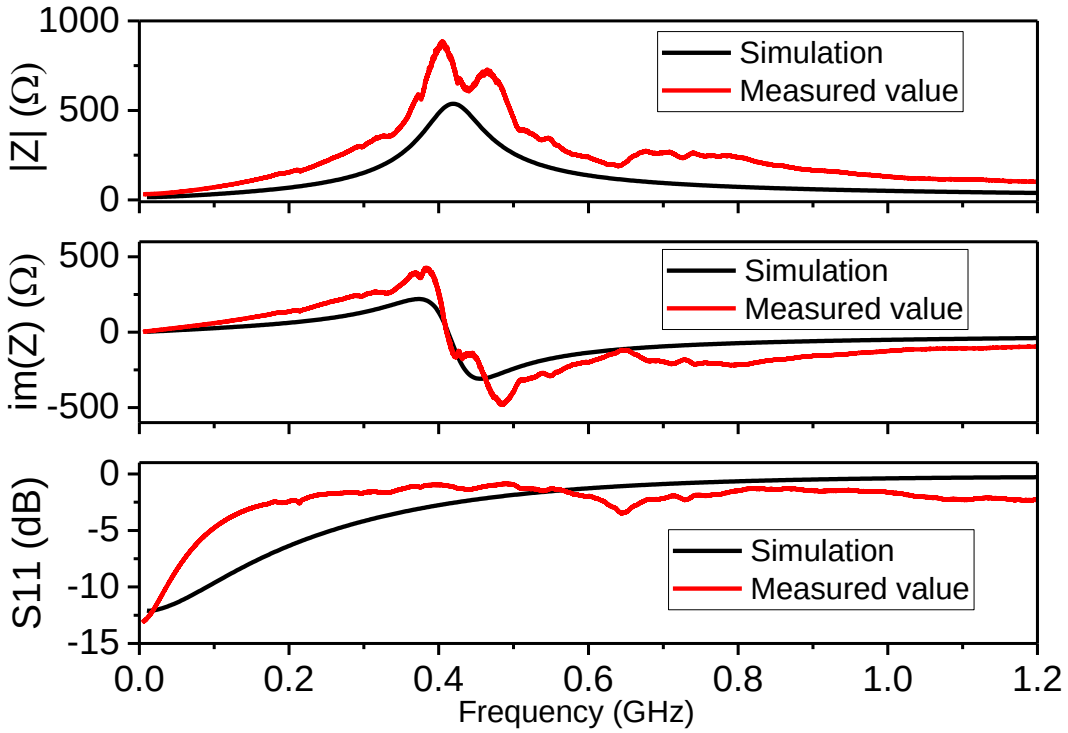

Figure 5-19. Measured and simulated impedance (|Z|), imaginary impedance (im(Z)), and S11 parameter of the coil with d = 20 mm, sheet resistance = 3 ohm/sq

A single turn square coil with a total width of 40 mm and an opening width of 20 mm was selected for the balance of resistance and inductance. To mimic the effect of wearing smart glasses with the NATP fabricated AgNW Rx coil, photographs were taken without and with the coil (Figure 4-20). Figure 5-20 b and c demonstrate the coil's high transparency. There is little difference between the two photographs.

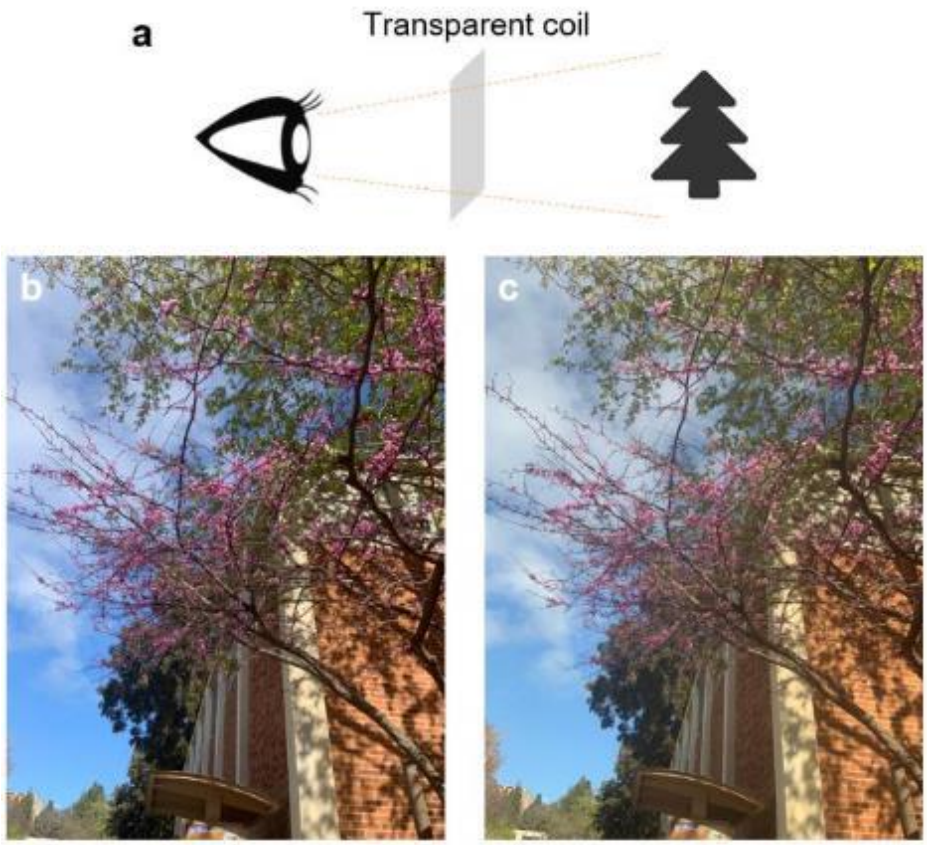

Figure 5-20. (a) Illustration of seeing through the transparent coil. (b), (c) shows pictures without (b) and with (c) "eye" covered. Pictures were taken by iPhone XR rear camera to mimic the condition.

5.3.2 WPT characterization

In order to verify the potential of the NATP fabricated AgNW-PUA nanocomposite as a wireless power transfer (WPT) component), we performed a pilot study. For the receiver to harvest maximum power, the operational frequency should be around its resonant frequency(*39*, *98*, *118*). The resonant frequency can be derived as follows, $f_R = \frac{1}{2\pi\sqrt{L_R C_R}}$, where f_R is the resonant frequency of the Rx coil, and L_R and C_R are the inductance and capacitance on the Rx side respectively. The circuit schematic of the WPT system is shown in Figure 5-21a. An arbitrary waveform generator is used to apply a

sinusoidal voltage to the Tx coil and the input power is fixed at 250 mW. The delivered voltage over a fixed resistor is measured by an oscilloscope. Figure 5-22 shows the AC signal across Rx coil and the WPT power was calculated.

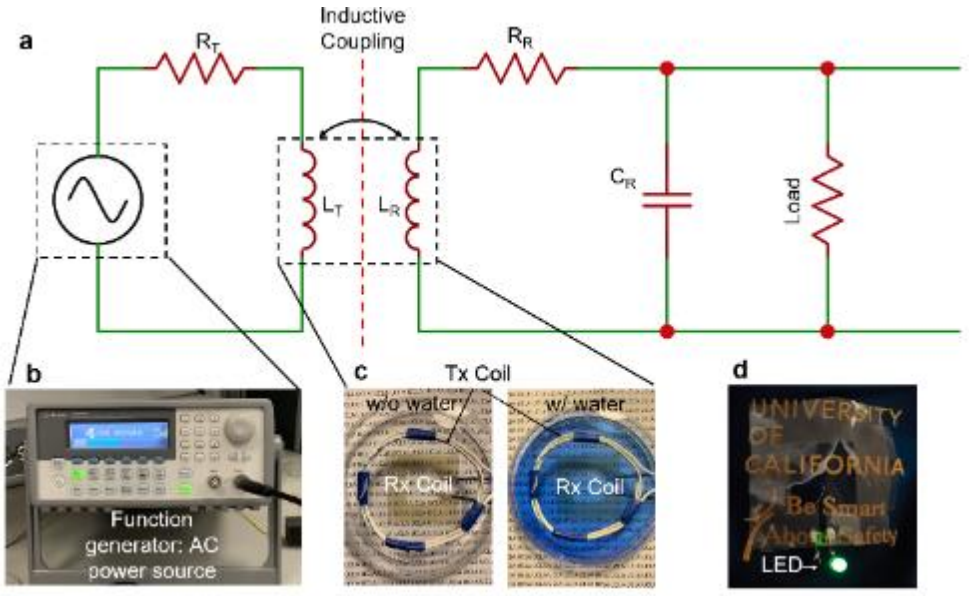

Figure 5-21. (a) Circuit diagram of the WPT system. (b) The high frequency AC power is supplied with a function generator. (c) Illustration of the set-up of the WPT link, left: without water, right: with 5mm deep water. (d) A green LED lit by WPT.

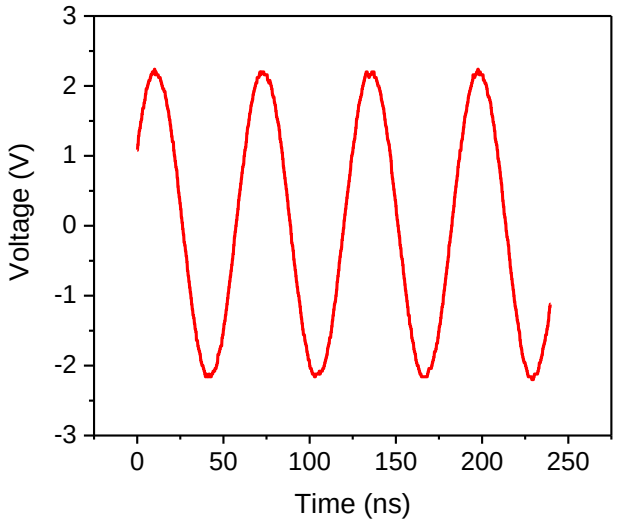

Figure 5-22. Wirelessly received AC signal measured by oscilloscope, load resistance = 1k ohm, distance between Tx and Rx is 10 mm.

The output voltage and power from the Rx coil as functions of the operating frequency and the load resistance are measured and shown in Figure 5-24 and Figure 5-25, respectively.

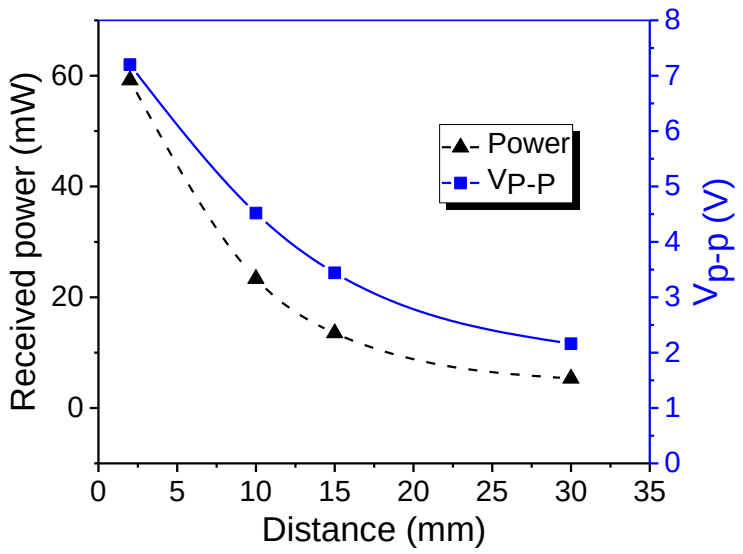

Figure 5-23. WPT received power and peak-to-peak voltage as functions of the distance between the Tx and Rx coils, load resistance = 1k ohm, operation frequency 15 MHz.

The voltage peaks at 15 MHz in accordance with its resonance frequency. The delivered power is dependent on the load resistance. It maximizes for the load resistance of 50 ohms at a distance of 10 mm with an output power of 23.3 mW, which sheds light on the design of future customized energy-salvaging circuitry(*118, 119*). As the indication of the magnetic interaction strength, the mutual inductance (*M*) of two adjacent coils can be derived from the equation $M = k\sqrt{L_T L_R}$, where *k* is the coupling coefficient, $L_T, L_R$are inductance of Tx and Rx coils respectively. *k* can be calculated as(*120*)

$$k = \frac{1}{[1+2^{2/3}(d/\sqrt{r_1 r_2})^2]^{3/2}} \quad (2)$$

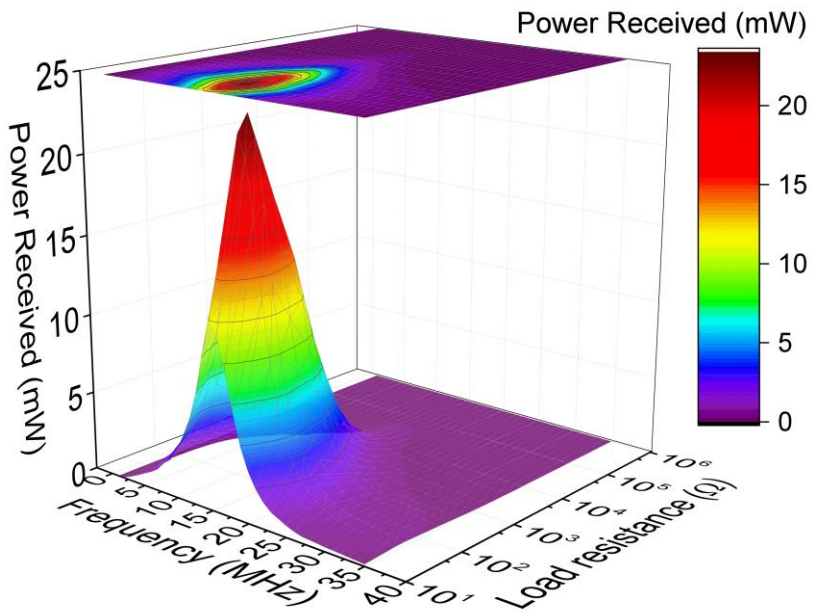

Figure 5-24. The WPT peak-to-peak voltage as a function of the load resistance and frequency, load resistance = 1k ohm, distance between Tx and Rx is 10 mm.

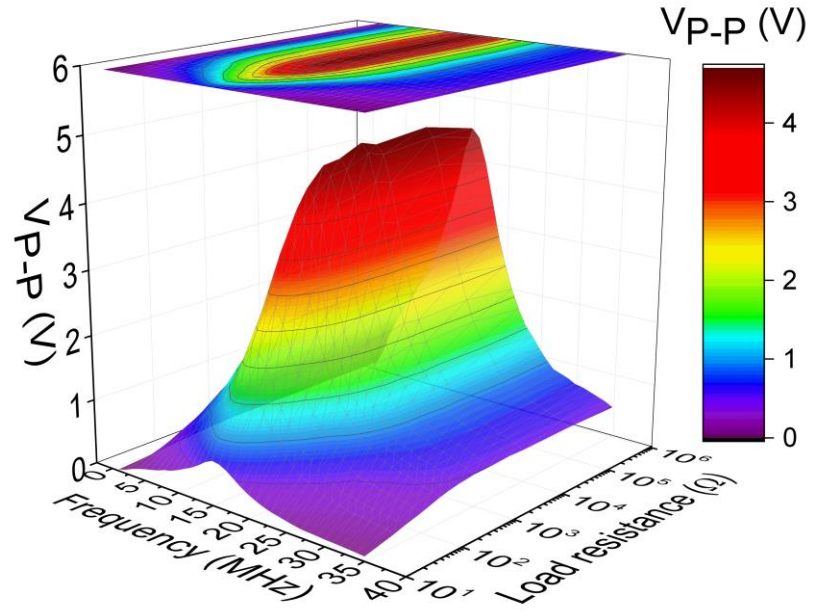

Figure 5-25. The WPT power as a function of the load resistance and frequency, load resistance = 1k ohm, the distance between Tx and Rx is 10 mm.

where r_1 and r_2 are the radii of the Tx and Rx coils. d is the distance between the two coils. The WPT energy decreases as the distance between the two coils increases. A

maximum WPT power of 59 mW (efficiency ~ 24%) is transferred wirelessly at a distance of 2 mm. For load resistance of 50 ohms, the delivered power as much as 5mW is achieved with the Tx-Rx distance up to 30 mm. A green light-emitting diode (LED) was connected to the Rx coil to illustratively demonstrate the functionality of the system, as shown in Figure 5-21d. The LED has a forward voltage of 2.2 V.

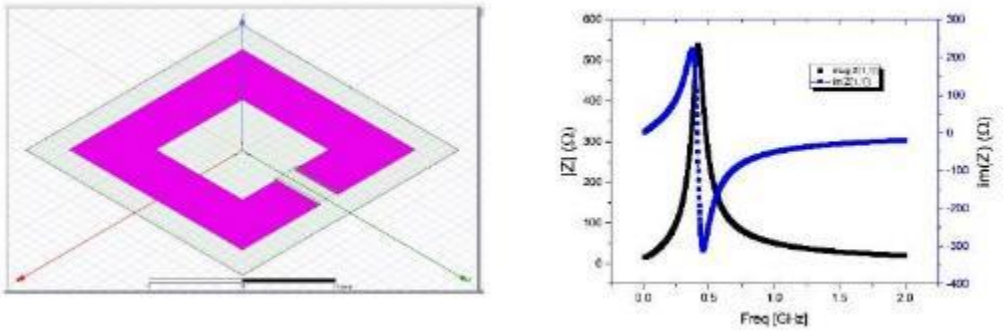

Figure 5-26. Simulation of the flat single turn Rx coil. Left 3D illustration, right simulation result.

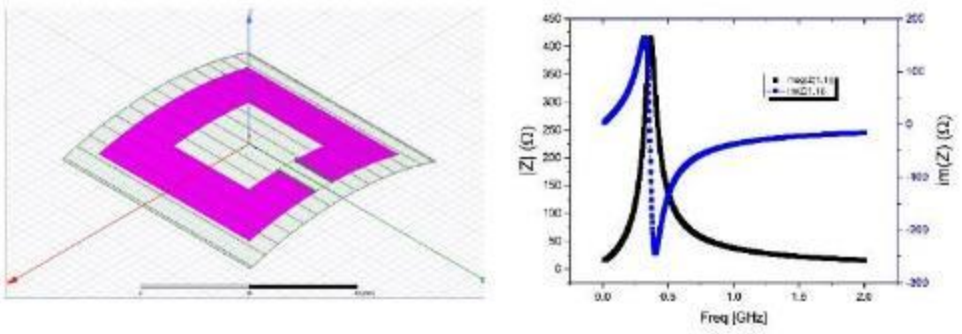

Figure 5-27. Simulation of the bended (radius = 8 mm) single turn Rx coil. Left 3D illustration, right simulation result.

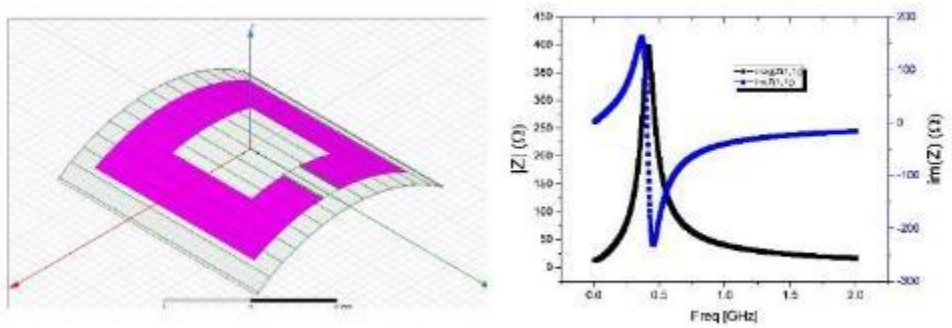

Figure 5-28. Simulation of the bended (radius = 4 mm) single turn Rx coil. Left 3D illustration, right simulation result.

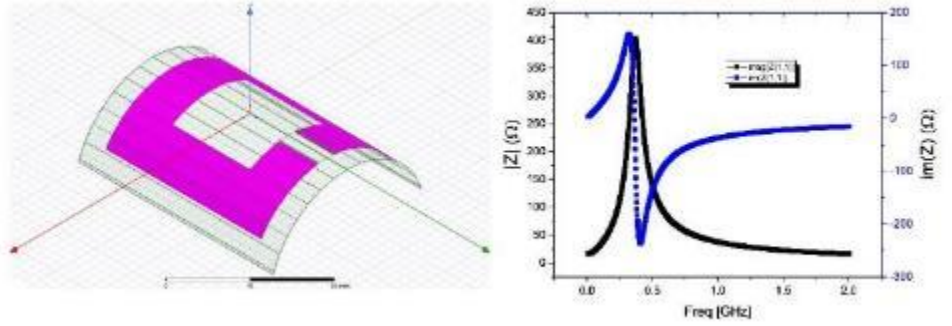

Figure 5-29. Simulation of the bent (radius = 2 mm) single turn Rx coil. Left 3D illustration, right simulation result.

For wearable electronics, the energy harvesting coil usually conforms to the surface of the human body, which could cause variations to the setup. The possible resistance change of the AgNW-PUA nanocomposite, in this case, was shown to be negligible. Also, finite element analysis proves that the self-resonance frequency only shifts marginally even at a bending radius of 40 mm (Figure 5-26~29).

5.4 Conclusion

In summary, we have successfully demonstrated stretchable and transparent wireless charging coil fabricated by the NATP method based on AgNW-PUA composite. The NATP method is based on adhesive elastomer and is compatible with solution-process technologies for large scale production. The resolution of NATP depends mostly on the resolution of adhesive stamps and can be potentially used for micro fabrications applications. The high aspect ratio AgNW provides excellent electrical conductivity, even under a significant strain and maintains an excellent optical transparency. The PUA acts as the polymer matrix for the AgNWs and shows excellent mechanical properties. The elastomeric coil retains high conductivity after a large number of bending and stretching cycles and can survive at a strain of 60%. A wireless power transport system was fabricated to investigate the practicality of the transparent coils. It has a resonant frequency at 15 MHz, and with a maximum output power of 59 mW at 2 mm. The Finite Element Method (FEM) is used to model the wireless power transfer when the coil is bending and the result matches well with experiments. A LED bulb with a forward voltage of 2.2 V was lit showing the practical applications for wireless charging of wearable electronics. This work demonstrates the feasibility of wirelessly charging wearable electronics with intrinsic stretchable and transparent coils.

6 Summary and Outlook

6.1 Concluding remarks

This dissertation investigates several applications of electrical functional polymer and nanocomposites, including the electrocaloric materials as well as their applications in novel cooling technology and wireless power transfer circuit for wearable electronics power supply.

The electrocaloric effect describes the adiabatic temperature change as a response to the external electric field. The fundamental physics of ECE is based on the electrically controlled dipole orientation. In chapter 2 and 3, P(VDF-TrFE-CFE) and its composites have been studied for its excellent EC responses. Freestanding EC thin films were fabricated through moisture mediated debonding process. A direct EC measurement technique was developed and has been used for the characterization of as-fabricated EC films. a peak temperature change of ~6 K for both cooling and heating can be achieved at 173 MV/m. The EC temperature change is fast (<0.1 s) due to the rapid switching of the dipoles inside of the EC materials under an external electric field. Cycling test was also conducted to demonstrate the reliability of the EC thin film. After one hour of cycling under an electric field of 173 MV/m, the total temperature difference of 12 K can be sustained. It indicates the robustness of the P(VDF-TrFE-CFE) thin film. Several approaches were proposed to further enhance the EC and dielectric properties of P(VDF-TrFE-CFE) terpolymer. Unsaturated P(VDF-TrFE-CFE) containing C=C double bond (PVDF-TrFE-CFE-DB) was synthesized through controlled dehydrochlorination catalyzed by an organic base, Triethylamine (TEA). Further modification of fluoropolymer chains necessitates the

introduction of the C=C double bonds. It provides active sites of crosslinking and opens a door for the introduction of desired functional groups.

The discovery of the giant electrocaloric effect initiated the research into the practical EC cooling devices. The heat switch and the thermal cycle design play significant roles in a functional EC device. At UCLA, we developed an electrostatically actuated heat switch which empowers a compact and efficient EC cooler. In addition, the electrostatic force ensures excellent thermal contact between the EC film and heat sink/source as a result of electrostatic pressure. In chapter 4, a highly efficient EC cooling was demonstrated. One operating cycle consists of four main steps: 1) electrostatic actuation of the EC polymer stack towards the bottom aluminum plate (heat sink), 2) electrocaloric heating of the EC polymer stack, 3) electrostatic actuation of the EC polymer stack towards the top aluminum plate (heat source), and 4) electrocaloric cooling of the EC polymer stack. An infrared camera and thermal couples were used for the temperature measurement. A solid-state cooling device with a high specific cooling power of 2.8 W/g and a COP of 13 was presented.

Chapter 5 demonstrates a transparent wireless power transfer coil utilizing AgNW/PUA nanocomposite. Wireless power transfer technology is widely regarded as a promising and preferable power recharging method for wearable electronics for its contact-free nature. However, the development of wearable electronics requires novel receiving coils which are compatible with the soft and flexible components of the wearable devices. In addition, with the rapid development of AR/VR technologies, a transparent and stretchable wireless charging coils can accelerate the adaption of these cutting-edge devices. In this dissertation, we present successful development of transparent and stretchable

wireless charging coils, using the negative adhesive transfer printing (NATP) method. A 50 μm wide AgNW strip was printed to demo the precision and resolution of the NATP method. The as-fabricated stretchable transparent coil is used as the receiver coil for wireless charging and can drive a LED bulb at full brightness range. The wireless charging coil is still functional after 1000 times bending and stretching cycles. Moreover, the wireless charging coil is optimized and studied using finite element analysis.

6.2 Future outlook

The development of EC cooling devices provides an alternate solution and environment-friendly solution for existing air conditioning technologies. The electrostatic actuated EC cooling device fabricated at UCLA demonstrated a feasible way for the EC cooling device design and laid the foundation for future optimization. From the practical standpoint of view, the advances in devices and materials are always coupled. To better propel the EC technology, it is necessary to take both material development and device design optimization into consideration.

In light of the EC materials development, various EC materials with maximum temperature change up to 50 K have been successfully synthesized in the past decade(*12*, *19*, *33*, *47*, *121*). These signs of progress made it clear that although it is still interesting to develop EC materials with substantial adiabatic temperature change, the absolute EC temperature change value is no longer the bottleneck for EC cooling applications. There are several material properties require more attention.

Firstly, the reliability of the EC materials is crucial, especially for mass adaption of the EC cooling technology. Because the ECE is a material property under external electric field, it is necessary to apply a high external electric field across the EC thin films or multi-

layer capacitors. The dielectric breakdown follows the Weibull statistics(*122*), where the breakdown possibility increases dramatically with the increasing operation field. To improve the electrical reliability of the EC materials, we can effectively improve the EC response in the low electric field range and apply the EC operation voltage far below the breakdown field strength. There are also some reports that investigated the enhanced dielectric and capacitive performance of nanocomposites with the aid of the Boron Nitride nanosheet(*47*, *123*).

Secondly, the thermal conductivity of the EC materials limits the operation frequency of the EC devices and determines the cooling power density. In the EC materials, their temperature oscillates driven by the external electric field. For each cycle, the maximum cooling power is limited by the materials' EC temperature change and breakdown field strength. By adding cycles in unit time (frequency), the overall heat transfer can be boosted. However, it is not realistic to expect that all the heat can be expelled within a cycle. The operation frequency is largely dominated by the thermal time constant of the EC component (EC films or EC MLCs). Generally, the thermal time constant is proportional to the thermal conductivity of a material. Hence it is directly related to future device design to develop EC materials with higher thermal conductivities. Introducing thermal conductive component into composites is a typical method for thermal conductivity enhancement(*47*, *123*). Another approach is to provide an alternative thermal pathway for the EC active part. Therefore the heat can be quickly dissipated through the thermal conductivity materials(*22*, *124*).

Future development of EC devices has the potential to realize high performing, cost-efficient, and reliable cooling technology, especially for the advancement of compact

cooling applications. Based on the discussion of Chapter 3, the electrostatic controlled heat switch has demonstrated the feasibility of EC cooling device. The continuing improvement in the following fields is critical for the mass scale adaption of EC cooling technology.

The heat flux pathway and thermal design of the EC device are essential topics for future research. As we discussed previously, the temperature change of the EC device is limited by the temperature change of the EC materials. However, it is both the reliability and electrical design problem to drive the EC film under high voltage. To fabricate an EC stack with EC units placed as a cascade is an effective method to multiply temperature span. An effort has been made in our group to develop EC cascade device, which can achieve much higher temperature span than that of the EC material.

In our prototype, the operation voltage was from 1kV to 2 kV. The EC unit itself is effectively a capacitor with square wave applied periodically. It is promising to reuse the electricity of the discharging cycle and improve the electrical usage efficiency. Both theoretical and experimental studies have been conducted to support the idea of introducing an energy recovery mechanism to the EC device(*125*). Through energy recovery, it is practical to improve the EC cooling device by several times.

The electrocaloric cooling technology is still in its infancy. However, the discovery of the giant ECE and the invention of the electrostatically controlled heat switch inspired a vast number of new systems which once only existed in theory and materialized into functional devices.

Reference

1. Annual Energy Outlook 2019 with projections to 2050, 83.

2. A. Smith, Who discovered the magnetocaloric effect?: Warburg, Weiss, and the connection between magnetism and heat. *EPJ H*. **38**, 507–517 (2013).

3. A. S. Mischenko, Giant Electrocaloric Effect in Thin-Film PbZr0.95Ti0.05O3. *Science*. **311**, 1270–1271 (2006).

4. B. Neese, B. Chu, S.-G. Lu, Y. Wang, E. Furman, Q. M. Zhang, Large Electrocaloric Effect in Ferroelectric Polymers Near Room Temperature. *Science*. **321**, 821–823 (2008).

5. F. Allab, A. Kedous-Lebouc, J. M. Fournier, J. P. Yonnet, Numerical modeling for active magnetic regenerative refrigeration. *IEEE Trans. Magn.* **41**, 3757–3759 (2005).

6. G. V. Brown, Magnetic heat pumping near room temperature. *Journal of Applied Physics*. **47**, 3673–3680 (1976).

7. A. Aznar, P. Lloveras, M. Romanini, M. Barrio, J.-L. Tamarit, C. Cazorla, D. Errandonea, N. D. Mathur, A. Planes, X. Moya, L. Mañosa, Giant barocaloric effects over a wide temperature range in superionic conductor AgI. *Nature Communications*. **8**, 1851 (2017).

8. J. Tušek, K. Engelbrecht, D. Eriksen, S. Dall'Olio, J. Tušek, N. Pryds, A regenerative elastocaloric heat pump. *Nature Energy*. **1**, 16134 (2016).

9. T. Correia, Q. Zhang, Eds., *Electrocaloric materials: new generation of coolers* (Springer, Heidelberg, 2014), *Engineering materials*.

10. D. Feng, S.-C. Yao, T. Zhang, Q. Zhang, Modeling of a Smart Heat Pump Made of Laminated Thermoelectric and Electrocaloric Materials. *J. Electron. Packag*. **138**, 041004 (2016).

11. P. Kobeko, J. Kurtschatov, Dielektrische Eigenschaften der Seignettesalzkristalle. *Z. Physik*. **66**, 192–205 (1930).

12. J. Shi, D. Han, Z. Li, L. Yang, S.-G. Lu, Z. Zhong, J. Chen, Q. M. Zhang, X. Qian, Electrocaloric Cooling Materials and Devices for Zero-Global-Warming-Potential, High-Efficiency Refrigeration. *Joule* (2019), doi:10.1016/j.joule.2019.03.021.

13. R. Kishore, S. Priya, A Review on Low-Grade Thermal Energy Harvesting: Materials, Methods and Devices. *Materials*. **11**, 1433 (2018).

14. S. B. Lang, Pyroelectricity: From Ancient Curiosity to Modern Imaging Tool. *Physics Today*. **58**, 31–36 (2005).

15. J. Y. Noh, G. H. Yoon, Topology optimization of piezoelectric energy harvesting devices considering static and harmonic dynamic loads. *Advances in Engineering Software*. **53**, 45–60 (2012).

16. V. V. Shvartsman, S. E. Aksenov, E. D. Politova, Phase relations and ferroelectric properties of Pb(Zr, Sn, Ti)O $_3$ ceramics. *Ferroelectrics*. **258**, 13–20 (2001).

17. P. D. Thacher, Electrocaloric Effects in Some Ferroelectric and Antiferroelectric Pb(Zr, Ti)O $_3$ Compounds. *Journal of Applied Physics*. **39**, 1996–2002 (1968).

18. R. B. Olsen, W. F. Butler, D. A. Payne, B. A. Tuttle, P. C. Held, Observation of a Polarocaloric (Electrocaloric) Effect of 2 °C in Lead Zirconate Modified with Sn 4 + and T i 4 +. *Phys. Rev. Lett.* **45**, 1436–1438 (1980).

19. G. Zhang, B. Fan, P. Zhao, Z. Hu, Y. Liu, F. Liu, S. Jiang, S. Zhang, H. Li, Q. Wang, Ferroelectric Polymer Nanocomposites with Complementary Nanostructured Fillers for Electrocaloric Cooling with High Power Density and Great Efficiency. *ACS Appl. Energy Mater.* **1**, 1344–1354 (2018).

20. G. C. Lin, X. M. Xiong, J. X. Zhang, Q. Wei, Latent heat study of phase transition in Ba0.73Sr0.27TiO3 induced by electric field. *J Therm Anal Calorim*. **81**, 41–44 (2005).

21. Y. Bai, G.-P. Zheng, S.-Q. Shi, Abnormal electrocaloric effect of Na0.5Bi0.5TiO3–BaTiO3 lead-free ferroelectric ceramics above room temperature. *Materials Research Bulletin*. **46**, 1866–1869 (2011).

22. S. Hirose, T. Usui, S. Crossley, B. Nair, A. Ando, X. Moya, N. D. Mathur, Progress on electrocaloric multilayer ceramic capacitor development. *APL Materials*. **4**, 064105 (2016).

23. F. Xia, S. Tadigadapa, Q. M. Zhang, Electroactive polymer based microfluidic pump. *Sensors and Actuators A: Physical*. **125**, 346–352 (2006).

24. Y. Bar-Cohen, Q. Zhang, Electroactive Polymer Actuators and Sensors. *MRS Bull.* **33**, 173–181 (2008).

25. Q. M. Zhang, H. Li, M. Poh, F. Xia, Z.-Y. Cheng, H. Xu, C. Huang, An all-organic composite actuator material with a high dielectric constant. *Nature*. **419**, 284–287 (2002).

26. M. Q. Le, J.-F. Capsal, J. Galineau, F. Ganet, X. Yin, M. Yang, J.-F. Chateaux, L. Renaud, C. Malhaire, P.-J. Cottinet, R. Liang, All-organic electrostrictive polymer composites with low driving electrical voltages for micro-fluidic pump applications. *Sci Rep*. **5**, 11814 (2015).

27. R. Hasegawa, Y. Takahashi, Y. Chatani, H. Tadokoro, Crystal Structures of Three Crystalline Forms of Poly(vinylidene fluoride). *Polym J*. **3**, 600–610 (1972).

28. L. Ruan, X. Yao, Y. Chang, L. Zhou, G. Qin, X. Zhang, Properties and Applications of the β Phase Poly(vinylidene fluoride). *Polymers*. **10**, 228 (2018).

29. C. Wan, C. R. Bowen, Multiscale-structuring of polyvinylidene fluoride for energy harvesting: the impact of molecular-, micro- and macro-structure. *J. Mater. Chem. A*. **5**, 3091–3128 (2017).

30. T. Yagi, M. Tatemoto, J. Sako, Transition Behavior and Dielectric Properties in Trifluoroethylene and Vinylidene Fluoride Copolymers. *Polym J*. **12**, 209–223 (1980).

31. S. G. Lu, B. Rozic, Z. Kutnjiak, Q. M. Zhang, Electrocaloric Effect in Ferroelectric P(VDF-TrFE) Copolymers. *Integrated Ferroelectrics*. **125**, 176–185 (2011).

32. G. Zhang, X. Zhang, T. Yang, Q. Li, L.-Q. Chen, S. Jiang, Q. Wang, Colossal Room-Temperature Electrocaloric Effect in Ferroelectric Polymer Nanocomposites Using Nanostructured Barium Strontium Titanates. *ACS Nano*. **9**, 7164–7174 (2015).

33. J. Qian, R. Peng, Z. Shen, J. Jiang, F. Xue, T. Yang, L. Chen, Y. Shen, Interfacial Coupling Boosts Giant Electrocaloric Effects in Relaxor Polymer Nanocomposites: In Situ Characterization and Phase-Field Simulation. *Advanced Materials*, 1801949 (2018).

34. R. I. Epstein, K. J. Malloy, Electrocaloric devices based on thin-film heat switches. *Journal of Applied Physics*. **106**, 064509 (2009).

35. Y. Wang, D. E. Schwartz, S. J. Smullin, Q. Wang, M. J. Sheridan, Silicon Heat Switches for Electrocaloric Cooling. *Journal of Microelectromechanical Systems*. **26**, 580–587 (2017).

36. Y. Jia, Y. Sungtaek Ju, A solid-state refrigerator based on the electrocaloric effect. *Applied Physics Letters*. **100**, 242901 (2012).

37. K. Guk, G. Han, J. Lim, K. Jeong, T. Kang, E.-K. Lim, J. Jung, Evolution of Wearable Devices with Real-Time Disease Monitoring for Personalized Healthcare. *Nanomaterials*. **9**, 813 (2019).

38. Wearables Market to Be Worth $25 Billion by 2019. *CCS Insight*, (available at https://www.ccsinsight.com/press/company-news/2332-wearables-market-to-be-worth-25-billion-by-2019-reveals-ccs-insight/).

39. A. Kurs, A. Karalis, R. Moffatt, J. D. Joannopoulos, P. Fisher, M. Soljacic, Wireless Power Transfer via Strongly Coupled Magnetic Resonances. *Science*. **317**, 83–86 (2007).

40. L. Sun, D. Ma, H. Tang, A review of recent trends in wireless power transfer technology and its applications in electric vehicle wireless charging. *Renewable and Sustainable Energy Reviews*. **91**, 490–503 (2018).

41. Wireless power transfer. *Wikipedia* (2019), (available at https://en.wikipedia.org/w/index.php?title=Wireless_power_transfer&oldid=903753747).

42. J. O. Mur-Miranda, G. Fanti, Y. Feng, K. Omanakuttan, R. Ongie, A. Setjoadi, N. Sharpe, in *2010 IEEE Energy Conversion Congress and Exposition* (IEEE, Atlanta, GA, 2010; https://ieeexplore.ieee.org/document/5617728/), pp. 4179–4186.

43. J. Liang, L. Li, X. Niu, Z. Yu, Q. Pei, Elastomeric polymer light-emitting devices and displays. *Nature Photonics*. **7**, 817–824 (2013).

44. Z. Yu, Q. Zhang, L. Li, Q. Chen, X. Niu, J. Liu, Q. Pei, Highly Flexible Silver Nanowire Electrodes for Shape-Memory Polymer Light-Emitting Diodes. *Advanced Materials*. **23**, 664–668 (2011).

45. W. Hu, X. Niu, L. Li, S. Yun, Z. Yu, Q. Pei, Intrinsically stretchable transparent electrodes based on silver-nanowire–crosslinked-polyacrylate composites. *Nanotechnology*. **23**, 344002 (2012).

46. D. McCoul, W. Hu, M. Gao, V. Mehta, Q. Pei, Recent Advances in Stretchable and Transparent Electronic Materials. *Advanced Electronic Materials*. **2**, 1500407 (2016).

47. G. Zhang, Q. Li, H. Gu, S. Jiang, K. Han, M. R. Gadinski, M. A. Haque, Q. Zhang, Q. Wang, Ferroelectric Polymer Nanocomposites for Room-Temperature Electrocaloric Refrigeration. *Advanced Materials*. **27**, 1450–1454 (2015).

48. X.-S. Qian, S.-G. Lu, X. Li, H. Gu, L.-C. Chien, Q. Zhang, Large Electrocaloric Effect in a Dielectric Liquid Possessing a Large Dielectric Anisotropy Near the Isotropic–Nematic Transition. *Advanced Functional Materials*. **23**, 2894–2898 (2013).

49. F. Bauer, Relaxor fluorinated polymers: novel applications and recent developments. *IEEE Trans. Dielect. Electr. Insul.* **17**, 1106–1112 (2010).

50. F. Bauer, E. Fousson, Q. M. Zhang, L. M. Lee, in *Proceedings. 11th International Symposium on Electrets* (IEEE, Melbourne, Vic., Australia, 2002; http://ieeexplore.ieee.org/document/1043017/), pp. 355–358.

51. X. Chen, W. Xu, B. Lu, T. Zhang, Q. Wang, Q. M. Zhang, Towards electrocaloric heat pump—A relaxor ferroelectric polymer exhibiting large electrocaloric response at low electric field. *Applied Physics Letters*. **113**, 113902 (2018).

52. W. B. Jensen, The Origin of the Soxhlet Extractor. *J. Chem. Educ.* **84**, 1913 (2007).

53. S. T. Choi, J. O. Kwon, F. Bauer, Multilayered relaxor ferroelectric polymer actuators for low-voltage operation fabricated with an adhesion-mediated film transfer technique. *Sensors and Actuators A: Physical*. **203**, 282–290 (2013).

54. J. Qian, J. Jiang, Y. Shen, Enhanced electrocaloric strength in P(VDF-TrFE-CFE) by decreasing the crystalline size. *Journal of Materiomics*, S2352847819300395 (2019).

55. H.-M. Bao, J.-F. Song, J. Zhang, Q.-D. Shen, C.-Z. Yang, Q. M. Zhang, Phase Transitions and Ferroelectric Relaxor Behavior in P(VDF−TrFE−CFE) Terpolymers. *Macromolecules*. **40**, 2371–2379 (2007).

56. A. J. Lovinger, G. T. Davis, T. Furukawa, M. G. Broadhurst, Crystalline forms in a copolymer of vinylidene fluoride and trifluoroethylene (52/48 mol %). *Macromolecules*. **15**, 323–328 (1982).

57. Q. Wang, L. Zhu, Polymer nanocomposites for electrical energy storage. *Journal of Polymer Science Part B: Polymer Physics*. **49**, 1421–1429 (2011).

58. M. S. Whittingham, Materials Challenges Facing Electrical Energy Storage. *MRS Bull.* **33**, 411–419 (2008).

59. F. Liu, Q. Li, J. Cui, Z. Li, G. Yang, Y. Liu, L. Dong, C. Xiong, H. Wang, Q. Wang, High-Energy-Density Dielectric Polymer Nanocomposites with Trilayered Architecture. *Adv. Funct. Mater.* **27**, 1606292 (2017).

60. M. Rabuffi, G. Picci, Status quo and future prospects for metallized polypropylene energy storage capacitors. *IEEE Trans. Plasma Sci.* **30**, 1939–1942 (2002).

61. Y. Zhou, Q. Li, B. Dang, Y. Yang, T. Shao, H. Li, J. Hu, R. Zeng, J. He, Q. Wang, A Scalable, High-Throughput, and Environmentally Benign Approach to Polymer Dielectrics Exhibiting Significantly Improved Capacitive Performance at High Temperatures. *Adv. Mater.* **30**, 1805672 (2018).

62. Prateek, V. K. Thakur, R. K. Gupta, Recent Progress on Ferroelectric Polymer-Based Nanocomposites for High Energy Density Capacitors: Synthesis, Dielectric Properties, and Future Aspects. *Chemical Reviews*. **116**, 4260–4317 (2016).

63. B. Chu, X. Zhou, K. Ren, B. Neese, M. Lin, Q. Wang, F. Bauer, Q. M. Zhang, A Dielectric Polymer with High Electric Energy Density and Fast Discharge Speed. *Science*. **313**, 334 (2006).

64. Y. Shen, Y. Lin, Q. M. Zhang, Polymer nanocomposites with high energy storage densities. *MRS Bulletin*. **40**, 753–759 (2015).

65. X.-Z. Chen, Z.-W. Li, Z.-X. Cheng, J.-Z. Zhang, Q.-D. Shen, H.-X. Ge, H.-T. Li, Greatly Enhanced Energy Density and Patterned Films Induced by Photo Cross-Linking of Poly(vinylidene fluoride-chlorotrifluoroethylene). *Macromolecular Rapid Communications*. **32**, 94–99 (2011).

66. R. Ma, Z. Zhang, K. Tong, D. Huber, R. Kornbluh, Y. S. Ju, Q. Pei, Highly efficient electrocaloric cooling with electrostatic actuation. *Science*. **357**, 1130–1134 (2017).

67. S.-G. Lu, Q. Zhang, Electrocaloric Materials for Solid-State Refrigeration. *Adv. Mater.* **21**, 1983–1987 (2009).

68. Q. M. Zhang, Giant Electrostriction and Relaxor Ferroelectric Behavior in Electron-Irradiated Poly(vinylidene fluoride-trifluoroethylene) Copolymer. *Science*. **280**, 2101–2104 (1998).

69. X. Chen, L. Liu, S.-Z. Liu, Y.-S. Cui, X.-Z. Chen, H.-X. Ge, Q.-D. Shen, P(VDF-TrFE-CFE) terpolymer thin-film for high performance nonvolatile memory. *Appl. Phys. Lett.* **102**, 063103 (2013).

70. X. Chen, X. Han, Q.-D. Shen, PVDF-Based Ferroelectric Polymers in Modern Flexible Electronics. *Adv. Electron. Mater.* **3**, 1600460 (2017).

71. Z. Zhang, Q. Meng, T. C. M. Chung, Energy storage study of ferroelectric poly(vinylidene fluoride-trifluoroethylene-chlorotrifluoroethylene) terpolymers. *Polymer*. **50**, 707–715 (2009).

72. S. Tan, J. Li, G. Gao, H. Li, Z. Zhang, Synthesis of fluoropolymer containing tunable unsaturation by a controlled dehydrochlorination of P(VDF-co-CTFE) and its curing for high performance rubber applications. *Journal of Materials Chemistry*. **22**, 18496 (2012).

73. S. Tan, X. Hu, S. Ding, Z. Zhang, H. Li, L. Yang, Significantly improving dielectric and energy storage properties via uniaxially stretching crosslinked P(VDF-co-TrFE) films. *Journal of Materials Chemistry A*. **1**, 10353 (2013).

74. S. Nandi, H. H. Winter, Swelling Behavior of Partially Cross-Linked Polymers: A Ternary System. *Macromolecules*. **38**, 4447–4455 (2005).

75. X.-Z. Chen, Z.-X. Cheng, L. Liu, X.-D. Yang, Q.-D. Shen, W.-B. Hu, H.-T. Li, Evolution of nanopolar phases, interfaces, and increased dielectric energy storage capacity in photoinitiated cross-linked poly(vinylidene fluoride)-based copolymers. *Colloid Polym Sci*. **291**, 1989–1997 (2013).

76. H. Guo, Y. Zhang, F. Xue, Z. Cai, Y. Shang, J. Li, Y. Chen, Z. Wu, S. Jiang, In-situ synchrotron SAXS and WAXS investigations on deformation and α–β transformation of uniaxial stretched poly(vinylidene fluoride). *CrystEngComm*. **15**, 1597 (2013).

77. J. Chen, S. Tan, G. Gao, H. Li, Z. Zhang, Synthesis and characterization of thermally self-curable fluoropolymer triggered by TEMPO in one pot for high performance rubber applications. *Polym. Chem.* **5**, 2130 (2014).

78. H. F. Brinson, L. C. Brinson, in *Polymer Engineering Science and Viscoelasticity: An Introduction*, H. F. Brinson, L. C. Brinson, Eds. (Springer US, Boston, MA, 2015; https://doi.org/10.1007/978-1-4899-7485-3_3), pp. 57–100.

79. V. Bharti, Q. M. Zhang, Dielectric study of the relaxor ferroelectric poly(vinylidene fluoride-trifluoroethylene) copolymer system. *Phys. Rev. B.* **63**, 184103 (2001).

80. Y.-X. Chen, Z.-X. Cheng, Q.-D. Shen, Regulation of energy storage capacitance and efficiency in semi-crystalline vinylidene fluoride copolymers through cross-linking method. *IEEE Trans. Dielect. Electr. Insul.* **24**, 682–688 (2017).

81. J. Fu, Y. Hou, M. Zheng, Q. Wei, M. Zhu, H. Yan, Improving Dielectric Properties of PVDF Composites by Employing Surface Modified Strong Polarized $BaTiO_3$ Particles Derived by Molten Salt Method. *ACS Appl. Mater. Interfaces*. **7**, 24480–24491 (2015).

82. H.-P. Xu, Z.-M. Dang, N.-C. Bing, Y.-H. Wu, D.-D. Yang, Temperature dependence of electric and dielectric behaviors of Ni/polyvinylidene fluoride composites. *Journal of Applied Physics*. **107**, 034105 (2010).

83. B. Hilczer, H. Smogór, J. Goslar, Dielectric response of polymer relaxors. *J Mater Sci*. **41**, 117–127 (2006).

84. S. Wang, Q. Li, Design, synthesis and processing of PVDF-based dielectric polymers. *IET Nanodielectrics*. **1**, 80–91 (2018).

85. J. M. Gonçalves, C. Melo, C. J. L. Hermes, J. R. Barbosa Jr., Experimental mapping of the thermodynamic losses in vapor compression refrigeration systems. *J. Braz. Soc. Mech. Sci. & Eng.* **33**, 159–165 (2011).

86. I. Chowdhury, R. Prasher, K. Lofgreen, G. Chrysler, S. Narasimhan, R. Mahajan, D. Koester, R. Alley, R. Venkatasubramanian, On-chip cooling by superlattice-based thin-film thermoelectrics. *Nature Nanotech.* **4**, 235–238 (2009).

87. Y. D. Wang, S. J. Smullin, M. J. Sheridan, Q. Wang, C. Eldershaw, D. E. Schwartz, A heat-switch-based electrocaloric cooler. *Applied Physics Letters*. **107**, 134103 (2015).

88. S. Jacobs, J. Auringer, A. Boeder, J. Chell, L. Komorowski, J. Leonard, S. Russek, C. Zimm, The performance of a large-scale rotary magnetic refrigerator. *International Journal of Refrigeration*. **37**, 84–91 (2014).

89. L. Engel, S. Kruk, J. Shklovsky, Y. Shacham-Diamand, S. Krylov, A study toward the development of an electromechanical poly(vinylidene fluoride–trifluoroethylene–chlorofluoroethylene) buckling membrane actuator. *J. Micromech. Microeng.* **24**, 125027 (2014).

90. K. Sato, M. Shikida, An electrostatically actuated gas valve with an S-shaped film element. *J. Micromech. Microeng.* **4**, 205–209 (1994).

91. Y. Liu, J. F. Scott, B. Dkhil, Direct and indirect measurements on electrocaloric effect: Recent developments and perspectives. *Applied Physics Reviews*. **3**, 031102 (2016).

92. H. Gu, X.-S. Qian, H.-J. Ye, Q. M. Zhang, An electrocaloric refrigerator without external regenerator. *Applied Physics Letters*. **105**, 162905 (2014).

93. M. J. Cima, Next-generation wearable electronics. *Nature Biotechnology*. **32**, 642–643 (2014).

94. D. Larcher, J.-M. Tarascon, Towards greener and more sustainable batteries for electrical energy storage. *Nature Chemistry*. **7**, 19–29 (2015).

95. Z. Yang, J. Deng, X. Sun, H. Li, H. Peng, Stretchable, Wearable Dye-Sensitized Solar Cells. *Advanced Materials*. **26**, 2643–2647 (2014).

96. Z. Wen, M.-H. Yeh, H. Guo, J. Wang, Y. Zi, W. Xu, J. Deng, L. Zhu, X. Wang, C. Hu, L. Zhu, X. Sun, Z. L. Wang, Self-powered textile for wearable electronics by hybridizing fiber-shaped nanogenerators, solar cells, and supercapacitors. *Science Advances*. **2**, e1600097 (2016).

97. S. J. Kim, J. H. We, B. J. Cho, A wearable thermoelectric generator fabricated on a glass fabric. *Energy & Environmental Science*. **7**, 1959 (2014).

98. H. Lyu, Z. Jian, X. Liu, Y. Sun, A. Babakhani, Towards the Implementation of a Wirelessly Powered Dielectric Sensor with Digitized Output for Implantable Applications. *IEEE Sensors Letters*, 1–1 (2019).

99. A. D. Mickle, S. M. Won, K. N. Noh, J. Yoon, K. W. Meacham, Y. Xue, L. A. McIlvried, B. A. Copits, V. K. Samineni, K. E. Crawford, D. H. Kim, P. Srivastava, B. H. Kim, S. Min, Y. Shiuan, Y. Yun, M. A. Payne, J. Zhang, H. Jang, Y. Li, H. H. Lai, Y. Huang, S.-I. Park, R. W. Gereau, J. A. Rogers, A wireless closed-loop system for optogenetic peripheral neuromodulation. *Nature*. **565**, 361–365 (2019).

100. H. Lyu, M. John, D. Burkland, B. Greet, Y. Xi, L. Sampaio, D. Taylor, M. Razavi, A. Babakhani, in *2018 40th Annual International Conference of the IEEE Engineering in Medicine and Biology Society (EMBC)* (IEEE, Honolulu, HI, 2018; https://ieeexplore.ieee.org/document/8512977/), pp. 3434–3437.

101. J. Kim, M. Kim, M.-S. Lee, K. Kim, S. Ji, Y.-T. Kim, J. Park, K. Na, K.-H. Bae, H. Kyun Kim, F. Bien, C. Young Lee, J.-U. Park, Wearable smart sensor systems integrated on soft contact lenses for wireless ocular diagnostics. *Nature Communications*. **8**, 14997 (2017).

102. S. Xu, Y. Zhang, J. Cho, J. Lee, X. Huang, L. Jia, J. A. Fan, Y. Su, J. Su, H. Zhang, H. Cheng, B. Lu, C. Yu, C. Chuang, T. Kim, T. Song, K. Shigeta, S. Kang, C. Dagdeviren, I. Petrov, P. V. Braun, Y. Huang, U. Paik, J. A. Rogers, Stretchable batteries with self-similar serpentine interconnects and integrated wireless recharging systems. *Nature Communications*. **4** (2013), doi:10.1038/ncomms2553.

103. S. H. Jeong, K. Hjort, Z. Wu, Tape Transfer Atomization Patterning of Liquid Alloys for Microfluidic Stretchable Wireless Power Transfer. *Scientific Reports*. **5** (2015), doi:10.1038/srep08419.

104. K. Tong, X. Liu, F. Zhao, D. Chen, Q. Pei, Efficient Light Extraction of Organic Light-Emitting Diodes on a Fully Solution-Processed Flexible Substrate. *Advanced Optical Materials*. **5**, 1700307 (2017).

105. J. Liang, L. Li, D. Chen, T. Hajagos, Z. Ren, S.-Y. Chou, W. Hu, Q. Pei, Intrinsically stretchable and transparent thin-film transistors based on printable silver nanowires, carbon nanotubes and an elastomeric dielectric. *Nature Communications*. **6** (2015), doi:10.1038/ncomms8647.

106. L. Li, J. Liang, H. Gao, Y. Li, X. Niu, X. Zhu, Y. Xiong, Q. Pei, A Solid-State Intrinsically Stretchable Polymer Solar Cell. *ACS Applied Materials & Interfaces*. **9**, 40523–40532 (2017).

107. H. Gao, K. Youssef, L. Li, X. Zhu, Q. Pei, Morphological study of an intrinsically stretchable photovoltaic bulk heterojunction. *Journal of Polymer Science Part B: Polymer Physics*. **56**, 814–820 (2018).

108. S. Yao, Y. Zhu, Wearable multifunctional sensors using printed stretchable conductors made of silver nanowires. *Nanoscale*. **6**, 2345 (2014).

109. A. R. Madaria, A. Kumar, F. N. Ishikawa, C. Zhou, Uniform, highly conductive, and patterned transparent films of a percolating silver nanowire network on rigid and flexible substrates using a dry transfer technique. *Nano Research*. **3**, 564–573 (2010).

110. D. Langley, G. Giusti, C. Mayousse, C. Celle, D. Bellet, J.-P. Simonato, Flexible transparent conductive materials based on silver nanowire networks: a review. *Nanotechnology*. **24**, 452001 (2013).

111. M. A. Meitl, E. Radauscher, R. Rotzoll, B. Raymond, S. Bonafede, D. Gomez, T. Moore, C. Prevatte, A. Fecioru, A. J. Trindade, C. A. Bower, 19-4: *Invited Paper* : Emissive Displays with Transfer-Printed Microscale Inorganic LEDs. *SID Symposium Digest of Technical Papers*. **48**, 257–263 (2017).

112. C. A. Bower, E. Menard, S. Bonafede, J. W. Hamer, R. S. Cok, Transfer-Printed Microscale Integrated Circuits for High Performance Display Backplanes. *IEEE Transactions on Components, Packaging and Manufacturing Technology*. **1**, 1916–1922 (2011).

113. M. A. Meitl, Z.-T. Zhu, V. Kumar, K. J. Lee, X. Feng, Y. Y. Huang, I. Adesida, R. G. Nuzzo, J. A. Rogers, Transfer printing by kinetic control of adhesion to an elastomeric stamp. *Nature Materials*. **5**, 33–38 (2006).

114. P. Lee, J. Lee, H. Lee, J. Yeo, S. Hong, K. H. Nam, D. Lee, S. S. Lee, S. H. Ko, Highly Stretchable and Highly Conductive Metal Electrode by Very Long Metal Nanowire Percolation Network. *Advanced Materials*. **24**, 3326–3332 (2012).

115. L. Hu, H. S. Kim, J.-Y. Lee, P. Peumans, Y. Cui, Scalable Coating and Properties of Transparent, Flexible, Silver Nanowire Electrodes. *ACS Nano*. **4**, 2955–2963 (2010).

116. S. De, T. M. Higgins, P. E. Lyons, E. M. Doherty, P. N. Nirmalraj, W. J. Blau, J. J. Boland, J. N. Coleman, Silver Nanowire Networks as Flexible, Transparent, Conducting Films: Extremely High DC to Optical Conductivity Ratios. *ACS Nano*. **3**, 1767–1774 (2009).

117. J. P. Kottmann, O. J. F. Martin, D. R. Smith, S. Schultz, Plasmon resonances of silver nanowires with a nonregular cross section. *Physical Review B*. **64**, 235402 (2001).

118. H. Lyu, J. Wang, J.-H. La, J. M. Chung, A. Babakhani, An Energy-Efficient Wirelessly Powered Millimeter-Scale Neurostimulator Implant Based on Systematic Codesign of an Inductive Loop Antenna and a Custom Rectifier. *IEEE Trans. Biomed. Circuits Syst.* **12**, 1131–1143 (2018).

119. H. Lyu, P. Gad, H. Zhong, V. R. Edgerton, A. Babakhani, A 430-MHz Wirelessly Powered Implantable Pulse Generator with Intensity/Rate Control and Sub-1 μ A Quiescent Current Consumption. *IEEE Trans. Biomed. Circuits Syst.*, 1–1 (2018).

120. T. Takamatsu, Y. Chen, T. Yoshimasu, M. Nishizawa, T. Miyake, Highly Efficient, Flexible Wireless-Powered Circuit Printed on a Moist, Soft Contact Lens. *Advanced Materials Technologies*, 1800671 (2019).

121. G. Zhang, X. Zhang, H. Huang, J. Wang, Q. Li, L.-Q. Chen, Q. Wang, Toward Wearable Cooling Devices: Highly Flexible Electrocaloric Ba0.67Sr0.33TiO3 Nanowire Arrays. *Advanced Materials*. **28**, 4811–4816 (2016).

122. C. Chauvet, C. Laurent, Weibull statistics in short-term dielectric breakdown of thin polyethylene films. *IEEE Trans. Elect. Insul.* **28**, 18–29 (1993).

123. Q. Li, L. Chen, M. R. Gadinski, S. Zhang, G. Zhang, H. U. Li, E. Iagodkine, A. Haque, L.-Q. Chen, T. N. Jackson, Q. Wang, Flexible high-temperature dielectric materials from polymer nanocomposites. *Nature*. **523**, 576–579 (2015).

124. G. Zhang, L. Weng, Z. Hu, Y. Liu, R. Bao, P. Zhao, H. Feng, N. Yang, M.-Y. Li, S. Zhang, S. Jiang, Q. Wang, Nanoconfinement-Induced Giant Electrocaloric Effect in Ferroelectric Polymer Nanowire Array Integrated with Aluminum Oxide Membrane to Exhibit Record Cooling Power Density. *Advanced Materials*, 1806642 (2019).

125. E. Defay, R. Faye, G. Despesse, H. Strozyk, D. Sette, S. Crossley, X. Moya, N. D. Mathur, Enhanced electrocaloric efficiency via energy recovery. *Nat Commun*. **9**, 1827 (2018).